
Ministero dell'Università e della Ricerca

Osservatorio Astronomico di Palermo "G.S.Vaiana"


Università degli Studi di Palermo

**DIPARTIMENTO DI FISICA**

**DOTTORATO DI RICERCA IN FISICA – XXIII CICLO**

# ANALYSIS OF SMALL-SCALE VARIABILITY OF CORONAL OBSERVATIONS WITH THE HINODE/X-RAY TELESCOPE

**(S.S.D. FIS/05)**

**Sergio Terzo**

Palermo, Febbraio 2012

Supervisore: prof. Fabio Reale

Coordinatore: prof. Antonio Cupane

# Abstract

My PhD thesis project is in the framework of investigating the heating of the solar corona, one of the most compelling and unsolved problems in astrophysics.

In my PhD thesis I examine a solar active region (Active Region - AR10923) observed by HINODE satellite on 14 November 2006 , and in particular its intensity fluctuations, to infer the presence of nanoflares, with the guiding idea that, if present, these impulsive events should leave their *signature* in the light curves.

My approach is to search for systematic effects in noisy background light curves. I apply specific methods for the time analysis, for the first time, to high-cadence HINODE observations.

As result I obtain that the distributions of intensity fluctuations have small but important asymmetries, either taken from individual pixels, multi-pixel subregions, or the entire active region. Moreover, negative fluctuations (corresponding to reduced intensity) are greater in number but weaker in amplitude, so that the median fluctuation is negative compared to a mean of zero. Monte Carlo simulations show that only part of this asymmetry and negative shift of the median can be explained by Poisson photon statistics. The remainder could be explained with a tendency for exponentially decreasing intensity, such as would be expected from a cooling plasma produced, e.g., from pulsed events as nanoflares.

A similar approach allows me to obtain also new temperature diagnostics of coronal active regions. Again, I analyze a high cadence observation of another

solar active region made on 1 April 2010, starting at 15:04:19 UT with a single-filter (Ti_poly) of Hinode/XRT. I use the variance of the intensity fluctuations as temperature proxy and derive the temperature map of the active region with a *single-filter*. The method should be robust because we expect little dependence on the filter calibration.

The problem of diagnostics of loop plasma from filter ratios, and, more in general, the whole analysis of loop observations are made even more difficult by the inescapable presence of other structures intersecting along the line of sight. A uniform diffuse background emission also affects the temperature diagnostics, by adding systematic offsets which alter the filter ratio values. The task of subtracting this *background emission* from the measured emission is non-trivial and can affect seriously the results of any analysis. The Appendix A includes a technical note, about the importance and different methods to remove background emission, in a TRACE EUV image, in the study of coronal loops.

My work has taken good advantage of the collaboration with Japanese Institution as NAOJ (*National Astronomical Observatory of Japan*) and ISAS/JAXA (*Institute of Space and Astronautical Science - Japan Aerospace and eXploration Agency*), where I stayed, as visiting student, from 01/06/2009 to 01/10/2009, by the HINODE Science Center group of prof.Tsuneta (NAOJ) and by the group of dr.Sakao (ISAS/JAXA).

**NOTE:** Part of the work here presented has been published in refereed journals and presented at international conferences. The analysis of Chapter 2 has been published as Terzo et al. (2011) on *The Astrophysical Journal*. The analysis of Chapter 3 is the subject of an article in preparation to be submitted to *The Astrophysical Journal*. The Appendix A has been already published as Terzo & Reale (2010) on *Astronomy and Astrophysics*.

# Acknowledgements

My gratitude goes to Prof. Fabio Reale for helping and guiding me in my research work. Many thanks to Prof. G.Peres for the helpful discussions. A special thank to Drs. M.Miceli and M.Guarrasi for their precious support and for good working together. I would like to thank Drs. M.Caramazza, M.Guarcello, L.Affer, S.Bonito, C.Argiroffi, C.Gelardi and P.Ballerini for their precious help in OAPA and for their friendship outside. A special thank goes to Prof. S.Tsuneta and his group at the HINODE Science Center, who support me during my Japanese period, introduced me in a very fruitful way to the HINODE/XRT world and to the japanese way of science. Many thanks to Dr. T.Sakao and his group at the ISAS/JAXA for the hospitality and help. My sincere aknowledgements to Drs. H.Hara, Y.Kato, R.Kano, N.Narukage, Y.Katsukawa, J.Okamoto, D.Orozco-Suárez for their kind help and friendship in my japanese period. A special thank to Dr. Y.Sakamoto for the fruitful and helpful discussions in NAOJ. I wish to thank Marie Fujiyoshi and Judit Palacios, for their help in my japanese life.

I wish to acknowledge Dr. J.A.Klimchuk for his help, the illuminating discussions and encouraging words.

I am glad to acknowledge Prof. E.Priest for his esteem for my PhD and research work.

Finally, my warm appreciations to my family and friends for having supported me during these years.

# Contents

# List of Figures

# List of Tables

# Chapter 1

# Introduction

Since the discovery of *"coronium"* and of the million degree solar corona, tens of years ago, generations of authors have tried to solve the problem of coronal heating. This is one of the big questions in astrophysics.

The HINODE mission (Shimizu, 2002; Kano et al., 2004; Golub et al., 2007), launched in September 2006, has provided data of unprecedented quality, and has opened new ways to investigate the solar corona. In particular, the *X-Ray Telescope* (XRT) collects high resolution X-ray images in different filters, and its high cadence observations have enabled the study on intensity variability of the solar corona, offering new opportunities to investigate the features of coronal heating.

My work addresses X-ray data of the solar corona from the HINODE satellite, in the framework of the coronal heating issue, and, in particular, to investigate signatures of nanoflare-heated loops.

## 1.1 Solar Corona

The *photosphere*, the base of the solar atmosphere, is a thin layer of about 300-500 Km thick, which emanates the bulk of the visible radiation. The temperature at the

outher boundary of photosphere is 4500 K, while at the inner boundary is 8000 K. The density also rapidly increase inwards, making the plasma optically thick and so hiding the interior from sight. The next layer outward is the *chromosphere* (Fig.1.1, left panel), a layer roughly 2,000 kilometers thick, with a temperature range from about 4500 K at the inner boundary to 20,000 K at the outher boundary, and with density of $\sim 10^{16}$ particles cm$^{-3}$. Typical chromosperic features are the *spicules*, long thin columns of gas that growning up from the photosphere below.

Spicules rise to the top of the chromosphere and then fall back down over a cycle of about 10 min. Above the chromosphere, the solar atmosphere - through a very thin layer ($\sim$ 500 kilometer wide called *Transition Region*) - reaches the temperature of 1 milion degree and more in the *Solar Corona* (from the latin for *"crown"*). This hot layer is the outest layer of the solar atmosphere that spans for tens of solar radii. The lower corona has a density of about $10^8 - 10^9$ cm$^{-3}$.

Since the photosphere has visible emission of several orders of magnitude greater

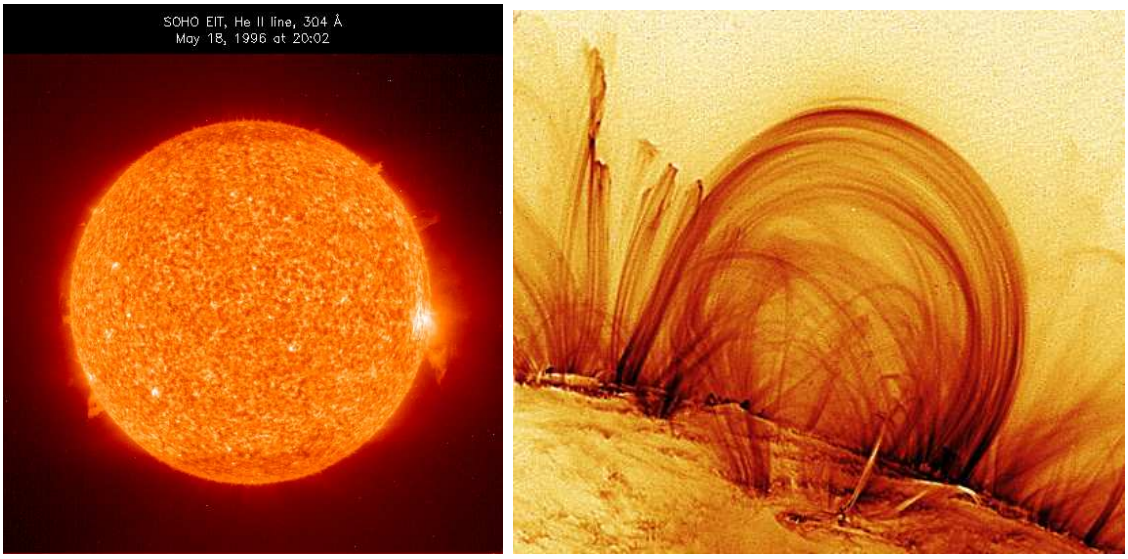


Figure 1.1 The Sun in the He II (304Å) emission line. Credit: SOHO (ESA/NASA), (left panel); Image of Coronal loops, observed by TRACE satellite in 171Å filter (right panel), (Sec.A.2.1).

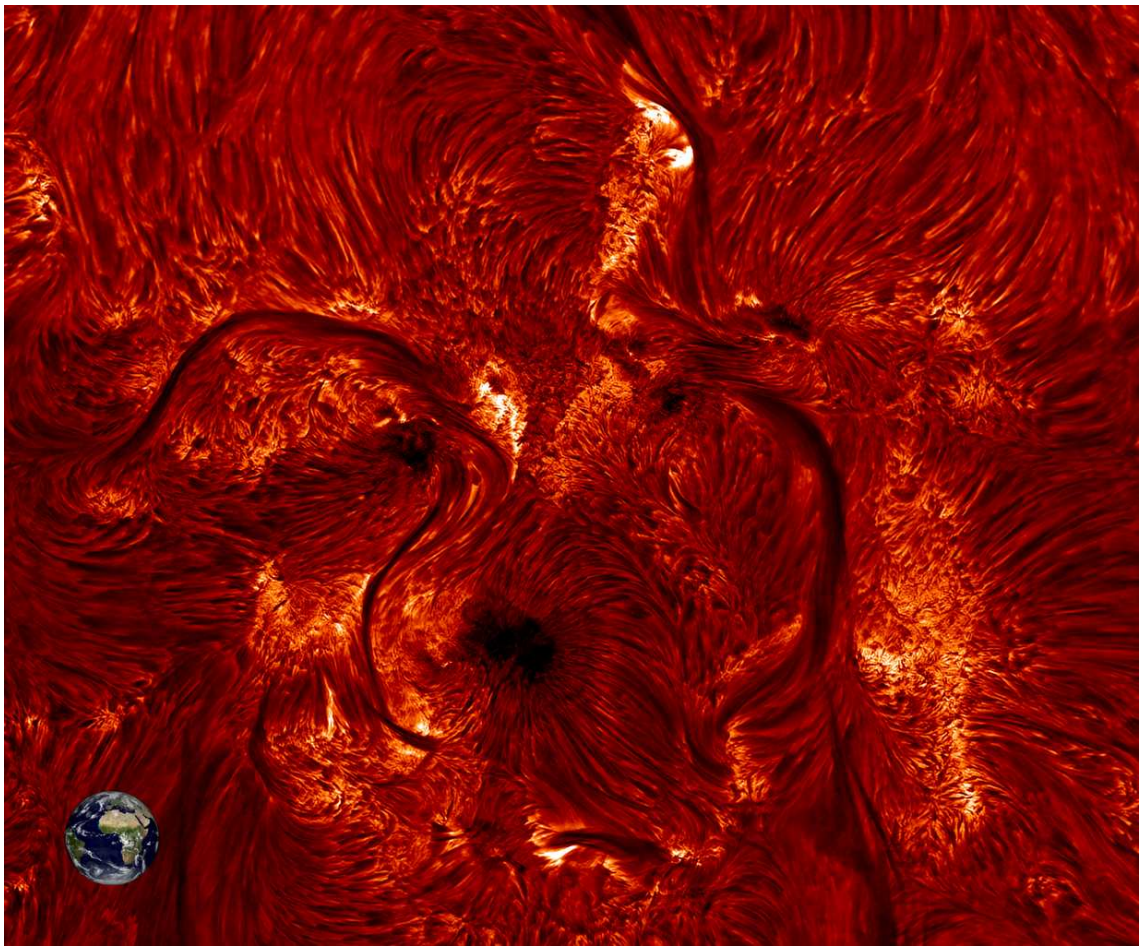

Figure 1.2 Active Region AR10786 observed in H$\alpha$ by DOT (Dutch Open Telescope), 8 July 2005. The field of view is of $182 \times 133$ arcsec. The earth image is just for dimension scale.

than the corona, the latter is completely invisible to the naked eye. Due to the lucky coincidence that the angular size of the Moon is almost the same of the sun-disk, the corona becomes directly observable in visible light only during the total eclipse of the sun, as a pale halo that rings the sun-disk.

At the soft-X-rays wavelength ($0.1 - 1$ nm) the solar corona has thermal emission and, because in this band the contribution of lower layer of solar atmosphere is minor, it could be observed directly. Anyway at these wavelengths the emission of the solar

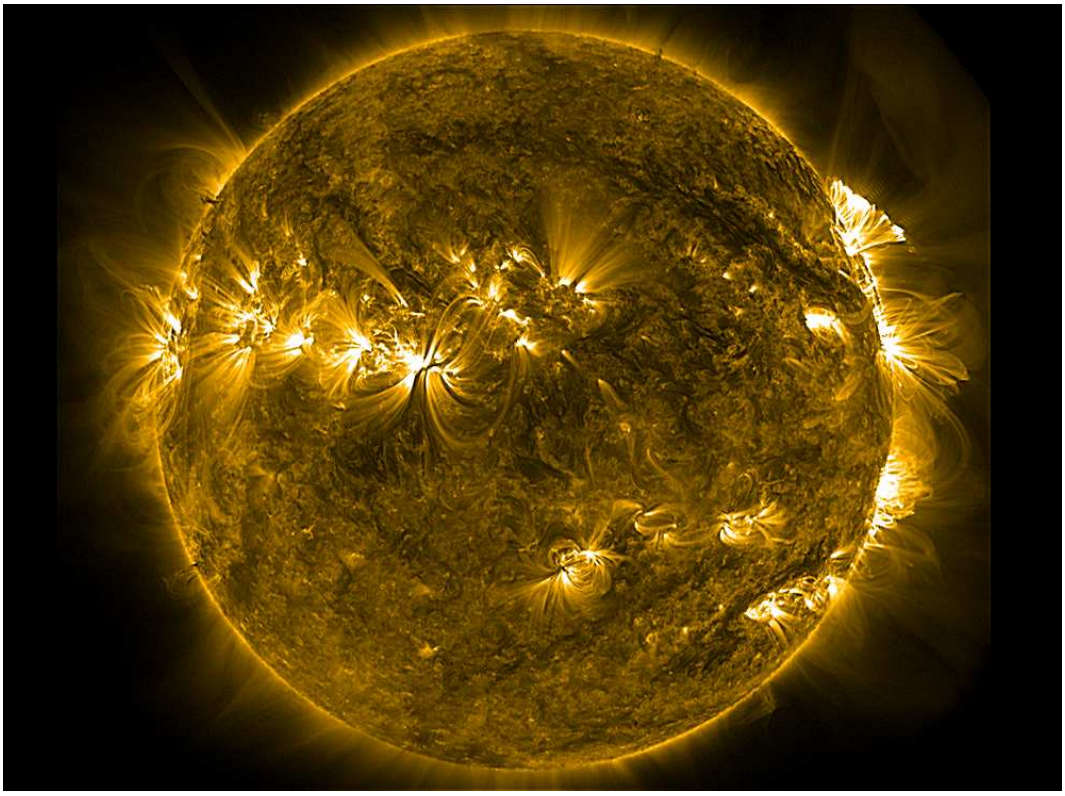

Figure 1.3 The Sun observed by *Solar Dynamic Observatory* in the 171Å filter (ref. Sec.1.4.2), at the wavelength of extreme ultraviolet light, with typical open and closed structures (*active regions*, *coronal loops*).

atmosphere is absorbed by the earth atmosphere. Spaceborn instrumentation and satellites (i.e. *Skylab*, 1973), have allowed us the direct observation of the on-disk corona, outside of solar eclipses.

In the soft-X-rays wavelength, among the main features of the solar corona I mention two different kinds of regions: highly sub-structured *active regions* (Fig.1.2 and Fig.1.3) with bright X-ray emission, and full of closed magnetic flux tubes (*coronal loops*) anchored in the photosphere and extending over in the atmosphere in an intricate carpet (Fig.1.1, right panel); and regions with open field lines and with fainter emission (*coronal holes*), (Priest, 1982).

Since the Corona is optically thin in the X-ray band, it appears very intricate with

many structures and characteristic features that overlap along the line of sight. With the current instrumental resolution ($\sim$ 1 arcsec), these structures can be resolved and studied in good detail. At this point a very challenging problem is to disantangle single structures from the others intersecting along the line of sight and from the foreground and *background emission*.

## 1.2 Coronal Heating

How the solar corona is heated to several million degrees Kelvin is one of the most compelling question in space science. Simple thermal conduction from below is clearly not the answer, since the corona is more than two orders of magnitude hotter than the solar surface.

The million degree plasma of the corona is fully ionized, and therefore strongly coupled with the solar magnetic field. The solar magnetic field then has an important role in the dynamics and structure of the outer solar atmosphere, and in the release of the energy for its heating. Nowadays, it is widely believed that the energy source for coronal heating is the magnetic energy stored in the solar corona. But an unsolved problem is how this magnetic energy could be converted into thermal energy of the coronal plasma. Mechanical motion of the lower part of the solar atmosphere is widely accepted as the first source for this energy. These motions displace the footpoints of the magnetic field lines, generating magnetic stresses or waves depending on the timescale of the motion, longer or shorter of the end-to-end Alfvén travel time (Klimchuk, 2006a).

Rapid pulses called *nanoflares* are among the best candidate mechanisms of magnetic energy release (Sec.1.3.3), in particular for coronal loops (Parker, 1988; Reale, 2005; Reale et al., 2005). It has been proposed that nanoflares may be extremely localized since each coronal loop is structured into very thin strands. In this case the detection and diagnostics of nanoflares may very difficult for a variety of reasons (Sec.1.5), (Klimchuk, 2006a).

Since the radiative and conductive losses of the solar corona have a flux of about $10^7$ ergs cm$^{-2}$ s$^{-1}$ for the active regions and $3 \cdot 10^5$ ergs cm$^{-2}$ s$^{-1}$ for the Quiet Sun, whatever mechanism heats the corona must account for this strong energy *losses* from both downward thermal conduction and radiation and in turn each theory for the coronal heating has to respect this energetic condition.

Nanoflares themselves present many unsolved questions: their time and space variation, their dependence on physical parameters, like field strength or line field's length.

To answer these compelling questions, the issues to address span from the identification of the energy sources, to the mechanisms of conversion of this energy into heat, ending with prediction of observables quantities to compare directly with real observations.

## 1.3 Study of Temporal Variability

The solar corona is the site of a variety of transient phenomena. Coronal loops – that do not flare in active regions – remain in a steady state for most of their life (up to tens of days), much longer than the plasma characteristic *cooling times* (Rosner et al., 1978b), that we will summarize in the following.

If the plasma of a coronal loop cools down due to efficient *thermal conduction* (Cargill, 1994a), the time scale (s) is:

$$\tau_c = \frac{3 n_c \kappa_B T_0 L^2}{2/7 \kappa T_0^{7/2}} = \frac{10.5 n_c \kappa_B L^2}{\kappa T_0^{5/2}} \approx 1500 \, \frac{n_{c,9} L_9^2}{T_{0,6}^{5/2}} \tag{1.1}$$

where $n_c$ is the particle density ($n_{c,9}$ in units of $10^9$ cm$^{-3}$), $T_0$ is the loop maximum temperature ($T_{0,6}$ in units of $10^6$ K), $L$ is the loop half-length ($L_9$ in units of $10^9$ cm), with thermal conductivity $\kappa = 9 \cdot 10^{-7}$ (in c.g.s. units).

If plasma with high density $n_M$ ($n_{M,9}$ in units of $10^9$ cm$^{-3}$) comes up from the chromosphere, the time scale (s) becomes that of *radiative cooling*:

$$\tau_r = \frac{3 \kappa_B T_M}{n_M P(T)} = \frac{3 \kappa_B T_M}{b T_M^{\alpha} n_M} \approx 3000 \, \frac{T_{M,6}^{3/2}}{n_{M,9}} \tag{1.2}$$

where $T_M$ is the temperature of the plasma ($T_{M,6}$ in unit of $10^6$ K), at the time when the density has the $n_M$ value, and where $P(T)$ is the *plasma emissivity* per unit emission measure, expressed as:

$$P(T) = b T^{\alpha} \tag{1.3}$$

with $b = 1.5 \cdot 10^{-19}$ and $\alpha = -1/2$, where $P(T)$ is in unit of W m$^{-3}$. Serio et al. (1981) (and refined by Reale, 2007) derived a global thermodynamic decay time that combines both time scales above:

$$\tau_s = 4.8 \times 10^{-4} \frac{L}{\sqrt{T_0}} = 500 \frac{L_9}{\sqrt{T_{0,6}}}. \quad (1.4)$$

where $T_0$ is the loop maximum temperature ($T_{0,6}$ in units of $10^6$ K), $L$ is the loop half-length ($L_9$ in units of $10^9$ cm).

The long lifetime of coronal loops could be taken as proof that a heating mechanism must be on and steady, long enough to sustain the loop to an equilibrium condition, stable for their lifetime. Anyway, the emission of the solar corona is found to vary significantly on various timescales, and the temporal analyses of coronal loop data (in particular) have been used to obtain different kinds of information, and to characterize the dynamics and possible mechanisms of heating (Reale, 2010).

The interpretation of the time variability of coronal emission is in general not easy. The sensitivity of the emission of coronal plasma to density more than to temperature, implies that the variations are not direct signatures of heating episodes but, since the plasma is free to move along the lines of the magnetic fields, of local compressions. Variations must therefore be explained in the light of the evolution of the whole loops. This needs, however, accurate modeling or attention to many relevant and concurrent effects. The instrumental band is also very important. The EUV bands of the normal incidence telescopes are quite narrow. Observations are then more sensitive to variations because cooling or heating plasma is seen to turn on and off rapidly as it crosses the band sensitivity. Telescopes in the X-ray band (grazing incidence) detect hotter plasma which is, in principle, more sensitive to heating and therefore expected to vary more promptly, but the bandwidths are large and do not take as much advantage of the temperature sensitivity as the narrow bands. Lastly, spectroscopic observations are, theoretically, very sensitive to temperature variations since they observe single lines, but their time cadence is typically low and able to follow variations only on large timescales.

### 1.3.1 Wave Heating

For many years, high frequency acoustic waves had been suggested as source of mechanical heating in the solar atmosphere. It was thought that the existence of the chromosphere itself depends on a time-constant energy supply provided by mechanical heating. High frequency oscillations have been observed and analyzed since this explanation was first suggested. The observed intensity oscillations, and energy they carry have been long discussed (Liu, 1974), concluding that the observed energy is insufficient to account for the chromospheric losses. Moreover the origin of the oscillations is still not clear (Moretti et al., 2001).

Turbulent motion of the photosphere could put in motion the footpoints of the magnetic field lines, generating a flux of upward propagating waves. The mode mixing between different kind of waves (Alfvén, magnetosonic, kink, sausage) could generate an amount of energy of more than $10^7$ ergs cm$^{-2}$ s$^{-1}$. But only a small fraction of these waves are able to pass through the steep gradients of temperature and density in the chromospere and transition region. Acoustic and slow-mode waves are damped due the formation of shocks, fast-modes instead are reflected and refracted. Alfvén waves, including torsional and kink tube waves, are able to pass through and reach the corona. But observation results show that Alfvén waves are responsible only for energy injection $\leq 10^7$ ergs cm$^{-2}$ s$^{-1}$, that is only marginally adequate to the active regions losses. Instead Parker (1991), argued that solar convection is not very efficient in generating Alfvén waves. Most Alfvén waves are strongly reflected in the chromospere and the transition region, but a significant transmission is possible only within narrow frequency bands of loop resonance. The problem of transmission is automatically over for waves generated directly in the corona. The existence of waves in corona is well established, but the real issue is whether these waves are able to carry enough energy to heat the corona to million degrees. At the end our lack of knowledge about the basic properties of coronal

waves is the greatest obstacle to deepen our comprehension of wave coronal heating (Klimchuk, 2006a).

### 1.3.2 Spicules

Discrete coronal heating events so-called spicules are right now attracting attention for the coronal heating problem.

These jets propel into solar corona a chromospheric mass flux that is estimated to be two orders of magnitude larger than the mass flux of the solar wind. But a coronal counterpart of them had not been observed, even if they have been revealed in a variety of lines of Chromosphere and Transition Region. So coronal heating due spicules drive mechanism had been dismissed as unlikely.

Recently some authors have observed a new kind of spicules that live for a shorter period ($\sim$ 100 s) and are more dynamic ($\sim$ 50 to 100 km/s) than its classical counterpart.

A spatio-temporal correlation between chromospheric brightness changes, linked to these *"type II"* spicules, and coronal upflows of 50 to 100 km/s, deduced from spectral line asymmetries of coronal lines at the footpoints of loops, was found by the previous authors, which considered the statistical relationship suggesting that the chromospheric jets may play a substantial role in providing the corona with hot plasma. Anyway a detailed one-to-one correlation between spicules and their coronal counterparts has remained elusive (De Pontieu et al., 2011).

### 1.3.3 Impulsive Heating

For many years it has been assumed that the high temperature of the solar corona could be explained by a steady dissipation of energy transported from the turbulent photosphere. A variety of mechanisms was proposed, such as Alfvén wave dissipation (Sec.1.3.1), anomalous current disruption (Tucker, 1973), and reconnection (Rosner et al., 1978a).

Other authors, on the other hand, developed a parallel vision that the corona was not heated in steady manner, but with series of impulsive energetic events. We believe that these impulsive events are the most promising explanation of coronal heating. Parker (1983) said: *"the idea that the active corona is heated largely by dissipation of the convolution of the coronal magnetic fields has been around for nearly 20 years"*. Afterwards himself (Parker, 1988) proposed a new picture of tangled magnetic fields. Soft X-ray and EUV images of the corona reveal infact many beautiful loop structures—arched magnetic flux tubes filled with plasma. Many tens to hundreds of unresolved strands are proposed to be bundled together within a single coronal loop as observed, as example, by HINODE or SDO satellite.

These elemental *fibrils* (Gomez et al., 1993; Reale, 2010), are anchored with their footpoints in photosphere and shuffled around, wrapped and braided by the footpoint motions (i.e. *convection* and *supergranulation*). The turbulent convection of the solar surface randomly shuffle the kilogauss photospheric magnetic flux tubes. Current sheets form at the interfaces where the tubes are misaligned, and when the stresses and currents become too large, in the so-called *X-neutral points*, the magnetic energy is released impulsively.

#### Nanoflares

Hard X-ray observations Lin et al. (1984) suggest that energy could be released in bursts of $10^{27}$ ergs. These events, that was $10^{-6}$ times with respect to major events

(as *flares*), was called *microflares*. But authors (Parker, 1988) noted that these microflares were composed by much smaller elemental energy release, of the order of $10^{24}$ ergs. The latters were referred as *nanoflares*.

But this does not mean that any event releases just $10^{24}$ ergs, it is just a typical number. The number of flares however (Drake, 1971), fall off with increasing peak flux as power law, with slopes of $\sim 1.8$ for the differential distribution. But, to account for the coronal radiative losses ($10^7$ ergs cm$^{-2}$ s$^{-1}$), there must be a more significant increase in the number of events per amount of energy release at the nanoflares level ($\sim 2.$), than the extrapolation from the microflares data would indicate (Hudson, 1991).

Since the average coronal energy is approximately $10^7$ ergs cm$^{-2}$ s$^{-1}$, if the nanoflare energy is $10^{24}$ ergs, the heating of part of an active region (as example $10^{18}$ cm$^2$), requires 10 nanoflares per second (Cargill, 1994a). We could consider that a large-scale part of the solar corona could be composed of many small elemental loops, with cross sectional area of $A_h$, and that each nanoflare event should happen in a single tiny loop. If the average energy in a nanoflare is $Q$ , in order to account for the heating of an active region, each elemental loop is required to be re-heated on a time-scale of:

$$\tau_{nano} = \frac{Q}{\lambda\, A_h} \tag{1.5}$$

If as example $A_h = 10^{14}$ cm$^2$, $\lambda = 10^7$ ergs cm$^{-2}$ s$^{-1}$, and $Q = 10^{-24}$ ergs, then $\tau_{nano} = 1000$ s. So an important parameter is the ratio between $\tau_{nano}$ and the characteristic cooling time of the loop. To be steady and visible the loop should be re-heated before the plasma cools down.

Identifiable warm loops, observed in the corona, account for only a small fraction of the coronal plasma. Recent observations have revealed that small amounts of extremely hot plasma are widespread in active regions (Reale et al., 2009) and

consistent with the predictions of theoretical nanoflare models (Patsourakos & Klimchuk, 2008; Guarrasi et al., 2010). This suggests that nanoflare heating may indeed be universal. However, the conclusion is far from certain (Brooks & Warren, 2009). My Phd work has tried to sheds new light on this fundamental question.

## 1.4 Recent and Past Missions for Coronal Varibility Studies

The **Skylab** mission launched into Earth orbit by a Saturn V rocket on May 14 1973 was the first mission of a major maturation in out-atmosphere solar physics. After that it was a continue run to better resolution in space and time, from Yohkoh to HINODE, from TRACE to SDO.

The high time coverage and resolution of **Yohkoh** (1991-2002) enabled studies of brightenings on short time scales. The Yohkoh/SXT resolution and dynamic range allowed to study the interaction of differently bright hot loops and to show, for instance, that X-ray bright points often involve loops considerably larger than the bright points themselves, and that they vary on timescales from minutes to hours (Strong et al., 1992).

Variability analyses have been conducted also on warm loops present in **TRACE** data (1998-2010). In an observation of more than 2 hours with a cadence of about 30 s, Reale (2002a) analyzed in detail the brightening of a single coronal loop. The loop evolves coherently in the rise phase and brightens from the footpoints to the top, allowing for detailed hydrodynamic modeling (Reale, 2002b). Active region transient events, i.e., short-lived brightenings in small-scale loops, were observed with TRACE with a high cadence of 35 s over half an hour (Seaton et al., 2001).

The analysis of temporal variations, from recent solar missions, has been used to investigate the possible presence of continuous and widespread heating pulses (i.e. the *nanoflares*). The temporal evolution of hot coronal loops was studied in data taken with **GOES** *Solar X-ray Imager* (SXI), an instrument with moderate spatial resolution and spectral band similar to Yohkoh/SXT (López Fuentes et al., 2007). The durations and characteristic timescales of the flare-like evolution (*emission rise, steady, and decay phases*) were found to be much longer than the plasma cooling

time, and indicate that the loop-averaged heating rate increases slowly, reaches a maintenance level, and then decreases slowly. This slow evolution is taken as a possible proof of a single heating mechanism operating for the entire time that the loop lives. From the analysis of the auto-correlation functions in SXT and TRACE loop observations (Sakamoto et al., 2008), the duration of the intensity fluctuations for the hot SXT loops was found to be relatively short. This because of the significant photon noise, but that for the warm TRACE loops agrees well with the characteristic cooling timescale. This may support loops to be continuously heated by impulsive nanoflares. The estimate of the energy of nanoflares is $10^{25}$ erg for SXT loops and $10^{23}$ erg for TRACE loops. The corresponding occurrence rate is about 0.4 and 30 nanoflares $s^{-1}$ in a typical hot SXT loop and a typical warm TRACE loop, respectively.

A recent study on time series has been performed on data taken with the **Hinode** mission. Hinode's Solar Optical Telescope (SOT) magnetograms and high-cadence EIS spectral data were taken to study the relationship between chromospheric, transition region, and coronal emission and the evolution of the magnetic field (Brooks et al., 2008).

Finally in my work of PhD I applied, for the first time on HINODE/XRT high cadence data, e new kind of varibility analysis with statistical methods.

### 1.4.1 Hinode Mission

The *Hinode* satellite (**Solar-B**) of the *Institute of Space and Astronautical Science, Japan Space Exploration Agency* (ISAS/JAXA) is the third japanese mission dedicated for solar physics, launched on 22 September 2006, 21:36 GMT, from *Kagoshima* Space Center (*KSC-ISAS*) and put in circular polar sun-synchronous orbit by *M-V ISAS* rocket, (Shimizu, 2002). The principal scientific instruments on board on the HINODE satellite (Fig.1.4) are:

- The *Solar Optical Telescope* (SOT), that provides quantitative measurements of full vector magnetic fields at photosphere with spatial resolution of 0.2-0.3 arcsec;

- The *X-Ray Telescope* (XRT), with the capability of obtaining high spatial and temporal resolution synoptic images;

- The *EUV Immaging Spectrometer* (EIS), that allow to measure physical conditions of coronal hot plasma fluxes.

All telecopes are equiped with dedicated CCD. Scientific data are managed and downlinked by the *Mission Data Processor* (MDP). Data aquired by the instruments on board on the Hinode satellite are downlinked 4 times a day by Uchinoura Space Center station as well as Norvegian high-latitude ground station at Svalbard. These telescopes are connected with *Focal Plane Package* (FPP) of analysis instruments

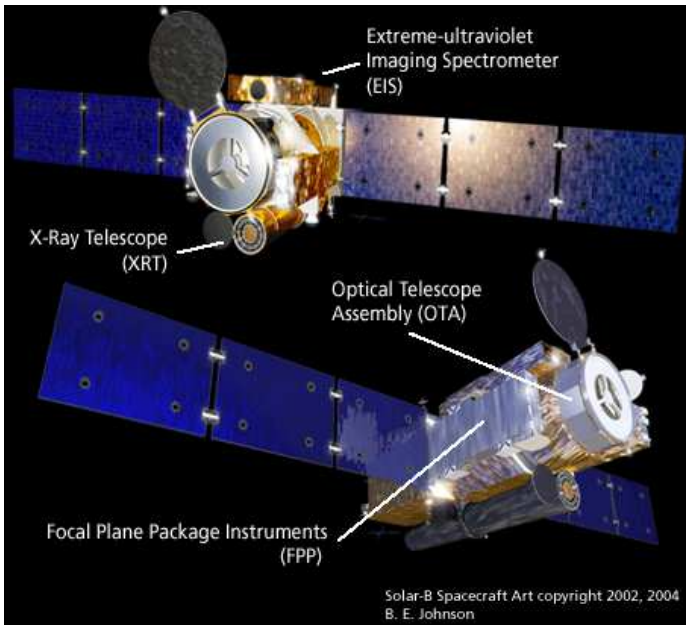


Figure 1.4 The HINODE spacecraft, with labeled the principal scientific instruments on board of it.

(filters, spectro-polarimeters).

The SOT consists of the *Optical Telescope Assembly* (OTA) and a *Focal Plane Package* (FFP). The OTA is a 50-cm diffraction-limited Gregorian telescope, with $0.2 \sim 0.3$ arcsec spatial resolution in $388-668$ nm band, with the capability to resolve photospheric tubes, with the aim to obtain more insight in the physical processes that works inside them. FFP includes narrowband and broadband philtergraph (NFI, BFI), and a Stokes Spectro-Polarimeter (SP). The main task of the SOT is to obtain a continuous series of diffraction-limited images, while being free from the conditions of atmospheric seeing, and to make highly accurate measurements of vector magnetic fields at the photosphere (Shimizu, 2002).

The EIS is a scanning mirror single-slit spectrograph, designed to observe plasmas in the temperature range from the upper Transition Region (0.1 MK) to the lower Corona (10 MK). The EIS is coupled with two back-illuminated CCD detectors, that cover the wavelength ranges of $170 - 210$Å and $250 - 290$Å, chosen on purpose for diagnostics of coronal plasma and flares.

### X-Ray Telescope (XRT)

The XRT was designed and developed by the Japan-US collaboration between Smithsonian Astrophysical Observatory (SAO), NASA MSFC, JAXA, and NAOJ. The XRT CCD camera was tested and calibrated in X-rays at the Advanced Technology Center of the NAOJ with JAXA.

The X-Ray Telescope (XRT) (Golub et al., 2007) is a grazing-incidence soft X-ray telescope (Fig.1.5a), which is sensitive to the emission of plasma in the temperature range $6.1 < \log T < 7.5$. XRT major technical parameters and specifications are reported in Table 1.1, (Kano et al., 2004). Several temperature passbands are provided by a selection over nine different filters in the X-ray band plus one in the optical G band continuum. These are held in two filter wheels (FW1 and FW2) lo-

cated close to the focal plane in front of the CCD camera (Fig.1.5b). The latter has a 1 arcsec pixel and the Full-Width-Half-Maximum (FWHM) of the Point Spread Function (PSF) is $\approx 0.8$ arcsec. The field of view is $34 \times 34$ arcminutes. XRT is sensitive in a bandwidth of frequency that corresponds to a range of temperatures $<$1 MK to 20 MK.

The spatial resolution of the grazing-incidence telescope strongly depends on the length of the telescope itself; XRT covers nearly the entire dimension of the satellite ($\sim$ 3.80 m), obtaining a spatial resolution of 1 arcsec. The *back illuminated* CCD of $2048 \times 2048$ pixel extends the sensitivity of the instruments to longer wavelength, beyond the wavelength sensitivity of precedent generation satellites (i.e. *YOHKOH/SXT*), and allows to cover the entire sun disk in a single observation (Kano et al., 2004).

Table 1.1 XRT (*X-Ray Telescope*), Major technical parameters and specifications.

| | |
|---|---|
| Optical design | Wolter-I |
| Mirror | 34 cm ø |
| Focal Lenght | 2708 mm |
| Wavelength range | $3 - 200$ Å (Al_thin filter; 1500 Å) |
| | $<$60Å other filters |
| Detector | Marconi Applied Technologies |
| | back-illuminated CCD |
| | $2K \times 2K$, (pixel 13.5 $\mu$m), at $-40°$ C |
| Field of View | 34 arcmin $\times$ 34 arcmin |
| Temperature Range | $1 - 20$ MK |
| Standard Exposure Time | 0.01 s (flares) - 200 (coronal holes) s |
| Standard Temporal Resolution | 10 s (partial frame) - 100 s (full frame) |

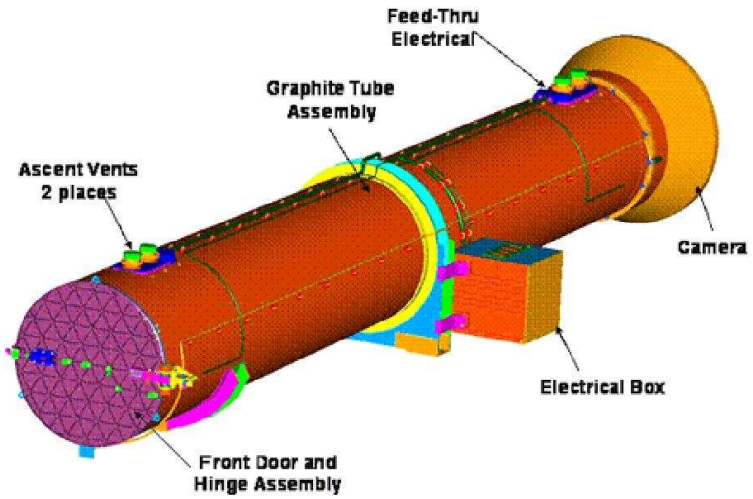


(a)

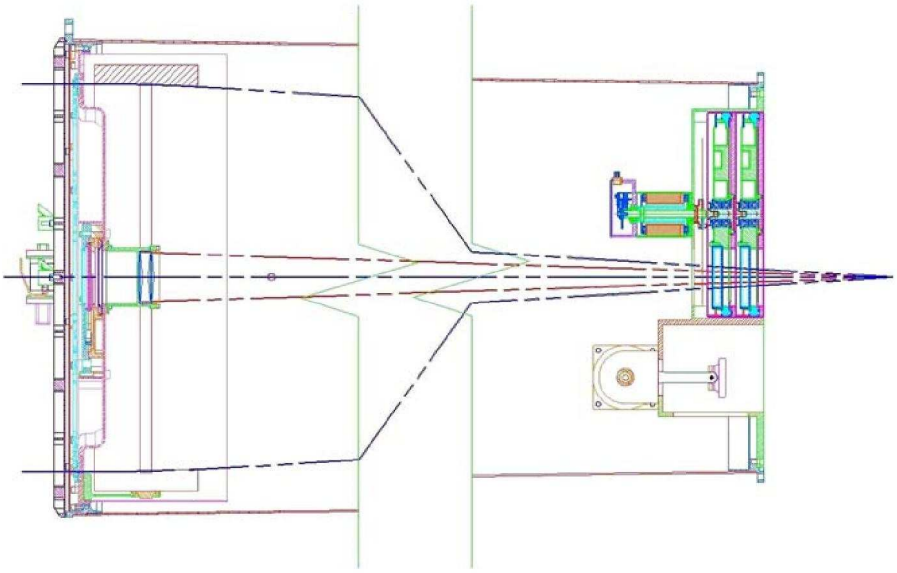

(b)

Figure 1.5 (a) Major components of the X-Ray telescope. (b) A diagram of the X-Ray grazing incidence-telescope, in which is visible, in the upper right part of the scheme, the package with the two wheels of analysis filters.

### Pre-filters and Filters

On the entrance aperture of XRT and on its focal plane there are two sets of different filters (Fig.1.5b). Thin *pre-filters* cover the annular region of the entrance aperture of the telescope (Fig.1.6), to reduce the incoming light and also to prevent the heating of the instrument itself. These pre-filters consist of 1200 Å of Al and 2500 Å of a Polyimide film, with a layer (100 Å) of $Al_2O_3$. The analysis filters are instead on the focal plane with two principal scientific aims:

1. To reduce the incoming light in the grazing-incidence telescope;

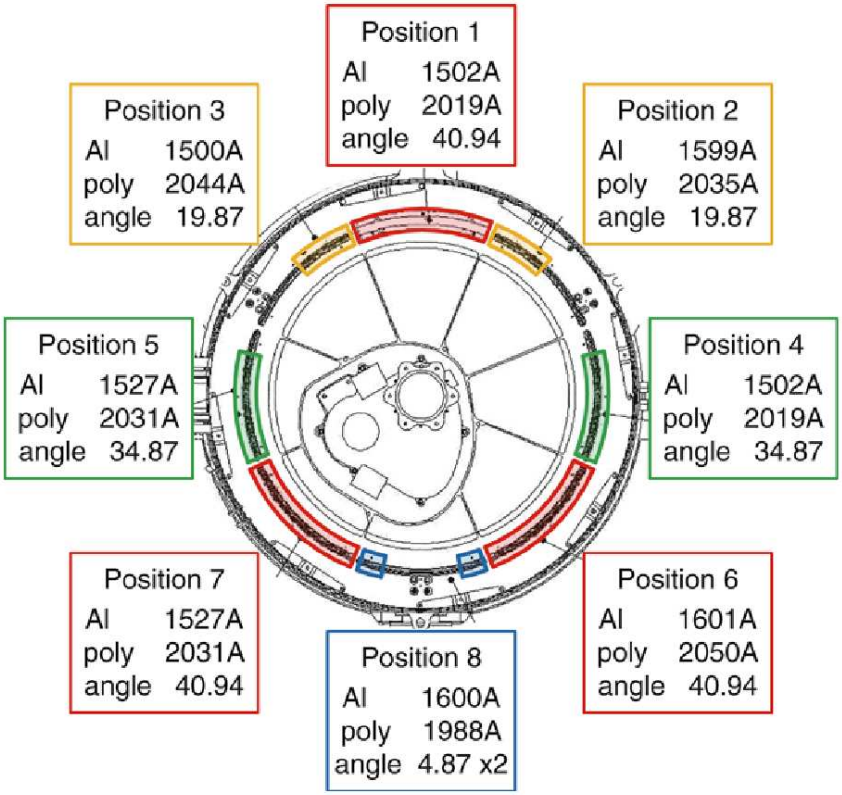


Figure 1.6 Pre-filters on the entrance aperture of XRT. Pre-filters are fun-shape segment that consists of aluminum on polyimide film. In the figure are summarized too the filters thicknesses and the opening angles (Narukage et al., 2011).

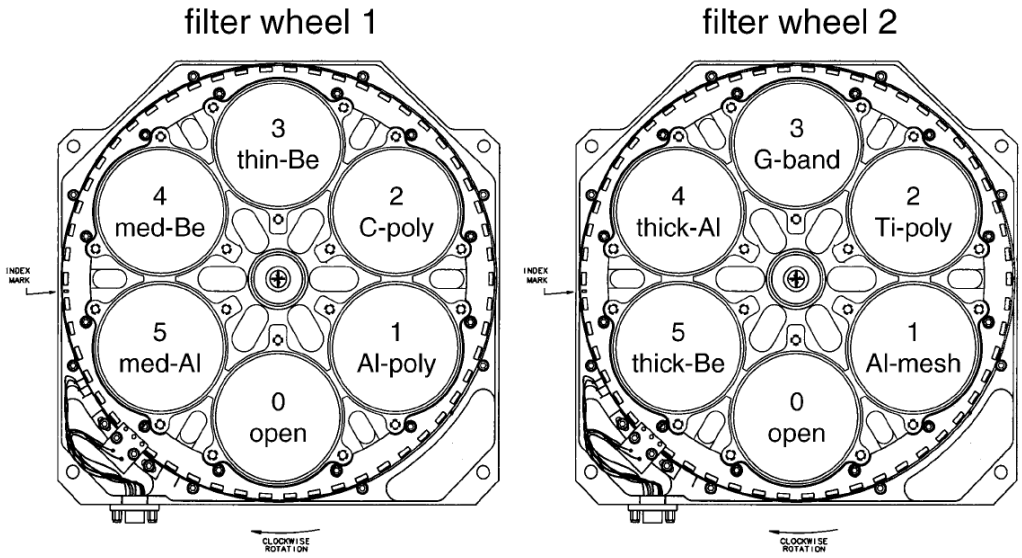


Figure 1.7 The figures show filters wheels on the focal plane of XRT. The left panel shows the outer wheel, closer to the mirror; the right panel shows the inner wheel, closer to the CCD.

2. To supply multiple pass-bands in different X-ray wavelength, for plasma diagnostics.

The nine analysis filters are nested in two wheels (Fig.1.7) in front of the CCD camera near the focal plane of XRT (Fig.1.5b). These filters extend the dynamical range of XRT, and differs in thickness by a factor of $10^4$. Thin filters are useful for fainter structures observations, while thick filters are suitable for stronger phenomena with intense emission as *Flares*. These filters put on the optical path of light inside the instrument bound the spectral response. By folding the filtered effective area with the model plasma spectra, we can obtain the XRT temperature response for each filter (Fig.1.8). The XRT focal plane filters were tested and calibrated also in Palermo at the *XACT (X-ray Astronomy Calibration and Testing)* of *INAF-Osservatorio Astronomico "G.S.Vaiana"*, in particular regarding the transmission properties and

spatial uniformity. In Table 1.2 the specifications and physical properties of the Focal Plane Filters of XRT are shown (Golub et al., 2007; Narukage et al., 2011).

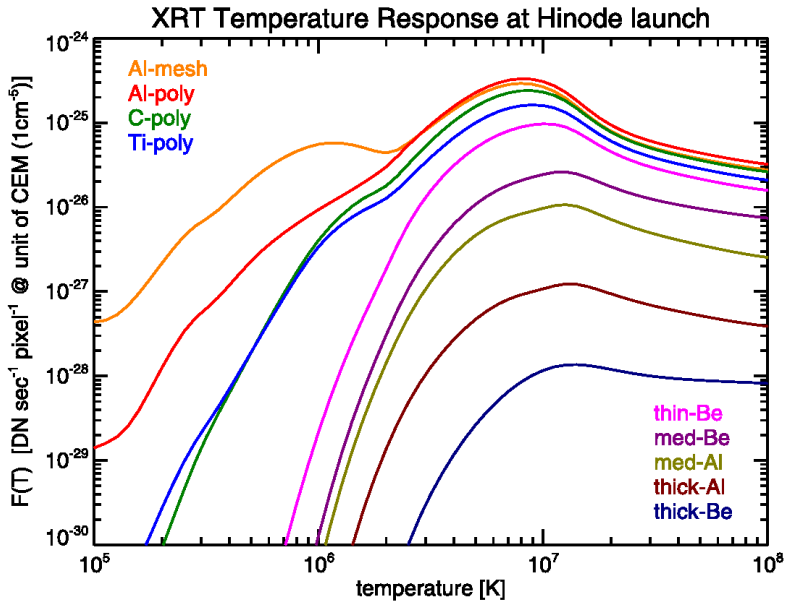


Figure 1.8 The figure show the total XRT temperature response functions, for all the X-ray focal-plane filters. The curves plot the combination of the total instrument response (as function of wavelength) with the coronal plasma emission model (ATOMDB/APEC) for a columnar EM of $10^30\ cm^{-5}$ in unit of wavelength (Narukage et al., 2011).

Table 1.2 Physical characteristics of the HINODE/XRT focal plane analysis filters.

| **Filter ID** | **Material** | **Thick. Å** | **Filter Support** | **Thick. Å** | **Oxide** | **Thick. (tot. Å)** |
|---|---|---|---|---|---|---|
| *Al-mesh* | Al | 1600 | - | 82% | *Al2O3* | 150 |
| *Al-poly* | Al | 1250 | Poliymide | 2500 | *Al3O3* | 150 |
| *C-poly* | C | 6000 | Poliymide | 2500 | N/A | N/A |
| *Ti-poly* | Ti | 3000 | Poliymide | 2300 | TiO2 | 100 |
| *Be-thin* | Be | 9*e*4 | N/A | N/A | BeO | 150 |
| *Al-med* | Al | 1.25*e*5 | N/A | N/A | Al2O3 | 150 |
| *Be-med* | Be | 3.0*e*5 | N/A | N/A | BeO | 150 |
| *Al-thick* | Al | 2.5*e*5 | N/A | N/A | Al2O3 | 150 |
| *Be-thick* | Be | 3.0*e*6 | N/A | N/A | BeO | 150 |

### 1.4.2 SDO Mission

Solar Corona as observed by precedent missions as Yohkoh, SOHO (*Solar and Heliosperic Observatory*), SECCHI (the Sun Earth Connection coronal and Heliospheric Investigation), STEREO (Solar Terrestrial Realations Observatory), TRACE (*Transition Region And Coronal Explorer*), HINODE shows evolution in its structures, in density, temperature and position in timescales of the seconds. These conditions depend on *local* conditions and in particular on the magnetic condition of field lines.

The SDO (*Solar Dynamics Observatory*) is the first mission to be launched within NASA's *Living With a Star* (LWS) Program, a program designed to understand the causes of the solar variability and its influence on life and society. SDO is designed to

Figure 1.9 The Solar Dynamic Observatory with evident the AIA telescopes as seen mounted on the SDO spacecraft's instrument module.

help us understand the Sun's influence on Earth and Near-Earth space by studying the solar atmosphere on small scales of space and time and in many wavelengths simultaneously (Lemen et al., 2011). SDO was launched on 11 February 2010, 10:23 am EST on an Atlas V from SLC 41 from Cape Canaveral.

The SDO instruments are focused on determining how and why the Sun varies and their implication on global change and space weather. The SDO scientific experiments are (Fig.1.9):

- Atmospheric Imaging Assembly (AIA)
- EUV Variability Experiment (EVE)
- Helioseismic and Magnetic Imager (HMI)

These three instruments observe the Sun simultaneously, performing the entire range of measurements necessary to understand the variations on the Sun. SDO is a sun-pointing semi-autonomous spacecraft that will allow nearly continuous observations of the Sun with a continuous science data downlink rate of 130 Megabits per second (Mbps). The spacecraft is 4.5 meters high and over 2 meters on each side, weighing a total of 3100 kg (fuel included). SDO's inclined geosynchronous orbit was chosen to allow continuous observations of the Sun and enable a high data rate through the use of a single dedicated ground station.

## 1.5 Problems in nanoflares detection

A magnetic strand that is heated by a nanoflare evolves in a well defined manner. Its light curve (intensity vs. time) has a characteristic shape (Reale, 2007). The intensity rises quickly as the nanoflare occurs, levels off temporarily, then enters a longer period of exponential decay as the plasma cools with proper time scales (eq. 1.4). If we could isolate individual strands in real observations, it would be easy to establish whether the heating is pulsed or steady. Unfortunately, this is not the case. The corona is optically thin, so each line of sight represents an integration through a large number overlapping translucent strands, nonetheless it may be possible to infer the presence of nanoflares. The nanoflares observation is difficult due to a merging of different causes: i) insufficient spatial resolution, we expect an individual nanoflare to occur in a thin loop strand, under the resolution of available instrument ($\sim$ 1 arcsec); ii) insufficient time resolution, it is difficult to resolve the expected very fast rise of a nanoflare, we can only hope to detect the slower exponential; iii) low emission, during the heat pulse the density and therefore the emission of the plasma is typically very low; iv) efficient thermal conduction, the temperature is rapidly made uniform all along the loop, inhibiting the localization of the heating site.

These problems lead to the need of specific indirect methods to obtain some proof of their existence, which are the target of the present work.

## 1.6 Scientific Aims of the Thesis

The solar corona is highly structured by the solar magnetic field and is hot ($\geq 10^6$ K). It is widely accepted that the origin of the heating of the hot plasma confined in the closed coronal structures (named *loops*) lies in the magnetic field (Vaiana et al., 1973). The determination of the fine thermal structure of the corona is crucial to solve the question of the detailed origin of the coronal heating. For

instance, it is currently under debate whether frequent small and rapid heating episodes (*nanoflares*) (Parker, 1988; Cargill, 1994b; Cargill & Klimchuk, 2004), are entirely able to heat the solar corona or partly or only negligibly (Klimchuk, 2006b). The solar *active regions* are good laboratories to investigate this, because they are bright and include a wide variety of structures.

My PhD work was intended to obtain more insight in the framework of coronal heating, coronal substructuring, coronal plasma physics and improvement of methods and techniques for the study of the solar corona. I explored new methods of analysis and improved older ones. During my work I took good advantage of the collaboration with italian (INAF, ASI) and foreigner Institutions (NAOJ, ISAS/JAXA, NASA) and collegues.

## 1.7 Outline of the Thesis

In the following we examine coronal intensity fluctuations, observed by HINODE satellite, to obtain insight in the framework of coronal heating, and to infer the presence of impulsive events as nanoflares, with the guiding idea that if these impulsive events happens, they should leave their *signature* on the light curves (Chapter 2).

One of the approaches I pursued is to study the time variability of the coronal structures, and to search for systematic effects in noisy background light curves. We apply specific methods for the time analysis (Sakamoto et al., 2008) to Hinode observations made of sequences of fast cadence images.

Besides we use these X-ray intensity fluctuations to obtain, the temperature map in an active region with a single filter method (Chapter 3).

As Appendix A we report a side work about the importance of remove background emission, in a TRACE EUV image, in the study of coronal loops, and about advantages and disadvantages of different methods of background subtraction.

# Chapter 2

# X-Ray Variability of the Solar Corona

## 2.1 Introduction

As Rosner et al. (1978b) said: *"intensity fluctuations of coronal structures occur on virtually all observable spatial and temporal scales"*. Coronal variability spans relatively long timescale, from seconds (*flares*) to years (*solar cycle*). The building block of the solar corona, the coronal loops, are observed to be steady for long times, longer than the plasma cooling times (Rosner et al., 1978b). Therefore, they need some heating mechanisms that can heat them throughout this time, and bring them to an equilibrium condition. These mechanisms could be stationary and held for all the loop's lifetime or could be impulsive with rapid rate, shorter than typical plasma cooling times. The investigation of solar corona variability is so of great importance to obtain more insight into the coronal heating problem (Sec.1.3). The emission of coronal loops varies on different time scales, so the temporal analysis of coronal data is useful to obtain information that can characterize both the dynamics and the heating mechanisms of the solar corona. However these variations are not trivial

to interpret. Since the emission of coronal plasma is more sensitive to density than to temperature, variations are not direct signatures of heating events.

Imaging instruments are more appropriate to steady variability, because of their low exposure times which lead to high data cadence. An important issue is the bandwidth of observations. Looking with different kinds of instruments, that look in different pass-bands, we can observe events of different time scales and maybe due to different heating mechanisms. The imaging EUV-instruments, with normal incidence optics, have very narrow bandwidths (*i.e.* TRACE). So they can see rapid temperature variations of plasma that, heating or cooling, crosses very rapidly the band of sensitivity. Imaging X-Ray telescopes (*i.e.* Yohkoh/SXT, HINODE/XRT), in general detect emission from hotter plasma, and so in practice are more appropiate for heating diagnostics but, their bandwidth is larger and so they cannot take best advantage of this property. The spectrometers, instead, are able to detect temperature variations very well because they observe single lines, but their low time cadence allows us then to follow variations only on large time scales.

Time variability studies can be classified to address two main classes of phenomena: slow variability of steady structures and single rapid events as flare-like events (Reale, 2010). Here we address the latter issue which has received a strong push by high quality data from recent solar missions (Sec.1.4).

### 2.1.1 The Approach

The investigation of the heating mechanisms of the confined coronal plasma is still under intense debate. It is widely believed that the energy source for coronal heating is the magnetic energy stored in the solar corona, but an unsolved problem is how this magnetic energy could be converted into thermal energy of the confined coronal plasma.

As Parker (1988) proposed, rapid pulses called *nanoflares* may be the best can-

didate mechanism of magnetic energy release. Nowadays it is generally agreed that these small impulsive energy bursts are responsible for at least some of the Sun's hot corona, but whether they are the explanation for most of the multi-million degree plasma has been a matter of ongoing debate. A challenging problem is to obtain in the solar corona evidence that such nanoflares are really at work.

We can imagine a coronal loop as consisting of multitude of thin strands. A magnetic strand that is heated by a nanoflare evolves in a well defined manner. Its light curve has a characteristic shape (Reale, 2007). The intensity rises quickly as the nanoflare occurs, levels off temporarily, then enters a longer period of exponential decay as the plasma cools. If we could isolate individual strands in real observations, it would be easy to establish whether the heating is impulsive or steady. Unfortunately, this is not the case. The corona is optically thin, so each line of sight represents an integration through a large number overlapping translucent strands (see Fig.2.1), nonetheless, it may be possible to infer the presence of nanoflares.

Actual light curves exhibit both long and short-term temporal variations. Inside the short-term fluctuations, due to photon statistical noise we can search, with indirect methods, for impulsive events (nanoflares), that could account for the coronal heating (Sec.1.3.3).

Observationally X-ray and EUV transient brightenings have been discovered and extensively studied with different X-ray instruments on-board on different satellites (*Yohkoh*/SXT, SOHO, TRACE). Drake (1971) made an early study of the distribution of soft X-ray burst and pointed out that the frequency distribution of the transient brightenings is a single power law function of the energy:

$$\frac{dN}{dW} \sim AW^{-\alpha} \tag{2.1}$$

with $N$ rate of flares, $A$ normalization factor, that depends on the solar activity level (function of time), $W$ energy and with $\alpha \sim 1.8$.

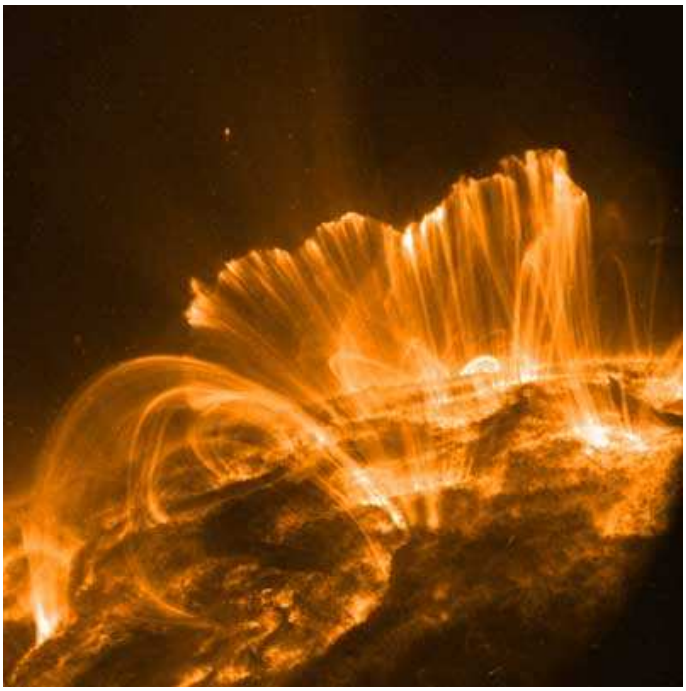

Figure 2.1 A TRACE (*Transition Region And Coronal Explorer*) image, with a portion of solar corona including a system of coronal loops (9 November 2000, 2 UT). Bundles of strands that overlap along the line of sight are clearly visible.

If the index is greater than 2, the smaller flares are dominant events (Hudson, 1991), and if the power law goes below the observational limit these small impulsive events could account for the entire coronal heating. For instance Shimizu (1995) found power law index for solar flares between $1.5 - 1.6$ for the range of energy $10^{25} - 10^{29}$ ergs for *Yohkoh*/SXT, while 1.8 for the range $10^{24} - 10^{26}$ ergs for TRACE.

A correlation between the magnitude of the time variability and the intensity of the persistent corona was found, in the sense that events with larger intensity happens more frequently in regions where the background emission is higher (Shimizu & Tsuneta, 1997). This means that the time variability is connected with the heating mechanisms of the persistent corona. So it is of fundamental importance to detect small (but systematic) events to obtain more insight into the nanoflares scenario.

Katsukawa & Tsuneta (2001) believed that if the X-ray intensity of the persistent corona is due to the superposition of small impulsive events, it cannot be constant but it is expected to fluctuate around the mean (or linear) intensity $I_0$, in a way that depends on the individual energy of the events itself. The fluctuation magnitude is larger as the energy of individual nanoflares increase with decreasing number of events. To quantitatively characterize these fluctuations simple histograms of the X-ray intensity fluctuation were created, these could give us information about nanoflares and coronal heating. They use multiple observing sequences of the YohkohSXT partial-frame images taken from 1992 April 29 to May 2, (Active Region 7150). The images were taken about every 100 s, in two different SXT passbands, and each observing sequence lasted 40 minutes.

Katsukawa & Tsuneta (2001) and Katsukawa (2003) showed that the amplitude of the fluctuations seems to be larger than expected from noise alone for SXT observations, and that the fluctuations excesses were larger for pixels with more intense emission. They found histograms that consists of two parts, a central gaussian-like profile, due to random fluctuation around the mean value $I_0$, and a wing component that they accounts for the transient brightening or gradual deviation.

Sakamoto et al. (2008, 2009) and Vekstein (2009) found in TRACE images much larger fluctuations than the photon noise for the brighter pixels, and they assumed that this excess of fluctuations was due to impulsive events below the noise level. However, this is difficult to determine with confidence, because the precise level of noise depends on the temperature of the plasma, and this is known only approximately in these studies. In fact, the level of noise depends on the incident photon counts, that can be evaluated with a conversion (Narukage et al., 2011) from measured Data Numbers (DN):

$$\sigma_{DN}(x,y,t) = \sqrt{K_i^2[T(x,y,t)]\ I_0(x,y,t)} \tag{2.2}$$

where $K_i^2$ is temperaure sensitive conversion factor, and $I_0(x, y, t)$ the measured intensity in DN. So we have to assume a temperature for the active region, and this value is only a rough guess for these data.

The existence of these small heating episodes is therefore a central issue for the investigation of the coronal heating, but they are elusive (see section 1.5).

The basic idea of this work is that if the solar corona is heated by nanoflares, they may leave some kind of signature on the light curves. As we have seen many authors (Shimizu & Tsuneta, 1997; Vekstein & Katsukawa, 2000; Katsukawa & Tsuneta, 2001; Katsukawa, 2003; Sakamoto et al., 2008) pointed out that a detailed analysis of intensity fluctuations of the coronal X-ray emission could provide us information about these smallest flares. Following this hint we searched, with statistical analysis, for small but systematic variability in high cadence light curves. We tackle this problem with the temporal analysis of imaging data from the X-Ray Telescope on-board the Hinode mission.

The high cadence allows us to separate the effects of noise fluctuations from the presence of true physical trends. We expect that the latter ones evolve in different, longer time scales, but might be very small and difficult to detect in a noisy background.

## 2.2 Temporal Analysis

### 2.2.1 The observation (AR10923)

**Active Region 10923** (hereafter AR10923) was observed on 14 November 2006 while it was located close to the Sun center (Fig.2.2). Other multi-filter observations of the same active region were extensively analyzed in the past for different purposes. Reale et al. (2007) used this active region observed in 12 November 2006 in different filter (Al_poly, C_poly, Be_thin, Be_med and Al_med) to determine the temperature distribution. They used ratios of appropriate products of filters (*combined filters ratio*) to optimize the signal-to-noise ratio, revealing a highly thermal structured corona. The fine structure of the loops was determined down to the maximum instrument resolution. Reale et al. (2009) searched for steady widespread hot plasma to infer the presence of nanoflares. They derived temperature and Emission Measure maps for all filter ratios that show evidence of a minor but significant component of hot plasma up to $\log T > 7$. Moreover they found a clear correlation between regions detected as hot in the soft filter ratio and regions detected as cool in the hard filter ratios and vice-versa (i.e. an anti-correlation). They performed Monte Carlo simulations with a variety of EM distributions along the line of sight. Since in the November 12 the south-west part of the active region was the location of several flares, Parenti et al. (2010) investigated the temporal evolution of one of the flares in, with particular interest in loops morphology, temperature and EM distributions. They compared this observation with another one, of the same active region, made by TRACE. They connected the temporal evolution and flaring of the active region with a rapid morphology change on TRACE data, in particular of the shorter loop system involved in the flare. These changes consisted in the relaxation of a tangled magnetic configuration. This result is consistent with the diffuse idea that the energy released by a flare phenomena comes from the relaxation of a tangled

magnetic configuration (*magnetic reconnection*).

The XRT image (Fig.2.3) shows the typical morphology of an active region, with dense arcades of coronal loops surrounding radially the central sunspot. The length of the bright loops ranges approximately between $4 \times 10^9$ cm (southern region) and $10^{10}$ cm. The image clearly shows a high degree of loop substructuring and most loops intersect along the line of sight.

AR10923 shows moreover several interesting features. A main toroidal loop

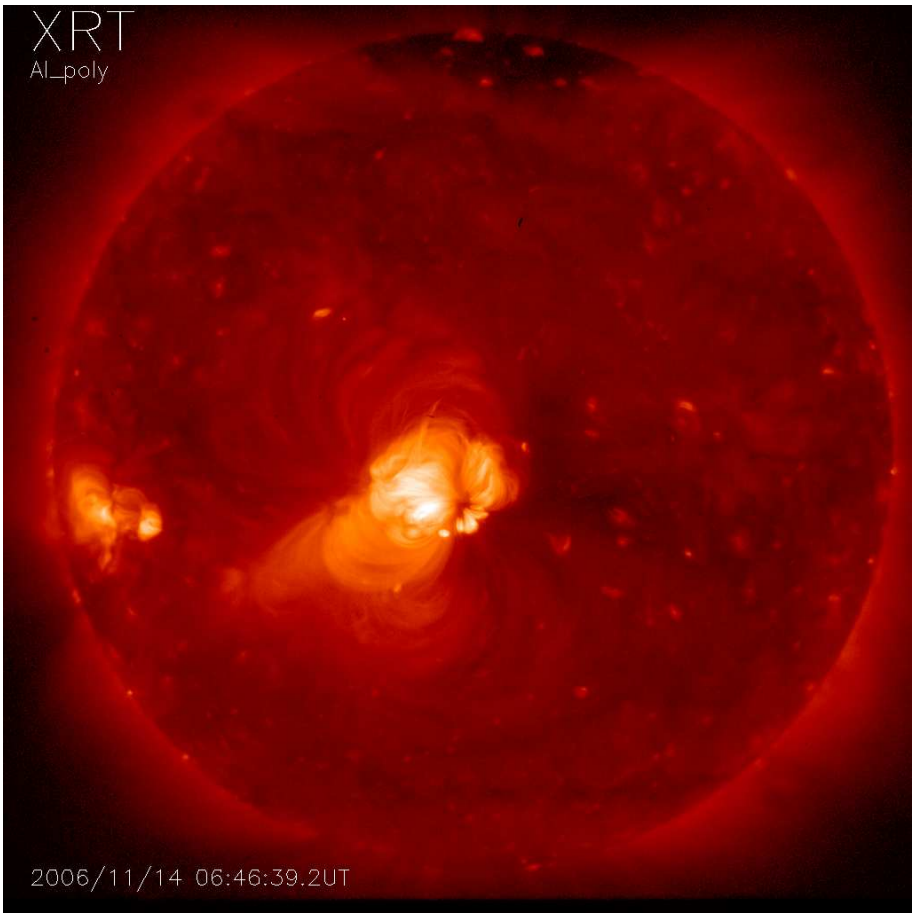


Figure 2.2 Synoptic image (2048×2048 pixels) of *X-Ray Telescope*, on board on the Hinode satellite, taken on 14 november 2006 at 6:46:39UT, in the Al_poly filter band. The active region under analysis (AR10923) is clearly visible located close to the disk center.

arcade ($\sim$ 100 arcsec wide), surroundings the central magnetic black pole, opens to the south part; there are large-scale loop structures (up to $\sim$ 350 km long) in the north and southwest regions; a bright nutshell-shape loop system in the south of the magnetic pole; and an upside-down V-like loop system on the right side of the bright nutshell (Fig.2.3). The central loop system is the brightest of the entire active region. Besides the XRT observed active region shows a very high degree of substructuring, with tens of loop and structures filed but also overlapping along the line of sight.

We analized a part of the active region AR10923 enclosed in a smaller field of view of 256×256 arcsec$^2$ (Fig.2.4, all panels). The observation sequence starts at 11UT and consists of 303 images taken in the Al_poly filterband (see Sec.1.4.1) with an exposure time of $\sim$ 0.25 s and an average cadence of $\sim$ 6 s (between 3 and 9 s), for a total time coverage of $\sim$ 40 min. During the observation time no major flare and no significant rearrangement of the region morphology occurred. We used the 2009/2010 release of the standard XRT software (*SolarSoftWare*) to perform calibration, including corrections for the read-out signal, flat-field, CCD bias, dark image subtraction. The observation images were co-aligned using the jitter information.

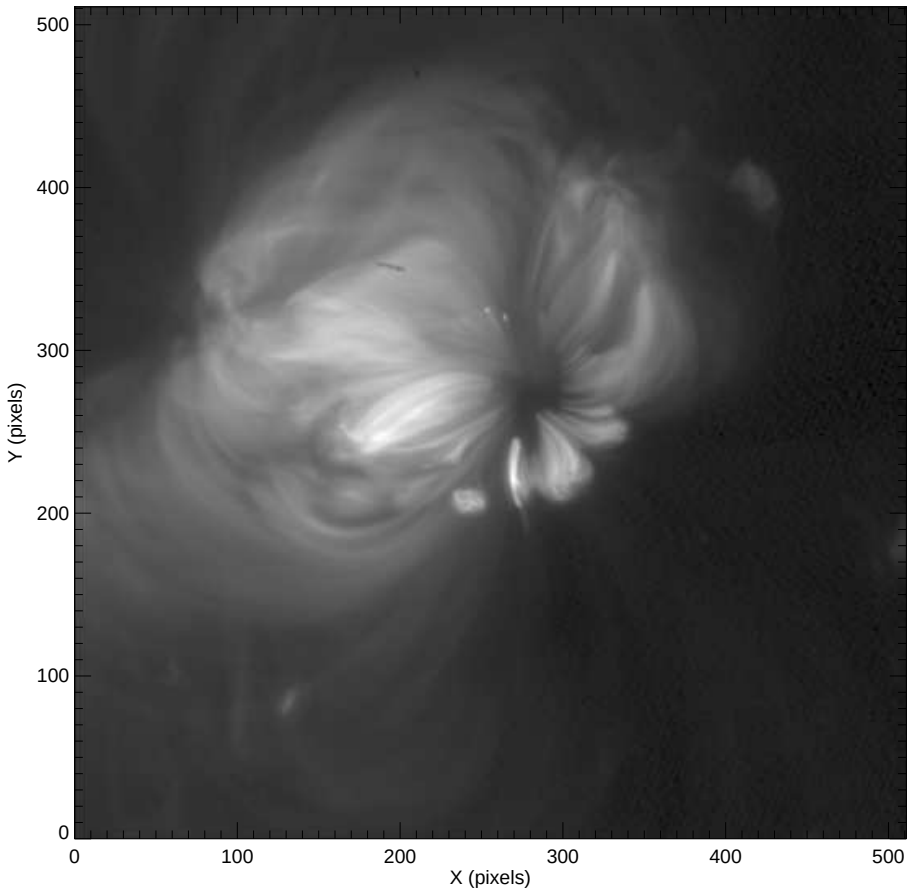


Figure 2.3 A 512×512 pixels particular of the sun disk (Fig.2.2), in the field of view the active region under analysis.

### 2.2.2 The Data Cleaning

We looked for possible small but systematic variations inside the fluctuations of X-ray emission. Then we had to remove any other effect that could confuses the effects that we are attempting to study. Before starting the analysis we did an accurate screening of the data that we list in the following:

- Low signal pixels remotion

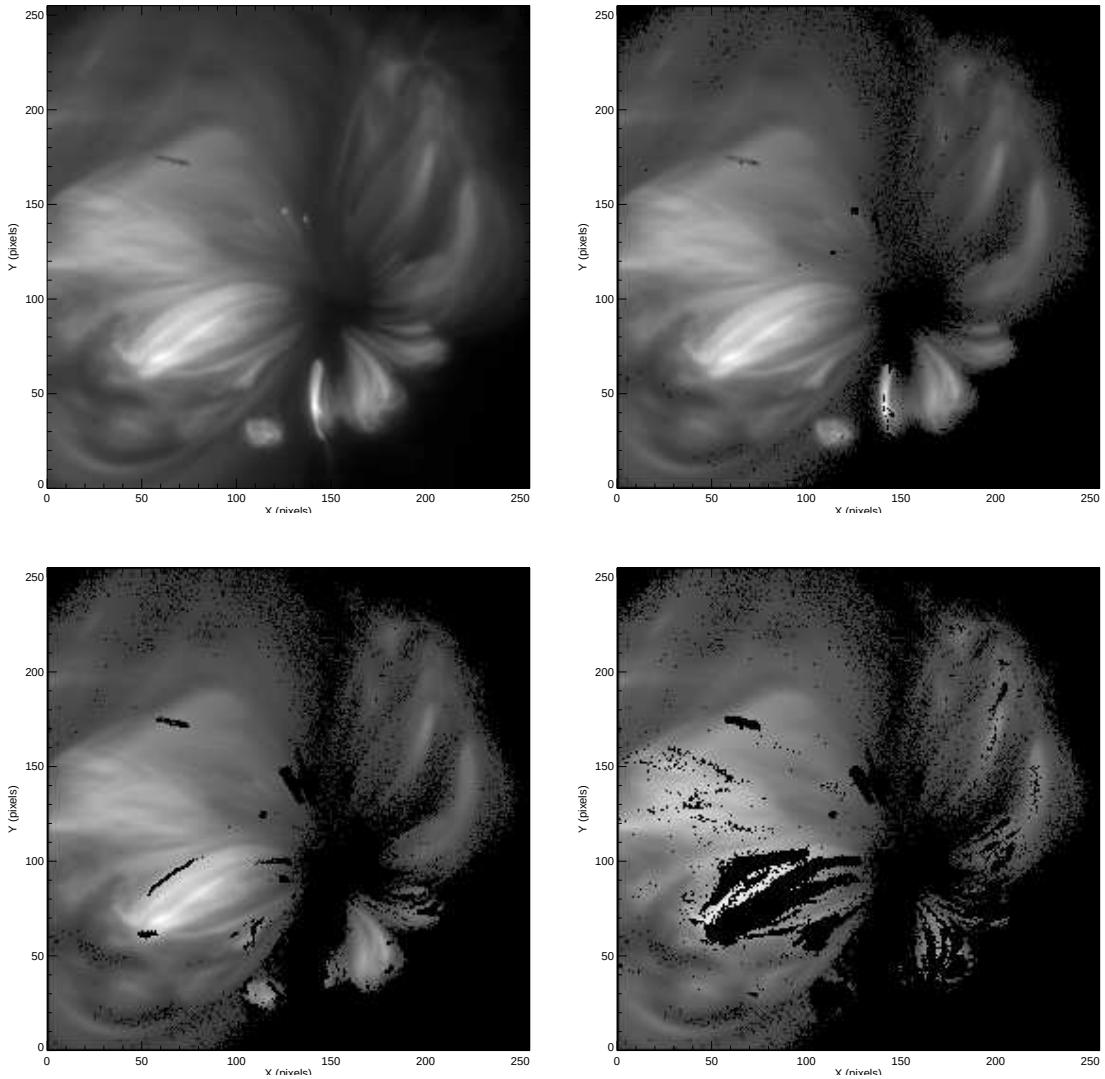


Figure 2.4 Summary of the images of the active region after removal of: the pixels with low signal (top left panel); the pixels with spike-like events (top right panel); the pixels involving microflares (bottom left panel); the pixels involving slow variations like loop drifts or loop motion (bottom right panel). We applied our analysis to all the remaining pixels.

and transient brightenings remotion:

- Spike-like features
- Microflares and brighter transient events

- Slow variations (*Loop motion effect*)

### Low Signal Remotion

Since fluctuations due to episodic heating are erratic and of very small amplitude, they are very difficult to detect among ever-present noise. To avoid pixels with low count statistics, we removed all pixels with average count rate below 30 DN/s, so we removed the *"quiet sun"* from the region under analysis (Fig.2.4, top left panel). We choose this threshold value to remove pixels with error greater then 50% of the photon count value. This is a threshold value that ensures to include pixels with good count statistics. This threshold value removes $\sim 11\%$ of the total pixels.

### Spike Like Features

Instruments and detectors on-board on satellites that work out of the earth atmosphere, could be hit by energetic ($10^9 - 10^{20}$ eV) particles (protons, hydrogen nuclei, helium nuclei, alpha particles, nuclei of heavier elements or electrons). In our data cleaning operations, we preliminary removed pixels affect by rapid and isolated variations maybe due to collisions with these particles (called *cosmic rays*). To avoid pixels affected by these spikes (very focused in space and time), we removed, from the data cube, those pixels that shown intensity value greater than 1.5 times the spatial median of the immediately surrounding pixels. The 1.5 value is the best compromise, because with lower threshold value we could remove pixel with statistical variation ($\sim 3\,\sigma$); with greater values we could instead accept, for the analysis, pixels affected by cosmic ray with lower energy, that not differs much with respect to the energy of active region pixels with more intense signal (Sakamoto et al., 2009). In Figure 2.5 we report, as an example, the light curve of a single pixel of the active region removed because of a spike. With this screening we remove $\sim 15\%$ of pixels (Fig.2.4, top right panel).

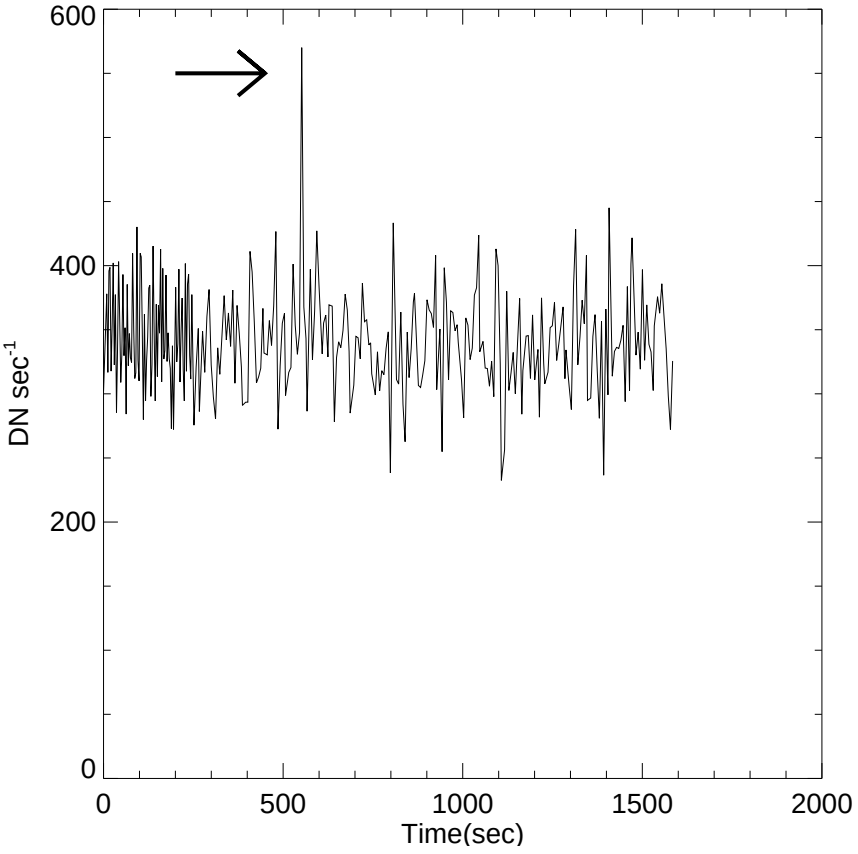


Figure 2.5 Single pixel light curve, removed because of a cosmic ray spike.

### Microflares events

An effective problem for our purposes is that the active region is a scenery of continuous macroscopic events, which may affect our search for small amplitude fluctuations (Lin et al., 1984). Light curves can be affected by different kind of large scale impulsive events such as *microflares* (Kano et al., 2010), that was out of interest for subsequent analysis. To exclude these large scale events we removed pixels where the intensity becomes 1.5 times brighter than the linear fit of the pixel light curve (Fig.2.6). The microflares-affected pixels are $\sim$ 10 % of total (Fig.2.4, bottom left panel).

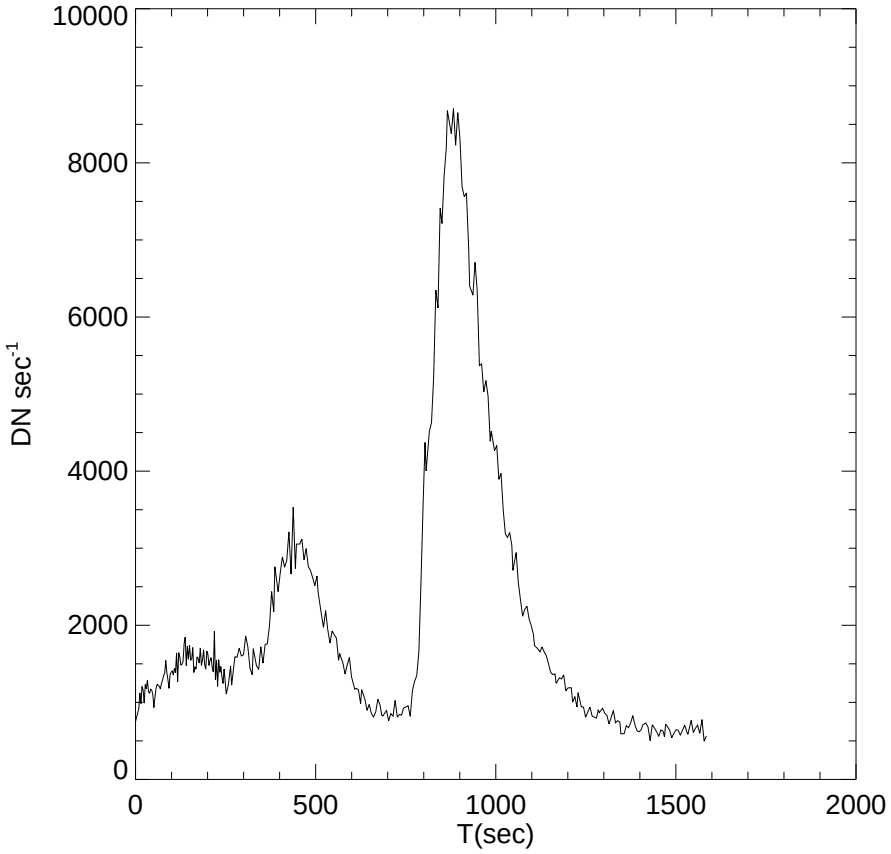


Figure 2.6 Single pixel light curve with a microflare event, i.e. pixels where the intensity becomes 1.5 times brighter than the linear fit to the pixel light curve (dash-dot line).

### Loop Motion effect

Throughout the observation time, we might see intensity variations simply due to the displacement or drift of coronal structures along the line of sight. We have to remove also this effect. We used a methodology developed by Sakamoto et al. (2009), which counts how many times an intensity light curve crosses the linear fit line. If the fluctuation of $m$ data point around the linear fit is completely randomic, the time profile has $m-1$ possibilities to cross the linear fit, with 0.5 probability. The *number of crossing* follows *Binomial* distribution with $\frac{(m-1)}{2}$ mean, and $\frac{\sqrt{m-1}}{2}$

standard deviation. We assumed that the duration of intrinsic intensity fluctuation is shorter than the observing time ($\sim$ 40 min), and the duration of fluctuation due to loop drift or motion is comparable with observing time. In these conditions the number of crossing due to loop motion should be smaller than $\sqrt{(m-1)}/2$. Slow variations are excluded by removing all pixels where the light curves have a "*number-of-crossing*" lower than the mean of binomial distribution ($\sim$ 7% of pixel), (Fig.2.4, bottom right panel). We show in the Figure 2.7 a removed pixel with *number-of-crossing* with regard to the linear fit ($m = 13$) much lower than the mean of binomial distribution ($151 \pm 8$).

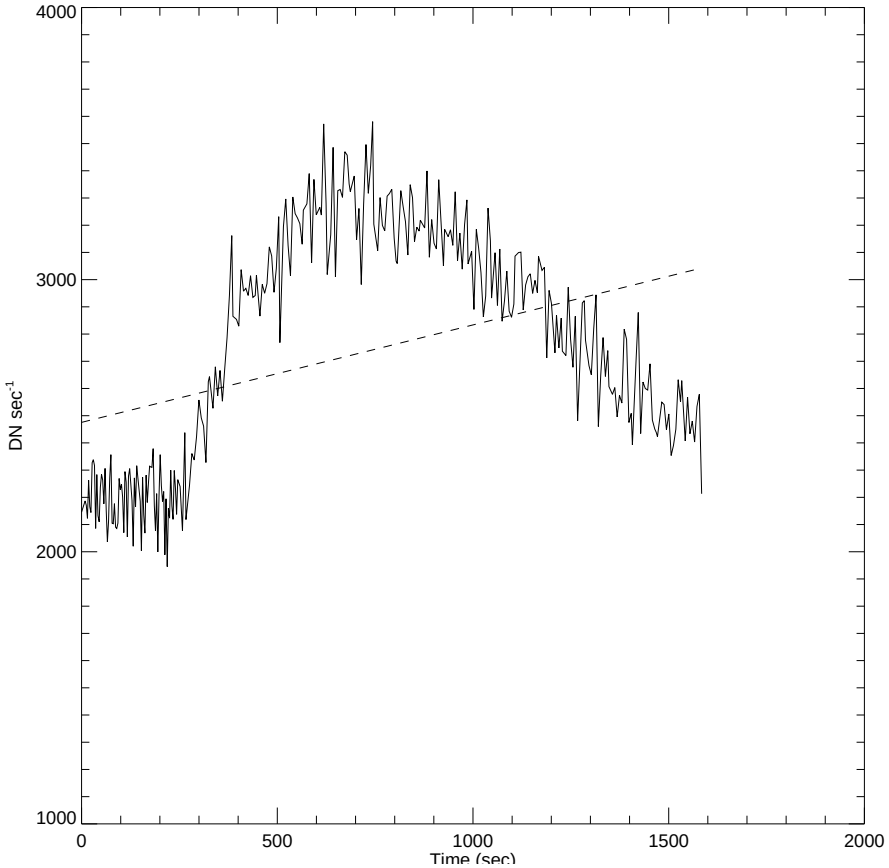


Figure 2.7 Light curve of a pixel probably affect by *loop motion effect*, due to local loop drift or loop motion. The dashed straight line is the linear fit with regard to we count the *number of crossing*. In the $x$-axis time values are reported in seconds; in the $y$-axis units are DN $\sec^{-1}$.

## 2.3 The Analysis and Results

### 2.3.1 Instrument Calibration

XRT has nine filters with different temperature response, and with a moderate capability of diagnosing temperatures of the coronal plasma (i.e. it makes temperature maps) from 1 MK to 10 MK and more, through filter ratios. To take advantage of this capability an accurate calibration of the temperature response of XRT is of

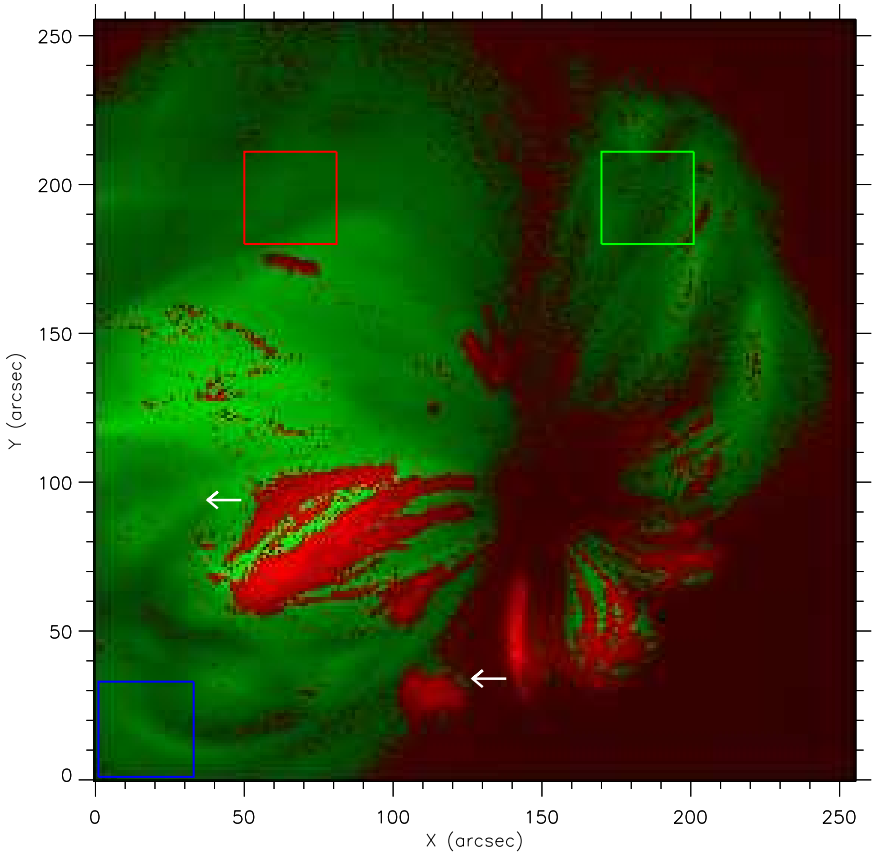


Figure 2.8 Active region AR 10923 observed with the Hinode/XRT Al_poly filter on 14 November 2006 at 11 UT. We distinguish between pixels accepted (green) and rejected (red) for the analysis. The color scales are powers of the intensity (0.5 and 0.1 for green and red respectively), with maxima of 57 DN/s and 1171 DN/s respectively. We mark three subregions (frames) which are analyzed specifically (Sec.2.3.5). We will show in the following the light curves of the two pixels indicated by the arrows.

great importance (Collura et al., 1994; Cosmo et al., 2005). But after the launch (during 142 days from 8 September 2007 to 28 January 2008) the X-ray intensity, of the *Quiet sun*, observed with XRT continuously decreased in the Al_mesh, Al_poly, C_poly, and Ti_poly filters to $\sim 27\%$, $\sim 59\%$, $\sim 80\%$, $\sim 73\%$ respectively. This was due probably to the accumulation of material (named *contaminant*) that could affect the optical path of XRT. The on-orbit calibration work was done by Narukage et al. (2011) during 2009-2011, taking into account this effect of on-orbit contamination. Fortunately the data set analyzed in this work (2006/11/14 - AR10923) was not strongly affected by contaminants because taken early in the mission. Anyway our approach allows us to minimize any calibration problem (Sec. 2.3.4).

### 2.3.2 Pixels Light Curves

At the end of the screening we are left with almost 56% of the total number of pixels (green pixels in Fig.2.8). We were at this point in the condition to analyze the data.

#### Physical Constraints

Our data cadence is below 10 s. If we observe pixel fluctuations from one frame to the other, we wonder whether we can expect plasma physical processes, e.g. heating or cooling, on this timescale. A fluctuation from high to low intensity should imply plasma cooling which is ruled by the strand cooling timescale (Reale, 2010):

$$\tau_s = 500 \, \frac{L_9}{\sqrt{T_{0,6}}} \tag{2.3}$$

with $L_9$ the loop length in unit of $10^9$ cm and $T_{0,6}$ the loop temperature in unit of $10^6$ K. In the conservative assumption of a (high) starting temperature of $\leq 10$ MK, we obtain that the strand length should be $2L \leq 10^8$ cm. Active region loops are far longer than this value, and therefore plasma confined in them simply cannot cool

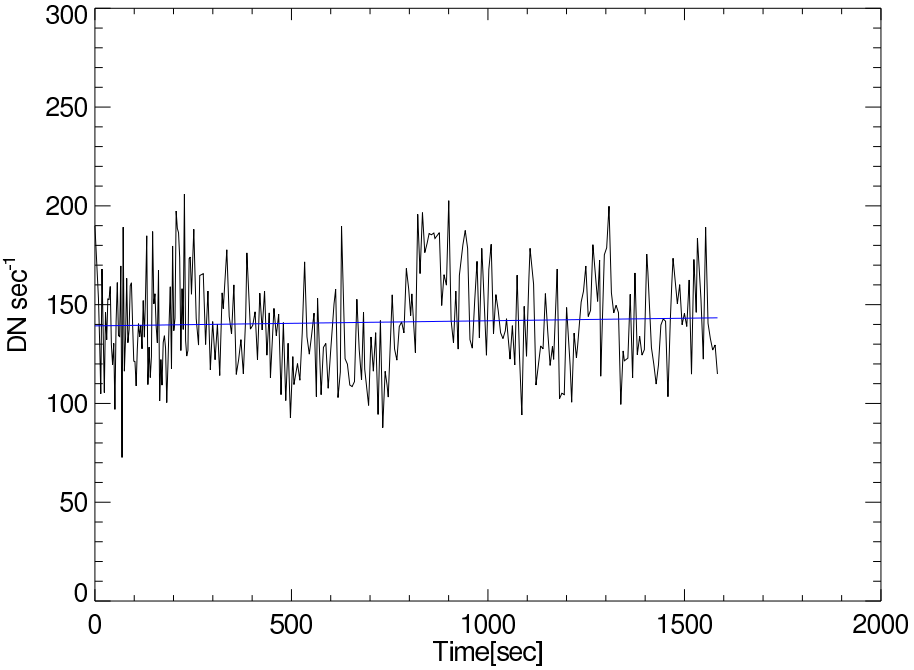


Figure 2.9 Light curve of a valid single pixel (black line), with linear fit (straight blue line).

on such short timescale. We can exclude that the fluctuations observed in our high cadence observations might be due to physical processes other than pure photon noise.

### Data Analysis

Next step was to measure the X-ray intensity variations, during observation time, with respect to specific temporal trend. Since we removed any kind of slow or fast fluctuation over the noise level, we can expect that the X-ray light curves have a linear trend with random noise added on (see Fig.2.9). We checked that the light curves of the remaining pixels can be fit satisfactorily well with a linear regression. The slopes tend to be very close to zero, even though this median is slighly positive, showing a small preference for increasing intensity (Sec.2.3.6). We then measure the amplitude of the fluctuations of the count rate in each pixel with respect to the

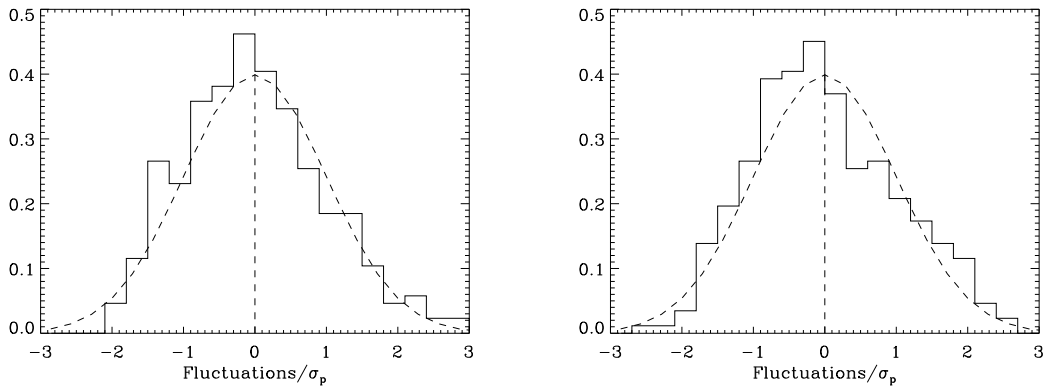


Figure 2.10 Distributions of the intensity fluctuations with respect to the linear fit to the light curves, in two selected pixels (highlighted by the arrows in Figure 2.8) . The distributions are normalized to the nominal Poisson noise. A Gaussian centered on zero and unit width is plotted for reference (dashed line).

linear fit to the light curve. The Fig.2.9 shows as example a single pixel light curve, with the linear fit in blue. We measure intensity fluctuations relative to the linear fit as to:

$$dI(x,y,t) = \frac{I(x,y,t) - I_0(x,y,t)}{\sigma_P(x,y,t)} \tag{2.4}$$

where $I(x,y,t)$ is the count rate (DN/s) at position $[x,y]$ and time $t$, $I_0(x,y,t)$ is the value of the linear fit at the same position and time, and $\sigma_P(x,y,t)$ is the photon noise value. Here the $\sigma_P(x,y,t)$ is obtained as the width of the distribution of the intensity fluctuations (*standard deviation*). To quantitatively characterize the fluctuations and possible small hidden trends we built simple histograms of the intensity fluctuations of the X-ray emission for the active region. We show as example in Figure 2.10 the distributions of the fluctuations of the light curves in two selected pixels. The distributions are normalized to the Poisson noise. A Gaussian-shape curve centered on zero and with unit width is also shown for reference (dashed line) in the same plots (Fig.2.10, both panels).

The distribution of the intensity fluctuations is not symmetric at either pixel. There is a slight excess of negative fluctuations (fainter than average emission) compared to positive, i.e. there are more negative fluctuations (corresponding to reduced intensity) than positive. This excess makes the histogram slightly asymmetric toward the left side of the distribution (Fig.2.10, both panels).

A good measure of the asymmetry is the difference between the median and mean values. The mean fluctuation is 0, by definition, the median fluctuation is $-0.03 \pm 0.07$ in the brighter pixel and $-0.07 \pm 0.08$ in the fainter pixel. The uncertainties in the median values have been rigorously computed according to (Hong et al., 2004) (Sec.2.3.3). As we can see at this point the median is negative but not significant, because is almost in the $\sigma_P$ range. To improve the significance of this result we need to sum up over a larger number of pixels, so in the subsequent analysis, we selected sub-regions and besides we sum up over the entire active region (Sec.2.3.5).

### 2.3.3 Error and Quantiles Analysis

The uncertainties in the median values have been rigorously computed according to the quantile error analysis (Hong et al., 2004). This quantile error estimation uses the Maritz & Jarrett (1978) method. The method rely on $L$ estimators (linear sum of order statistics) using beta function. $N$ is the number of the analyzed elements $E_i$ (fluctuations in our case), $x$ is is the order of *quantile fraction* (0.5 for the median).

$$M = Nx + 0.5, \qquad a = M - 1, \qquad b = N - M. \tag{2.5}$$

We then define $W_i$ using the incomplete *beta function* $B$,

$$W_i = B(a, b, y_{i+1}) - B(a, b, y_i) \tag{2.6}$$

$$B(a,b,y) = \frac{\Gamma(a+b)}{\Gamma(a)\Gamma(b)} \int_0^y t^{a-1}(1-t)^{b-1} dt \tag{2.7}$$

where $y_i/N$ and $\Gamma(n+1) = n!$ (the gamma function). Using $W_i$ and $E_i$, we calculate the $L$ estimators $C_k$,

$$C_k = \sum_{i=1}^{N} W_i E_i^k \tag{2.8}$$

and then

$$\sigma(E_{x\%}) = \sqrt{C_2 - C_1^2} \tag{2.9}$$

is the value of the error over the mean of the median distribution.

### 2.3.4 Photon noise

To improve the significance of our results (improving the signal to noise ratio) and to check whether this effect is unfrequent or spread throughout the entire region, we build the distribution of the intensity fluctuations on areas larger than a single pixel. To do this we have to normalize the fluctuations so that we can sum them homogeneously. We normalize each of them to the respective average noise amplitude.

In general, since the photon noise follows a Poisson distribution, the standard deviation of $dN$ ($d\sigma$) could have been derived as the square root of the photon counts as (Kano & Tsuneta, 1995; Katsukawa & Tsuneta, 2001; Narukage et al., 2011):

$$d\sigma = \sqrt{dN} \tag{2.10}$$

and since the electron counts (DN) can be connected to the photon counts by

$$DN = \int \left( \frac{hc}{\lambda} \times \frac{1}{e \times 3.65 \times G} \right) \, dN \tag{2.11}$$

where $h$, $c$, $e$, and $G$ are respectively the Planck's constant, the speed of light, the elementary electric charge, and the system gain of the CCD camera, which is 57.5 [electron $DN^{-1}$] for XRT (Kano et al., 2008). We can derive the error of DN [$\sigma_{DN}$] as

$$\sigma_{DN} = \sqrt{\int \left( \frac{hc}{\lambda} \times \frac{1}{e \times 3.65 \times G} \right)^2 \, (d\sigma)^2} \; = \; \sqrt{K_i^{(2)}(T) DN} \tag{2.12}$$

where $K_i^{(2)}$ (hereafter $K_i[T(x,y,t)]$) is a conversion factor from DN to photon counts, which depends on the underlying spectrum and therefore on the temperature $T$ of the emitting plasma, in the part of detectable temperature range of XRT. We can rewrite the noise from the measured DN as:

$$\sigma_{DN}(x,y,t) = \sqrt{K_i[T(x,y,t)] \; I_0(x,y,t)} \tag{2.13}$$

where $I_0$ is the measured DN, and $\sigma_{DN}$ is already in units of DN.

In order to estimate $\sigma_{DN}$ (eq.2.13) we need a guess on the spectrum and tempearature $T$, which we do not know.

Our work started and developed in the period of maximum uncertanty about the HINODE/XRT filters calibration due to the discover of calibration problems (contaminants inside the instrument, sec.2.3.1). With the aim to by-pass these problems (before the last release of calibration, Narukage et al., 2011) and to make the whole analysis as self-consistent as possible, we choose to estimate the photon noise by measuring it directly as the standard deviation of the fluctuations with respect to the best-fit line. The output is a single value $\sigma_{DN}(x,y)$ for each pixel, in the assumption that the DN rate and so the temperature do not change significantly

during the observation.

### 2.3.5 Region Analysis

Figure 2.11 (left panel) shows results for the three sub-regions marked in Fig.2.8 and for the whole active region. Subtle asymmetries can be detected by eye when compared to the Gaussian distribution shown as a dashed curve for comparison. The right panel in Fig.2.11 shows the distributions of the median values themselves, computed individually at each pixel.

Table 2.1 shows the values of the *mean of medians* of the fluctuations for the entire (allowed) active region (green pixels in Fig.2.8) and for the three selected sub-regions (squares in Fig.2.8). The analysis of the whole region (section 2.3.2) was made considering pixels above three different threshold intensity values (30, 800, 1600 DN $\sec^{-1}$). These values are selected to sweep almost all the intensity range of the active region after the pixel removal ($30 - 3800$ DN $\sec^{-1}$), choosing sub-ranges with enough pixels ($< 1600$ DN $\sec^{-1}$) and that differ from one another, significantly, in intensity level ($\geq 500$ DN $\sec^{-1}$). This operation with the aim to check whether the effects of median shift could appear or disappear with different intensity levels.

Each column of Table 2.1 shows the results for each intensity threshold. As we can see in the Table, there is a clear preference for the medians to be negative. The peaks of the distributions (most likely values) are between $-0.025 \pm 0.002$ and $-0.030 \pm 0.002$ for the sub-regions and $-0.0258 \pm 0.0004$ for the active region as a whole. The estimate method of the uncertainties is reported in the previous section.

So the bias toward negative values id highly significant.

The assumption that all observed fluctuations come from photon statistics will over-estimate the actual photon noise. The standard deviation of the counts relative to the linear fit includes real variations in addition to the photon statistical fluc-

Table 2.1. Active Region Analysis results

| Data | Threshold 30 | Threshold 800 | Threshold 1600 |
|---|---|---|---|
| Region | -0.0258±0.0004 | -0.0160±0.0009 | -0.0136±0.0018 |
| Sub-reg 1 | -0.025±0.002 | ··· | ··· |
| Sub-reg 2 | -0.026±0.002 | ··· | ··· |
| Sub-reg 3 | -0.030±0.002 | ··· | ··· |

Note. — Table 2.1 shows the values of the median averages, with errors, for the entire active region, and for the selected subregions (Fig.2.8). The listed values for the entire active region are obtained analyzing only pixels with intensity over three different threshold values. The listed values including threshold values are in unit of DN $sec^{-1}$.

tuations. The derived value of $K_i(x, y)$ is therefore an upper limit: $K_i < \sigma^2_{DN}/I_0$. Since Poisson distributions have the property that they are more asymmetric for smaller mean values, the distribution used to generate the time series is therefore overly asymmetric. In our opinion this asymmetryies are signature of systematic trends in the intensity light curve hide in the photon noise. These signatures are also widespread over the entire region, suggesting that this possible systematic effect is also present and the physics cause of this works in the whole active region. Before to start with numerical simulations of different theoretical possible heating models, we made different kind of tests to disprove if this effect could be due to the particular analysis and chooses made during the screening and analysis work.

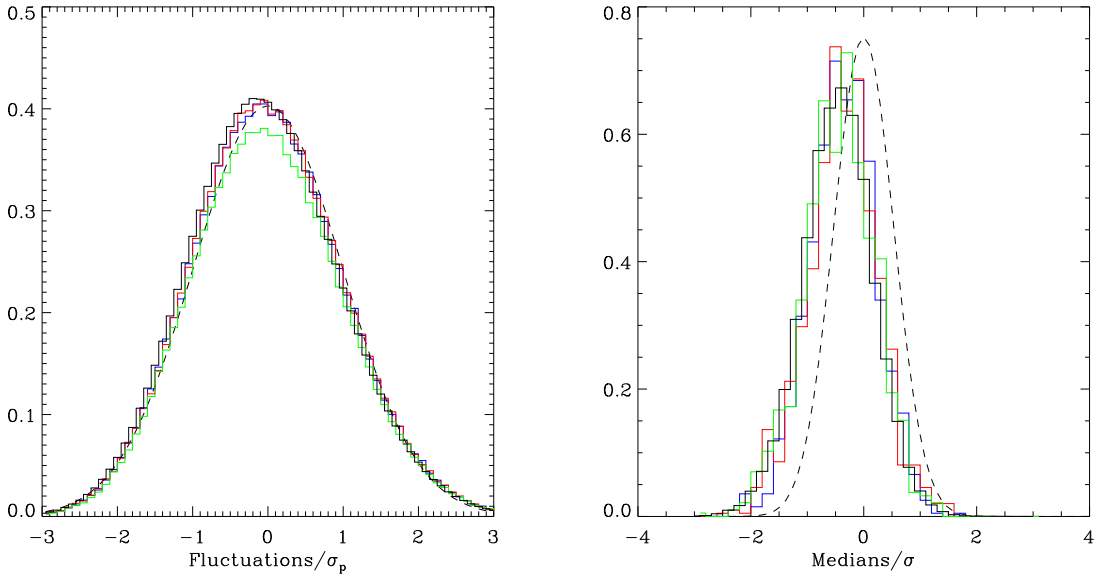


Figure 2.11 Statistical analysis of the fluctuations of the pixels light curves with respect to the linear fit in three selected regions (histograms with the same colors of boxes in Figure 2.8) and in the whole active region (black histogram). We show the distributions of the fluctuations normalized to the nominal Poisson noise and the distributions of the medians normalized to their standard deviation. A Gaussian centered on zero and unit width is plotted for reference (dashed line).

### 2.3.6 Tests

In this section we show a series of additional tests that we performed to verify if the result is robust, and to check whether the effect that we find is due to any kind of bias. As first step we checked for dependence on the fitting of the pixel light curve.

#### Best Fit Curve

Before the temporal analysis we searched for the best fit curve to analyze the light curve fluctuations. We have checked linear and quadratic fit. All the valid light curves are fitted satisfactorily with a linear regression, and the trends are generally constant or very slow, with small preference for increasing tendences (see Fig.2.12).

The distribution of slopes has an almost Gaussian shape, very peaked near zero value, with a little wing on the right side. The average time-scale for these trends is $\tau = (1/m) =\sim 625$ sec, with $m$ average angular coefficient, that for an observation of $\sim 2400$ sec, show a variation of 0.16%. The results do not change qualitatively considering only pixels with light curves compatible with a constant, i.e. the slope of the linear fitting is compatible with zero (32% of the total pixels). The results are confirmed with a median peak at $-0.0244 \pm 0.0006$.

The results do not change qualitatively using a quadratic fitting to the pixel light curves, instead of a linear fitting. If we sum up all the fluctuations normalized to the average Poisson noise over the whole region, we again obtain an asymmetric distribution, and the medians are asymmetrically distributed around zero.

### Skewness

The third moment about the mean is known as the *skewness* parameter. Here we considered this parameter as a measure of the degree of asymmetry of a distribution (tipically of a real-valued random variable):

$$S_k = \frac{\frac{1}{N}\sum_{j=0}^{N-1}(x_j - \overline{x})^3}{\sigma_{skew}^3} \tag{2.14}$$

with

$$\sigma_{skew} = \sqrt{\frac{1}{N}\sum_{j=0}^{N-1}(x_j - \overline{x})^2} \tag{2.15}$$

The skewness value of a distribution can be positive or negative. If the left tail of the distribution is longer than the right tail, the skewness of the distribution is said to be negative. If the right tail is, on the contrary, longer, than the distribution has positive skewness (Fig.2.13). If the two tails are equal, the distribution has zero skewness.

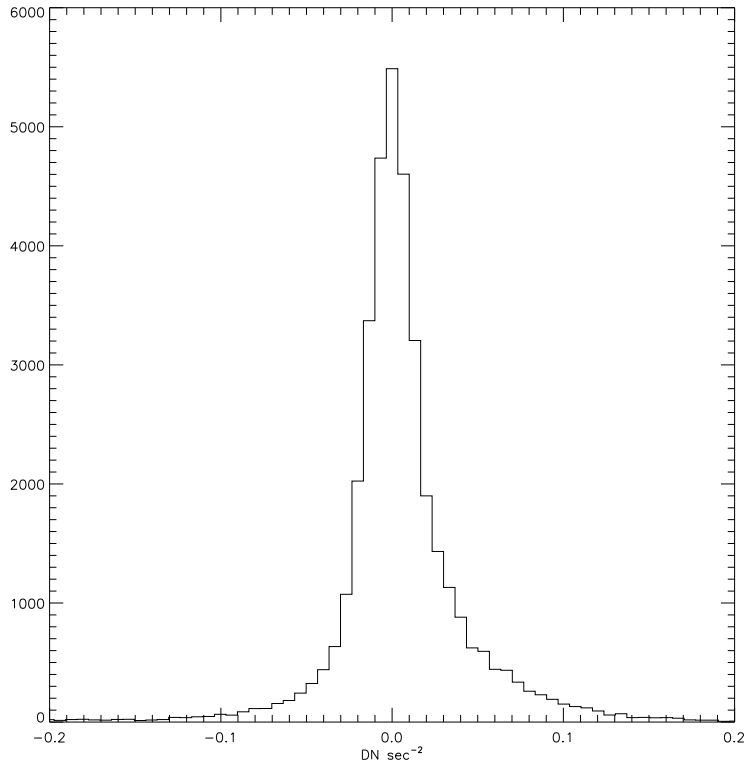


Figure 2.12 Distribution of the angular coefficients of the linear fitting of the pixels light curves.

The value obtained for the fluctuations distribution of the entire active region is $1.13 \pm 0.23$, positive value that account for an asymmetric distribution like Poissonian distribution i.e. with the right tail more pronounced than the left tail (e.g. the blue curve in the Figure 2.13). So the skewness value for the asymmetry of the distribution of intensity fluctuations confirms an asymmetric distribution in agreement with Poissonian distribution that shown also a negative median.

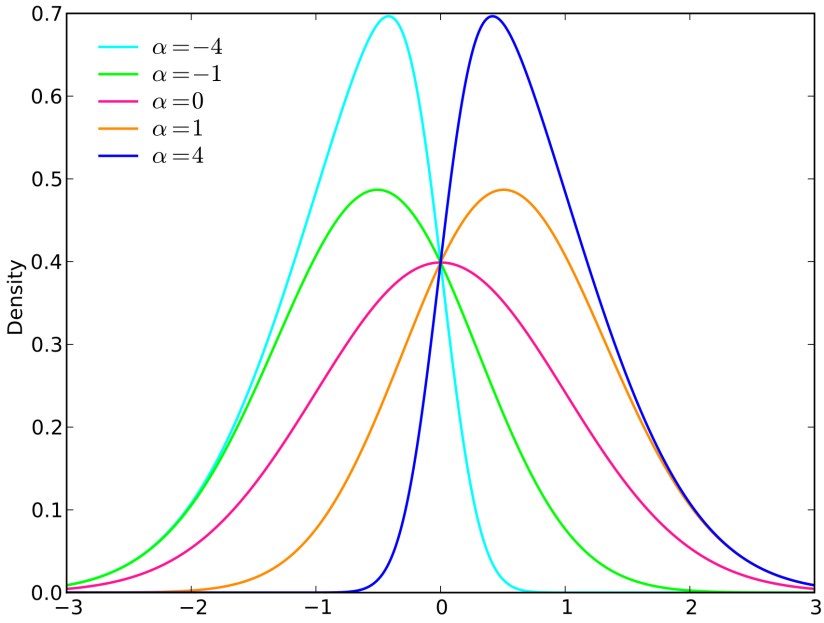


Figure 2.13 Only with the aim of example we show skewness values for a probability density function. Skewness is a measure of the degree of asymmetry of a distribution, if the left tail is more pronounced than the right tail, the function is said to have negative skewness. If the reverse is true, it has positive skewness. If the two are equal, it has zero skewness.

## 2.4 Modeling

Photon counting obeys Poisson statistics, and since the Poisson distribution is asymmetric, we expect that at least part of the negative offset of the median values is due to photon noise. We determine how much by performing Monte Carlo simulations to generate synthetic light curves for an appropriate number of pixels. As first step we devise an *"ad hoc"* model tailored to reproduce the observed evidence. In particular, we build pixel light curves, using a pre-determined basic pattern and adding the appropriate noise effect due to the discrete photon statistics.

### 2.4.1 The Monte Carlo Simulation

#### Null Hypothesis

As starting point, we consider the observed emission map, obtained by time averaging all the images. As null-hypothesis we assume the count rate in each pixel to be constant and equal to the average count rate, i.e. the light curve of each pixel to be flat.

We then randomize the pixel counts collected at each time according to Poisson statistics, with the same average fluctuation amplitude as the observed one, derived according to Equation 2.13. We obtain a noisy light curve, with fluctuations Poisson-distributed around the zero-value. We repeat this procedure for all valid pixels, therefore obtaining a data-cube of fake XRT images exactly equivalent to the real one. We can then apply the same analysis to the fake data. The result is that we obtain asymmetric distributions already from the null-hypothesis.

In the first row of Tab.2.3 we show the results obtained from the Monte Carlo simulations for the null-hypothesis, for the whole active region (first row, $A = 0$) and for the three threshold values (30, 800, 1600 DN sec$^{-1}$). The obtained result $-0.0164 \pm 0.0004$ ($\geq$ 30 DN sec$^{-1}$) has to be compared with $-0.0258 \pm 0.0004$ obtained from the data. Analogously we have computed that for all pixels with an average rate $\geq 800$ and $\geq 1600$ DN/s the median distribution for the whole region is $-0.0096 \pm 0.0009$ and $-0.0096 \pm 0.0017$, respectively. In the second row of Tab.2.4 we show the results obtained for the null-hypothesis (first row, $A = 0$), for the three subregions (only for the threshold 30 DN sec$^{-1}$), where we obtain median values between $-0.013 \pm 0.002$ and $-0.018 \pm 0.002$. All these values are incompatible with and significantly lower than those measured from the observational data ($-0.025/-0.030 \pm 0.002$).

Table 2.2. Monte Carlo Simulations Parameters

| $A$ [1] | $dt$ [2] | $\tau$ [2] | $Thr = 30$ [1] | Thr=800 | Thr=1600 |
|---|---|---|---|---|---|
| 0 | 0 | 0 | 30 | 800 | 1600 |
| 30 | 360 | 360 | 30 | 800 | 1600 |
| 30 | 540 | 360 | 30 | 800 | 1600 |
| 60 | 360 | 180 | 30 | 800 | 1600 |
| 60 [3] | 360 | 360 | 30 | 800 | 1600 |
| 60 | 360 | 540 | 30 | 800 | 1600 |
| 60 | 540 | 360 | 30 | 800 | 1600 |

Note. — Parameters of the Monte Carlo simulations of light curves with trains of decaying axponentials. The cadence ($dt$ [2]) is Poisson-distributed around the average value, the amplitude ($A$ [1]) is random-uniform between 0.5 and 1.5 the average value, A. A = 0 is the *null-hypothesis* (no perturbation).

[1]The amplitude height of exponentials and the threshold of intensity for the simulated pixels are in units of DN $s^{-1}$.

[2]The sampling spacing ($dt$) and the $e$-folding time ($\tau$) are in seconds.

[3]Simulation that best approaches the values measured in the observation.

### 2.4.2 Exponential Decay Hypothesis

Because we obtained, in our analysis, asymmetric distributions of fluctuations and a negative off-set of the medians distribution, we want to search for a possible lightcurve that could account for this kind of results. Among the possible curves, the exponential decay is an intrinsically asymmetric curve with negative median, and with physical reasonable significance (as example see sec.2.5). So the next step of our modeling was to perturb the constant parent light curve with a sequence of random segments of exponential decays, linked one to the other. We slightly reduce the constant offset so as to maintain the same average DN rate after adding the perturbations, which are all positive.

As shown in the top panel of Fig.2.14, the parameters of the perturbations are the $e$-folding time, the average time distance between two subsequent perturbations, and the amplitude. All the parameters values used in the Monte Carlo simulations

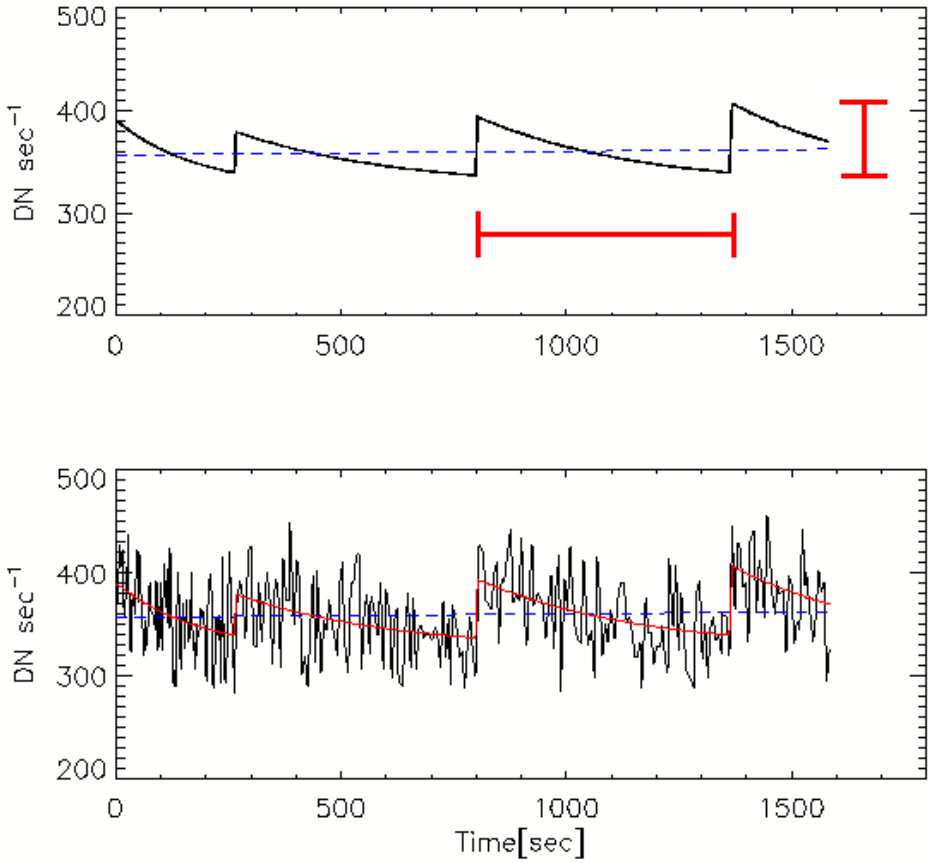


Figure 2.14 Top panel: Light curve of a single pixel obtained from Monte Carlo simulations made with trains of exponentials. In the figure are showed also in red two of the parameters of the simulation: the sample spacing ($dt$) between subsequent perturbations (horizontal red segment); and the amplitude ($A$) of the exponential pulse (vertical red segment). Bottom panel: The same simulated train of exponential (red line) with photon noise added on (black line). The linear fits are marked (dashed blue lines, both panels).

are listed in Tab.2.2. The $e$-folding time is fixed for each simulation. The cadence is Poisson-distributed around the average value, the amplitude is random-uniform between 0.5 and 1.5 the average value. The light curve becomes *"saw-toothed"*, but non-periodic, with exponential descending trends (Fig.2.14, bottom panel). This new light curve is then randomized according to the pixel average count statistics,

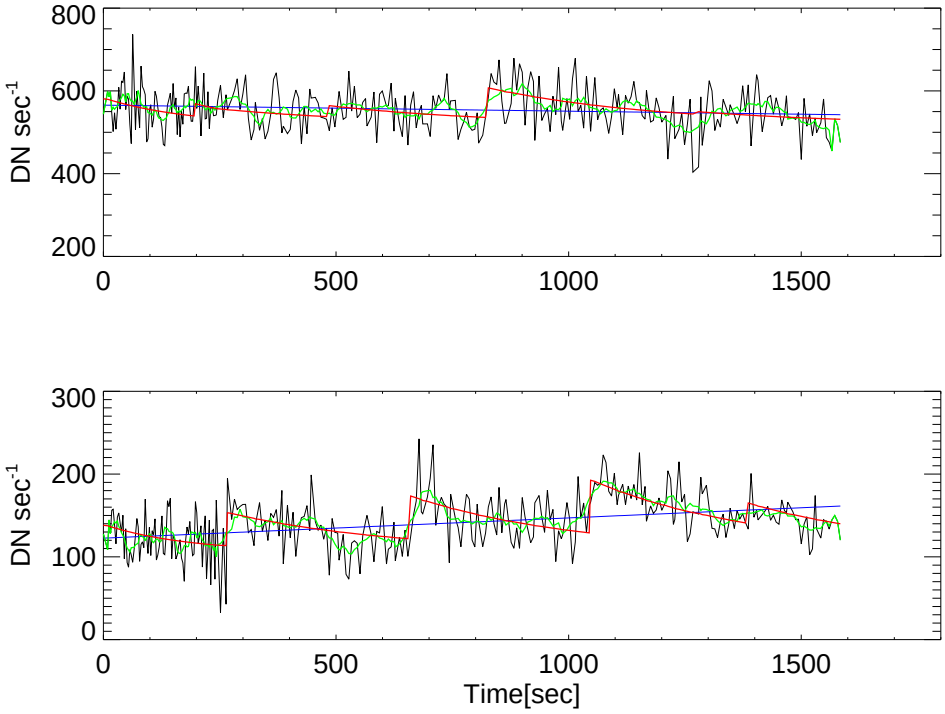


Figure 2.15 Light curves of two other pixels obtained from Monte Carlo simulations with trains of exponentials. The linear fits are marked (blue lines); 9-point ($\sim$ 1 min) running averages are shown (green).

as done for the constant light curve (Fig.2.14 bottom panel, and Fig.2.15).

Again, we replicate this procedure for all valid pixels, and obtain new datacubes, which we can analyze as if they were real data. We perform a sample exploration of the parameter space. In particular, we consider reasonable loop cooling timescales as possible $e$-folding times, i.e. $\tau$ = 180 s, 360 s, 540 s. The larger values appear as probably more realistic for active region loops of length $5 - 10 \times 10^9$ cm, according to the loop cooling times ($\tau_s$), which are of the order of (Serio et al., 1991):

$$\tau_s = 4.8 \times 10^{-4} \frac{L}{\sqrt{T_0}} \sim 120 \frac{L_9}{\sqrt{T_{0,7}}} \tag{2.16}$$

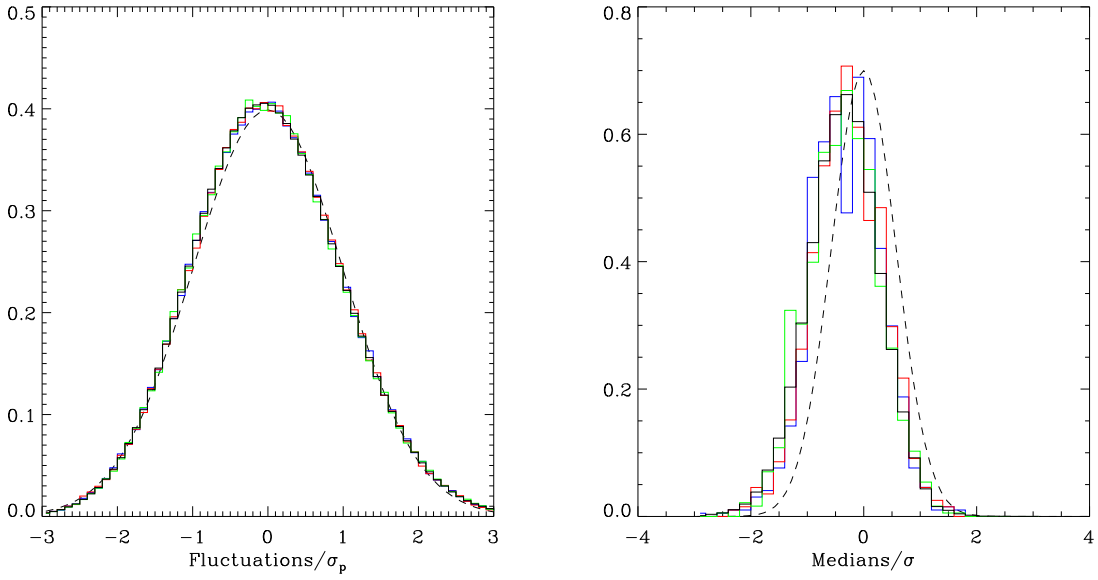


Figure 2.16 Identical to Figure 2.17 but obtained with the Monte Carlo simulation with: $A = 60$ DN/s, $\tau = 360$ s, and $dt = 360$ s.

where $L$ is the loop half-length ($L_9$ in units of $10^9$ cm) and $T_0$ is the loop maximum temperature ($T_{0,7}$ in units of $10^7$ K). We are aware that there is probably a non-trivial link between the time distances between perturbations, their amplitude and the local brightness, nevertheless we make a simple choice for the exploration. The average time distance between two subsequent perturbations cadence ranges around the chosen $e$-folding time by a factor between 2 and 3. The basic amplitude $A$ is chosen to be the same everywhere, and we make three different sets of simulations with $A = 30$, 60 and 90 DN/s.

### 2.4.3 Comparison with Observation

We can compare the values listed in the Tab.2.1 and Tab.2.3, that show the results of the data analysis and the results of the Monte Carlo simulations respectively. The median values from the simulations approach those obtained from the data for all values of $\tau$, for A = 60 DN/s and for time distances of the order or larger than $\tau$ (Figures 2.11 and 2.16). The simulation with A=60, $dt$=360 and $\tau$=360, besides, is the value that best approaches the values in the obsservation. It is worth commenting further on the distribution of median values obtained from the individual pixels (Figure 2.11 and 2.16, right panel). As we have discussed, a negative median is indicative of exponentially decreasing intensity and cooling plasma (and also Poisson photon statistics to some degree). However, a sizeble fraction of the observed median values are positive. Without the benefit of our simulations, we might conclude that these pixels do not have cooling plasma. The good agreement between the observed (Figure 2.11, right panel) and simulated (Figure 2.16, right panel) distributions, both in terms of the centroid offset and the width, shows that the observations are in fact consistent with all of the pixels having cooling plasma. Positive median values occur when photon statistics mask the relative weak signal of the exponentially decreasing intensity (compare the two light curves in Figure 2.15). The resulting median value deviates from 0 more than it should. Our claim that up to 60% of the observed deviations can be explained by photon statistics is therefore conservative. The actual contribution from photon statistics is likely to be smaller.

Figure 2.15 confirms that it is not trivial to discern the presence of parts of decaying exponential in a noisy lightcurve. It is only after an accurate statistical analysis and an accurate modeling through Monte Carlo simulations that we can ascertain their presence in excess of Poisson noise. However, once ascertained their presence, we may hope to visualize some of these exponentials at least in the cases where the median is particurarly negative. One of these cases is shown in Fig.2.17. Indeed,

we can already see such trends in this light curve, that we mark with exponential segments, obtained from fitting the related segment of the light curve. Although this case cannot be taken as a proof, it shows that this effect is realistic and, in a sense, closes our loop.

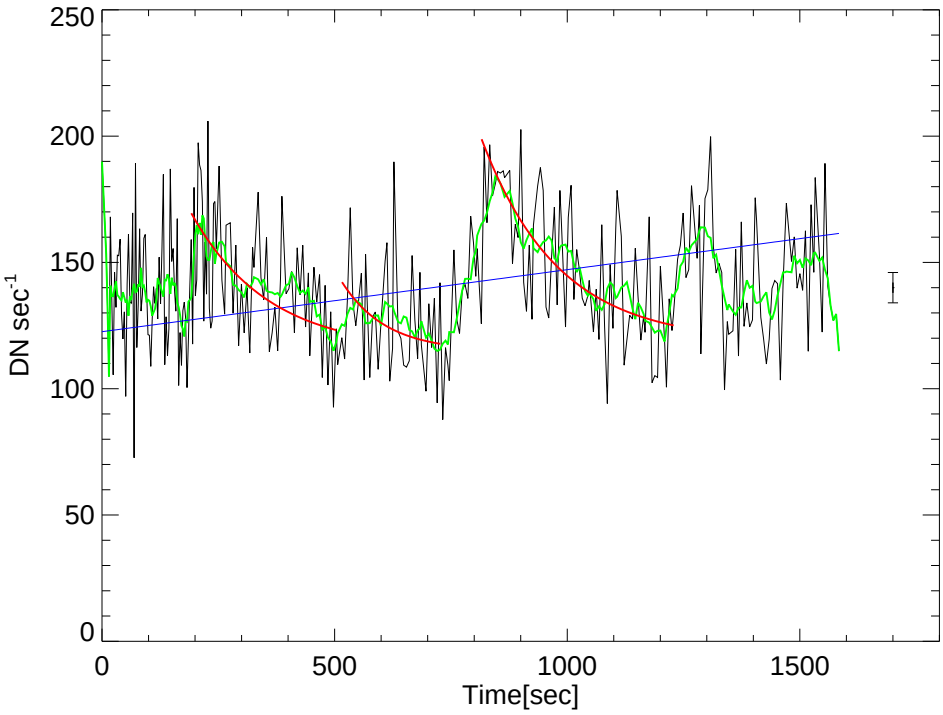


Figure 2.17 Light curve of a selected pixel, the lower indicated by the arrow in Figure 2.8. The linear fits are marked (blue lines); 9-point ($\sim$ 1 min) running averages are shown (green). Exponentials lines (red) well fit the respective data segments.

Table 2.3. Monte Carlo Simulations Results

| $A$ [1] | $dt$ [2] | $\tau$ [2] | $Thr = 30$ [1] | Thr=800 | Thr=1600 |
|---|---|---|---|---|---|
| 0 | 0 | 0 | -0.0164±0.0004 | -0.0096±0.0009 | -0.0096±0.0017 |
| 30 | 360 | 360 | -0.0184±0.0004 | -0.0105±0.0005 | -0.0087±0.0017 |
| 30 | 540 | 360 | -0.0189±0.0004 | -0.0099±0.0009 | -0.0086±0.0018 |
| 60 | 360 | 180 | -0.0322±0.0004 | -0.0136±0.0008 | -0.0109±0.0017 |
| 60 [3] | 360 | 360 | -0.0253±0.0004 | -0.0112±0.0009 | -0.0070±0.0017 |
| 60 | 360 | 540 | -0.0228±0.0004 | -0.0103±0.0009 | -0.0063±0.0018 |
| 60 | 540 | 360 | -0.0283±0.0004 | -0.0124±0.0008 | -0.0087±0.0017 |

Note. — Table 2.3 shows the simulated values of averaged medians, with errors, for light curves with trains of decaying axponentials. The cadence is Poisson-distributed around the average value, the amplitude is random-uniform between 0.5 and 1.5 the average value, A. A = 0 is the *null-hypothesis* (no perturbation).

[1]The amplitude of nanoflares and the threshold of intensity for the simulated pixels are in unit of DN $s^{-1}$.

[2]The sampling spacing ($dt$) and the $e$-folding time ($\tau$) are in seconds.

[3]Simulation that best approaches the values measured in the observation.

Table 2.4. Monte Carlo Simulations Results for Sub-regions

| A | dt | Sub-reg 1 | Sub-reg 2 | Sub-reg 3 |
|---|---|---|---|---|
| 0 | 0 | -0.016±0.002 | -0.013±0.002 | -0.018±0.002 |
| 30 | 360 | -0.018±0.002 | -0.018±0.002 | -0.018±0.002 |
| 30 | 540 | -0.021±0.002 | -0.017±0.002 | -0.020±0.002 |
| 60 | 360 | -0.021±0.002 | -0.021±0.002 | -0.024±0.002 |
| 60 | 540 | -0.024±0.002 | -0.024±0.002 | -0.028±0.002 |

Note. — Table 2.4 shows the simulated values of averaged medians, with errors, for selected sub-regions (Fig.2.8) obtained from Monte Carlo simulations, with units as in Tab.2.3.

## 2.5 Interpretation and Possible Implication on Coronal Heating

We analyzed a very high cadence observation which allowed us to detect a significant deviation from the expected Gaussian/Poissonian distribution of the emission fluctuations in time. This deviation is an asymmetry toward the negative side of $x$-axis, i.e. an excess of the number of negative fluctuations, at higher and higher significance on larger and larger scales, from the single pixels to the whole active region. These negative fluctuations (corresponding to reduced intensity) are greater in number but weaker in amplitude, so that the median fluctuation is negative compared to a mean of zero. The negative median can be explained with light curves consisting mainly of sequences of exponential decays: the emission spends a longer time below the mean than above it. We quantified this excess by measuring the median of the fluctuations, which is in fact negative. As well the effect is widespread and enhanced when summed over the region.

A magnetic strand that is heated by a small impulsive events evolves in a well defined manner (Warren et al., 2002, 2003; Patsourakos & Klimchuk, 2005; Testa et al., 2005; Reale, 2007; Reale & Orlando, 2008), and its light curve (intensity vs. time) has a characteristic shape, as shown in Fig.2.18. The intensity rises quickly as the nanoflare occurs, levels off temporarily, then enters a longer period of exponential decay as the plasma cools. The light curve is so very asymmetric, the strand is bright for less time than it is faint, and when it is bright it is much brighter than the temporal average.

This particular example (Fig.2.18) comes from a numerical simulation and represents a light curve of a single strand that is heated by short and intense heat pulse. Before the heating the strand is cold and so invisible. The heat pulse lasts 60 s and brings the strand to a maximum temperature $\log T \approx 7$. The plasma confined in

the strand transports energy and can move only along the magnetic field line, so to describe this physical system we can use a one-dimensional hydrodinamic model, through the equations (Peres et al., 1982; Betta et al., 1997):

$$\frac{dn}{dt} = -n\frac{\partial \mathrm{v}}{\partial s} \tag{2.17}$$

$$nm_H\frac{d\mathrm{v}}{dt} = -\frac{\partial p}{\partial s} + nm_H g + \frac{\partial}{\partial s}\left(\mu\frac{\partial \mathrm{v}}{\partial s}\right) \tag{2.18}$$

$$\frac{d\varepsilon}{dt} + w\frac{\partial \mathrm{v}}{\partial s} = Q - n2\beta P(T) + \mu\left(\frac{\partial \mathrm{v}}{\partial s}\right)^2 + \frac{\partial}{\partial s}\left(\kappa T^{5/2}\frac{\partial T}{\partial s}\right) \tag{2.19}$$

$$p = (1+\beta)\, nK_B T \tag{2.20}$$

$$\varepsilon = \frac{3}{2}p + n\beta\chi \tag{2.21}$$

$$w = \frac{5}{2}p + n\beta\chi \tag{2.22}$$

where $n$ is the hydrogen number density; $t$ is the time, $s$ is the coordinate along the field line; v is the plasma velocity; $m_H$ is the mass of hydrogen atom; $p$ is the pressure; $g$ is the component of gravity along the field line; $\mu$ is the effective coefficient of compressional viscosity (including numerical viscosity); $\beta = n_e/n$ is the ionization fraction where $n_e$ is the electron density; $T$ is the temperature; $\kappa$ is the thermal conductivity ($\simeq 9 \cdot 10^{-7}$ erg cm$^{-1}$ s$^{-1}$ K$^{-7/2}$); $K_B$ is the Boltzmann constant; $\chi$ is the hydrogen ionization potential; $P(T)$ are the radiative losses per unit emission measure (Raymond & Smith, 1977); $Q(s,t)$ is the volumetric power input to the solar atmosphere:

$$Q\left(s,t\right) = H_{steady} + H_0\ f(t)\ g(s) \tag{2.23}$$

where $H_{steady}$ is the steady heating term that balances radiative and conductive losses for the static initial atmpsphere and the second term describes the heat pulse as a separable function of space and time.

It simulates an observation that would be made by the X-Ray Telescope (XRT) on the Hinode spacecraft in the Al_poly filterband (Guarrasi et al., 2010). This results in a distribution of intensities that is also very asymmetric. As we have seen a good measure of the asymmetry is the difference between the median and mean values. The median intensity over the whole simulation (7.0 DN/s) is much less than the mean (16.6 DN/s). This is a generic property of light curves that are dominated by an exponential decay, as is the case with nanoflares. We used this property to demonstrate that nanoflares are occurring throughout a particular active region that we studied in detail.

Using also Monte Carlo simulations with a model of small scale fast energy release followed by slower cooling, we obtain evidence that only part of this asymmetry can be explained by Poisson photon statistics. The remainder is explainable with a tendency for exponentially decreasing intensity, such as would be expected from a cooling plasma produced, e.g., from a nanoflare.

Previous attempts to determine the nature of coronal heating outside of isolated warm loops have been inconclusive. Our study provides strong evidence for widespread cooling plasma in active region AR10923. The fact that the result is similar for the whole active region is important because it shows that the effect is widespread and real. Were it due simply to random fluctuations, the magnitude would decrease as more and more pixels are included in the statistics. This suggests heating that is impulsive rather than steady, which in turn suggests that nanoflares play a universal role in active regions. We favor nanoflares occurring within the

corona, but our observations may also be consistent with the impulsive injection of hot plasma from below, as has recently been suggested De Pontieu et al. (2011).

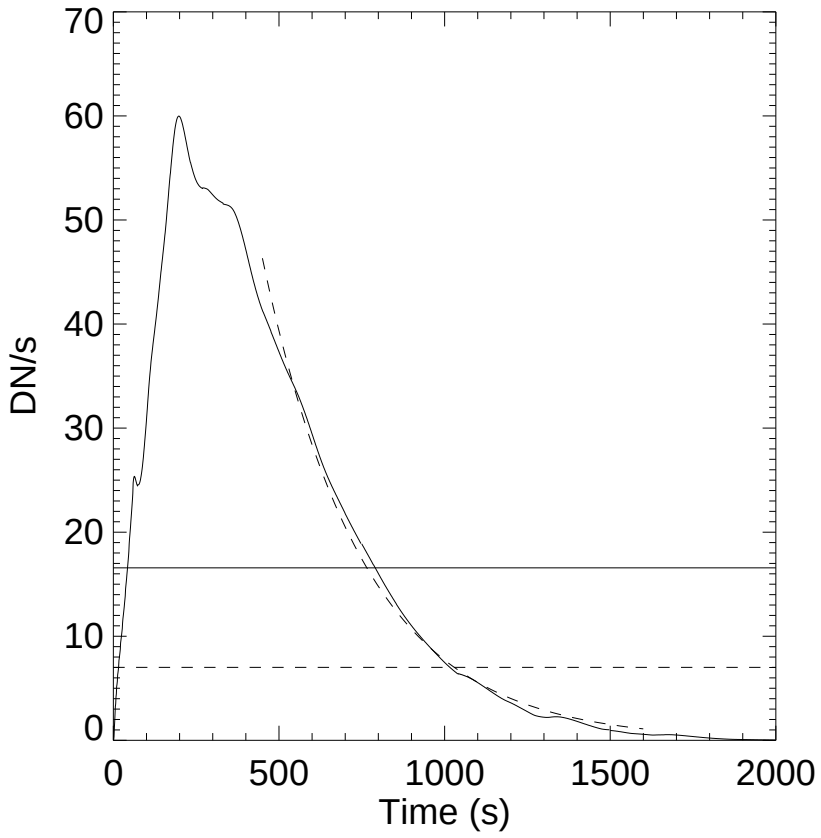


Figure 2.18 This particular example comes from a numerical simulation and represents an observation that would be made by the X-Ray Telescope (XRT) on the Hinode spacecraft (Kosugi et al., 2007). The light curve (solid curve) is in the XRT Al_poly filterband obtained from a hydrodynamic simulation of the plasma confined in a loop strand ignited by a heat pulse (nanoflare), and that cools down following an exponential decay trend (shown by the dashed curve). The heat pulse lasts 60 s and brings the strand to a maximum temperature $\log T \approx 7$. The straight horizontal lines show the mean (solid line) and the median (dashed line) of the simulated intensity.

### 2.5.1 Loop and Nanoflares Parameters Estimate

#### Loop substructuring

We can make simple estimates of some characteristic implied by the parameters constrained with Monte Carlo simulations. Let us assume that the events that we resolve are able to heat an active region loop, that an event observed in a pixel heats a whole loop strand, that the intensity each events is able to bring the loop to a temperature of 10 MK, with an average temperature of 3 MK, that the loop has a total length of $2L = 5 \times 10^9$ cm.

From Monte Carlo simulations, we find that an appropriate average event cadence is:

$$dt \geq 360 \quad s$$

For an observation duration:

$$\Delta t = 1600 \quad s$$

the number of events per pixel is:

$$dn \approx \frac{\Delta t}{dt} \leq 4$$

If we assume an average loop half-length ($10^9$ cm):

$$L_9 \approx 2.5$$

and a loop diameter (typically 10% of the loop length):

$$D \approx 0.1 \times 2L \approx 0.5 \times 10^9 \text{cm} \approx 7 \quad \text{pix}$$

The number of events in the loop is:

$$n \approx dn \times D \leq 30$$

From loop scaling laws (Rosner et al., 1978b) , we estimate the equilibrium pressure corresponding to the maximum temperature (MK) $T_{max,6} = 10$, possibly due to a heat pulse:

$$p \approx 0.3 \frac{T_{0,6}^3}{L_9} \sim 100 \text{ dyne cm}^{-2}$$

the pulse heating rate per unit volume in units of $10^{-3}$erg cm$^{-3}$ s$^{-1}$:

$$H_{-3} = 3p^{7/6}\ L_9^{-5/6} \sim 300$$

and the pulse energy flux over the whole loop:

$$F = H \times 2\ L \sim 0.3 \times 5 \times 10^9 \sim 1.5 \times 10^9 \quad \text{erg cm}^{-2}\ \text{s}^{-1}$$

The energy released by the nanoflare in the loop is then:

$$E_n = F\ n\ t_n\ dA_n \leq 1.5 \times 10^9 \times 30 t_n\ dA_n \approx 4 \times 10^{10} t_n\ dA_n$$

where $t_n$ is the nanoflare duration and $dA_n$ is strand cross-section area. Let's now consider the average loop conditions. For a loop cross-section of:

$$A = \pi\ R^2 \sim \pi 6 \times 10^{16} \sim 2 \times 10^{17} \ \text{ cm}^2$$

and an average loop heating rate per unit volume for steady state ($T_{max,6} = 3$):

$$\langle H \rangle \sim 0.002 \ \text{ erg cm}^{-3}\ \text{s}^{-1}$$

The loop total thermal energy in the observation can be estimated as:

$$E_L \approx \langle H \rangle \; 2 \; L \; A \; \Delta t \approx 0.002 \times 2 \times 2.5 \times 10^9 \times 2 \times 10^{17} \times 1600 \approx 3 \times 10^{27} \quad \text{erg}$$

By equating $E_n \approx E_L$, we obtain:

$$t_n \frac{dA_n}{A} \geq \frac{3 \times 10^{27}}{4 \times 10^{10} \times 2 \times 10^{17}} \approx 0.5$$

So the product of the nanoflare duration (in s) and the fractional strand area is of the order of 1. For instance, if the nanoflare lasts 60 s we fill the loop with about 120 strands. The implication would be that the strand diameter is more than $10^7$ cm, i.e. a fraction of arcsec, not far from the resolution of the current instruments. Probably these are the most significant nanoflare events, the high tail of a distribution. The bulk of the events may occur with higher frequency and in finer strands.

**Nanoflares energy**

We can assume that the amplitude of the best-fit model exponential is the amplitude corresponding to a single nanoflare: $A = 60$ DN/s, which heats a whole loop strand. From the filter response function, assuming a temperature $\log T \sim 6.5$ we derive the emission measure per unit area (1 pixel):

$$EM_{pix} \approx 4 \times 10^{42} \;\; \text{cm}^{-3}$$

We can estimate the total emission measure along a loop pixel strip (total length $2L = 5 \times 10^9$ cm $\approx 70$ pixel):

$$EM_L = EM_{pix} \; L_{pix} \approx 4 \times 10^{42} \times 70 \sim 3 \times 10^{44} \;\; \text{cm}^{-3}$$

The corresponding emitted energy rate (for an emissivity $P(T) \approx 10^{-22}$ erg cm$^{-3}$

$s^{-1}$ for $\log T \sim 6.5$, Rosner et al., 1978b) is:

$$E_r \approx EM_L \; P(T) \approx 3 \times 10^{22} \;\; \text{erg s}^{-1}$$

Assuming for the emission perturbation $e$-folding time the best-fit value $\tau = 360$ s, the total emitted energy in a loop pixel strip is:

$$E_L \sim E_r \; \tau \sim 360 \times 3 \times 10^{22} \approx 10^{25} \quad \text{erg}$$

## 2.6 Conclusions

As we report here for the first time, there is a new method for detecting nanoflares from intensity fluctuations that does not depend sensitively on the noise. The typical light curve of a flare or micro-flare is very asymmetric. The strand is bright for less time than it is faint, and when it is bright it is much brighter than the temporal average. This results in a distribution of intensities that is also very asymmetric. As we saw a good measure of the asymmetry is the difference between the median and mean values. The median intensity is much less than the mean, and this is a generic property of light curves that are dominated by an exponential decay, as is the case with nanoflares. We used this property to demonstrate that nanoflares are occurring throughout a particular active region that we studied in detail. Since the light curve at each pixel in the image set is a composite of many light curves from along the line-of-sight, the asymmetries of the intensity distributions and the differences between the median and mean values are small. We used both statistical analysis and quantitative modeling to show that the differences are nonetheless significant and consistent with widespread nanoflaring in the active region.

For the first time we applied this method to a very high cadence observation which allowed us to detect a significant deviation from the expected Poissonian dis-

tribution of the emission fluctuations in time. The deviation is an asymmetry toward the negative side, i.e. an excess of the number of negative fluctuations, at higher and higher significance on larger and larger scales, from the single pixels to the whole active region. These negative fluctuations (corresponding to reduced intensity) are greater in number but weaker in amplitude, so that the median fluctuation is negative compared to a mean of zero. We quantified this excess by measuring the median of the fluctuations, which is in fact negative. As well the effect is widespread and enhanced when summed over the region. The negative median can be explained with light curves consisting mainly of sequences of exponential decays: the emission spends a longer time below the mean than above it.

Using also Monte Carlo simulations (with a model of small scale fast energy release followed by slower cooling), we obtain evidence that only part of this asymmetry can be explained by Poisson photon statistics. The remainder is explainable with a tendency for exponentially decreasing intensity, such as would be expected from a cooling plasma produced, e.g., from a nanoflare.

The results of this work shed more light on the heating problem of the solar corona, and are a clear evidence of a widespread nanoflaring activity over the whole active region. Thus in this thesis we suggest that nanoflares are a universal heating process within active regions.

# Chapter 3

# Single-Filter Temperature Analysis

## 3.1 Temperature Diagnostics and Thermal Structuring

The investigation of the thermal structure of solar active region and coronal loops is crucial for their deep physical comprehension and to understand the underlying heating mechanisms. In the solar corona the diagnostic of temperature is not a trivial task, since no direct measurements are available.

Since the plasma is optically thin, we receive information integrated on all the plasma column along the line of sight. The problem is to separate the distinct contributions to thermal component and reconstruct the detailed thermal structure along the line of sight. Moderate diagnostic power is allowed by imaging instruments, by means of multifilter observations. Filter ratio maps provide information about the spatial distribution of temperature and emission measure (e.g.,Vaiana et al., 1973).

The emission of an optically thin isothermal plasma as measured in a *j-th* filter passband is:

$$I_j = EM\ G_j(T) \tag{3.1}$$

where $T$ is the temperature and $EM$ is the Emission Measure, defined as

$$EM = \int_V n^2 dV \tag{3.2}$$

where $n$ is the particle density, and $V$ the plasma volume. The temperature function

$$G_i(T) = \int d\lambda f(\lambda, T) g_i(\lambda) \tag{3.3}$$

is the plasma flux $f(\lambda, T)$, through the response function of the $i$-th filter $g_i(\lambda)$ (Fig. 3.1). Assuming an isothermal source, $G_i(T) = G_i(T_0) = cost.$, the ratio in two different filter bands, $i$-th and $j$-th (*Filter Ratio*), is a function of the temperature alone, because the effect of EM ($n_e^2(T_0) = cost.$) cancels in the measured flux.

This ratio is a single-value function of the temperature (Fig.3.2). So it is possible to obtain the temperature map of the region pixel by pixel by the inversion of this relationship, and by the response function of the used analysis filters.

The limitations of this method are substantial, in particular, one filter ratio value provides one temperature value for each pixel. This is a reliable measurement, within experimental errors, as long as the assumption of isothermal plasma approximately holds for the plasma column in the pixel along the line of sight. If the plasma is considerably multi-thermal, the temperature value is an average weighted for the instrumental response. The interpretation of the related maps is not a trivial task, since the response is a highly non-linear function of the emitting plasma temperature. In addition, it is fundamental to know precisely the instrument response, in order to avoid systematic errors, which propagate dangerously when filter ratios are evaluated.

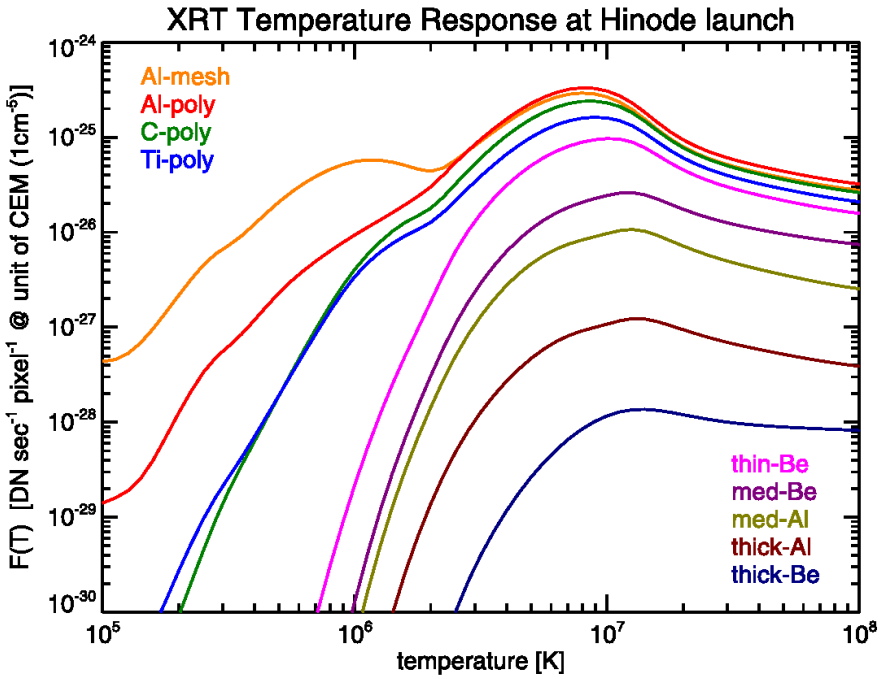


Figure 3.1 Temperature Response Function of XRT focal-plane filters (*i*). The curves plot the combination of the total instrument response (as function of wavelength) with the coronal plasma emission model (ATOMDB/APEC) for a columnar EM of $10^{30}$ cm$^{-5}$ in unit of wavelength (Narukage et al., 2011).

In this sense, broadband filters provide robust thermal diagnostics, because they are weakly dependent on the details of the atomic physics models, e.g., on the presence of unknown or not well-known spectral lines, on the choice of element abundances. Narrowband filters can show non-unique dependencies of filter ratio values on temperature (e.g., Patsourakos & Klimchuk, 2007), due to the presence of several important spectral lines in the bands, but a more general problem can be the bias to detect narrow ranges of temperatures forced by the specific instrument characteristics. This problem can be important especially when the distribution of the emission measure along the line of sight is not simple and highly non-linear (e.g., Reale et al., 2009).

Reale et al. (2007) improved the filter ratio method combining different XRT filters (Sec. 1.4.1). They used the XRT filters Al_poly (F1), C_poly (F2), Be_thin (F3), Be_med (F4), and Al_med (F5). Softer filters F1 and F2 are more sensitive to the emission of cooler plasma than are the harder filters F4 and F5. They used the ratio between the geometric mean of the emission detected in all the available

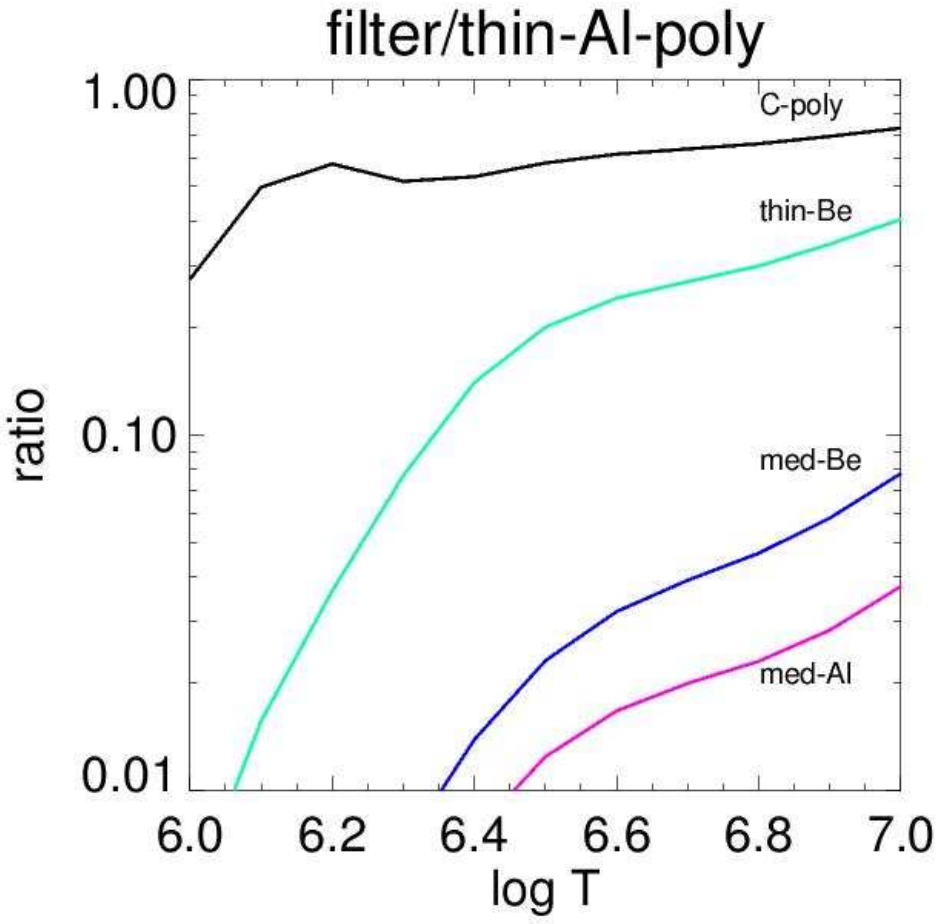


Figure 3.2 Ratio of different XRT analysis filters, all with the same denominator (thin-Al-poly), give different curves *Filter Ratio/temperature*. In the $x$-axis the temperature in logaritmic scale.

filters and the emission $I_j$ in a single ($j$-$th$) filter given by Eq. 3.4:

$$CRF_j = \frac{(\Pi_{i=1}^{n} I_i)^{\frac{1}{n}}}{I_j} = \frac{(\Pi_{i=1}^{n} G(T)_i)^{\frac{1}{n}}}{G(T)_j} \tag{3.4}$$

The geometric mean allows them to normalize the sensitivity of the soft and hard filters, and to optimize the statistics of the regions where the signal is high in most filters. A further improvement is obtained with the product of the ratios computed for the two softest filters, i.e., Al_poly and C_poly:

$$CIFR = CIFR_1(T) \times CIFR_2(T) \tag{3.5}$$

The resulting map of this *combined improved filter ratio* (CIFR) shows a very high degree of thermal structuring in the core loop arcade (Reale et al., 2007).

For active regions with single filter X-Ray instrument observation, temperature analysis should be not possible without maybe spectral analysis. Instead a high cadence observation of an active region made with a single Hinode/XRT filter allows us to use an alternative approach: we measure the time fluctuations of the pixel count rate and use the variance as temperature proxy.

I show here preliminary results and discuss limitations. In particular in the Sections 3.2 and 3.3 I show the theoretical approach and its application, to real data, respectively. In the Section 3.4 I show the results and discuss limitations of method.

## 3.2 Single-Filter Method

Most solar X-ray telescopes, such as Yohkoh/SXT and Hinode/XRT, use CCD detectors in an integrating mode and are designed to make temperature estimates from multiband filter photometry (Sec. 3.1). In the subsequent, I will show that such instruments can be used in a different way to perform a different type of spectroscopy.

Each photon, in the energy range of KeV, that hits a single pixel of a CCD detector produce hundreds of electrons. The number of electrons is proportional to energy of photons, allowing a measurement of spectral information with CCD-imaging detectors. Kahler (1976) introduce the possibility of determining physical parameters of the solar corona through the use of single soft X-ray filters, as long as a single X-Ray photon produces a large enough number of photoelectrons in the CCD to allow the spectroscopy. Thereafter Labonte & Reardon (2007) introduced the so-called *Photon Spectroscopy*, with the main goal of determining the mean plasma temperature, measuring the variance in intensity of a series of repeated images, through a single filter, of a relatively stable X-ray source.

Since the photon energy is related to the underlying coronal spectrum, we can deduce the mean plasma temperature measuring the amount of energy released by individual photon, striking the CCD detector.

## 3.3 Data Analysis

### 3.3.1 Observation

The data that we used was collected from the *X-Ray Telescope* (XRT) on-board on the HINODE satellite (Shimizu, 2002). The active region under analysis was observed when it was located closer to the disk limb. The data set under analysis consists of 265 couples of $384 \times 384$ pixels images, taken in the Ti_poly filter band

(Fig.3.3). The data set have a cadence of 15 seconds, with exposure times ($\sim 0.73$ sec) for a total coverage of $\sim 60$ min. The active region was observed in 1 April 2010, starting at 15:04:19 UT. This high cadence observation provided by HINODE/XRT let us follow an alternative way using a single filter diagnostics.

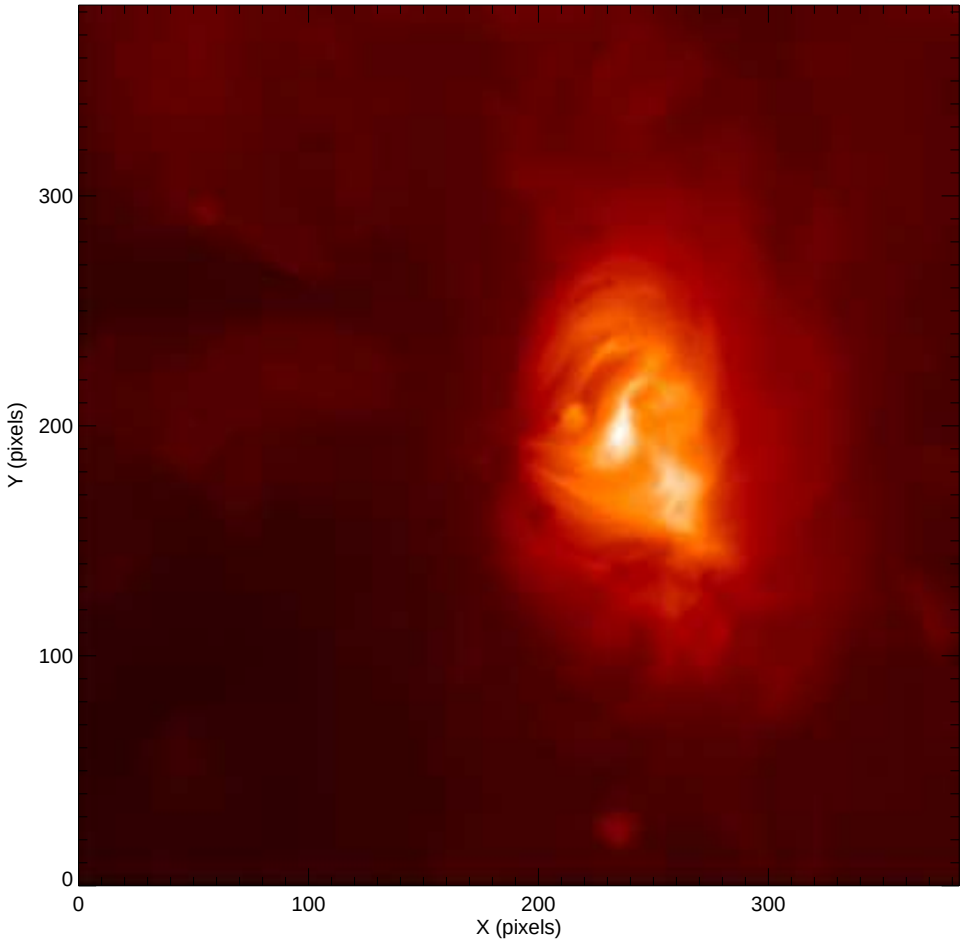


Figure 3.3 Active region observed with the Hinode/XRT Ti_poly filter on 01 April 2010 at 15 UT.

### 3.3.2 Conversion Factor

In general, since the photon noise follows a Poisson distribution, the standard deviation of $dN$ ($d\sigma$) could be derived as the square root of the photon counts as (Kano & Tsuneta, 1995; Katsukawa & Tsuneta, 2001; Narukage et al., 2011):

$$d\sigma = \sqrt{dN} \tag{3.6}$$

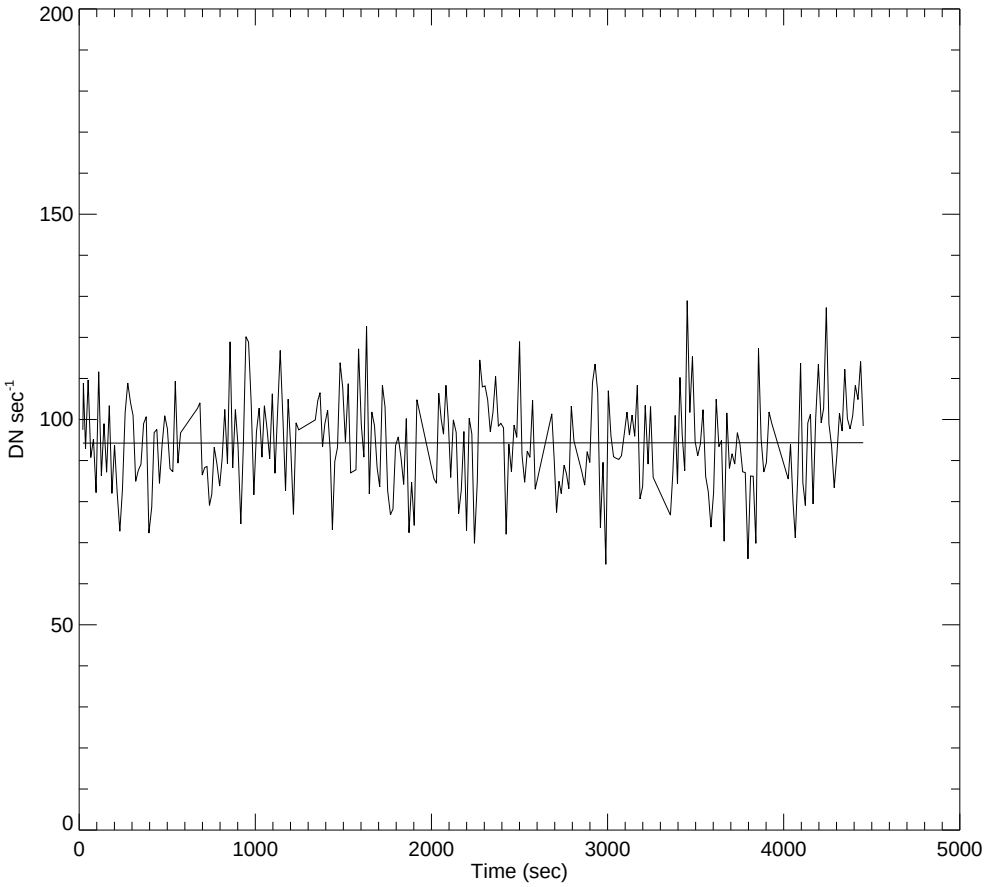


Figure 3.4 Light curve of an single accepted pixel, of the active region under analysis. The staight line is the linear fit of the light curve toward to we measure the amplitude of the intensity fluctuations.

and since the electron counts (DN) can be connected with the photon counts by

$$DN = \int \left( \frac{hc}{\lambda} \times \frac{1}{e \times 3.65 \times G} \right) \, dN \tag{3.7}$$

where $h$, $c$, $e$, and $G$ are the Planck's constant, the speed of light, the elementary electric charge, and the system gain of the CCD camera respectively (Narukage et al., 2011). The latter is 57.5 [electron $\mathrm{DN}^{-1}$] for XRT. We can derive the error of DN [$\sigma_{DN}$] as

$$\sigma_{DN} = \sqrt{\int \left( \frac{hc}{\lambda} \times \frac{1}{e \times 3.65 \times G} \right)^2 \, (d\sigma)^2} \; = \tag{3.8}$$

$$= \sqrt{K_i^{(2)}(T) DN} \tag{3.9}$$

where $K_i^{(2)}(T)$ is a conversion factor from DN to photon counts, which depends on the underlying spectrum and therefore on the temperature $T$ of the emitting plasma, in the part of detectable temperature range of XRT from $\sim 1$ MK to $\sim 5$ MK.

### 3.3.3 Temperature Diagnostics

The method is so based on measuring the fluctuations of the pixel light curves, assuming that they are entirely due to the photon noise. This is reasonable because all relevant physical processes are expected to occur on time scales longer than the data cadence.

Eq. 3.9 links the measured data noise to the measured intensity. We can measure $\sigma_{DN}$ directly in the light curves (Fig.3.4) as the root-mean square fluctuations of the measured count rate, provided that the cadence is sufficiently high to ensure that the fluctuations are due to photon noise only. So for each pixel we measure $\sigma_{DN}$ and $I_0$ independently and we can obtain a value of $K_i^2(T)$ for that pixel. Applying

this procedure pixel-by-pixel, we obtain a map of $K_i^2(T)$. From the monotonic relationship shown in Fig.3.5 from a value of $K_i^2(T)$ we obtain a value of temperature. So we obtained a map of temperature.

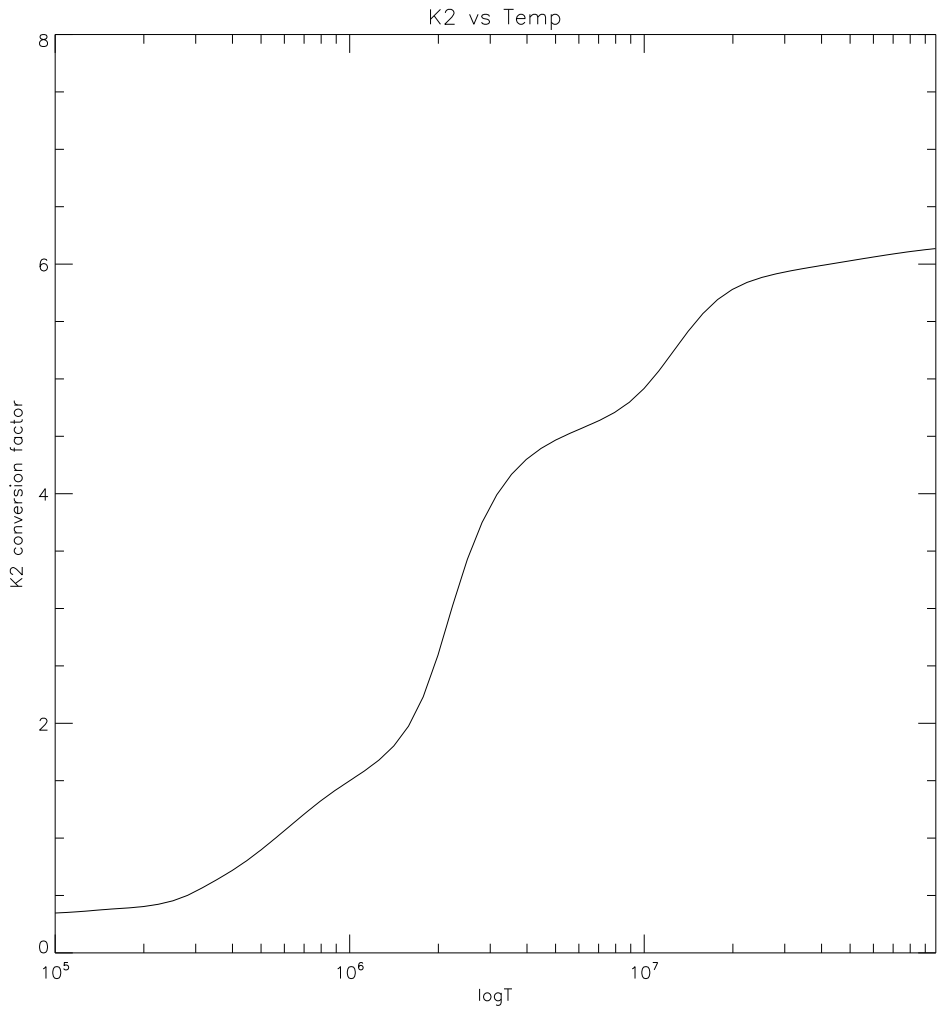


Figure 3.5 Conversion factor $K^{(2)}_{Ti\_poly}$ ($y$ axis) of the Ti_poly filter of XRT to the coronal temperature ($x$ axis) on orbit, considering the contaminant accumulated on the CCD (Narukage et al., 2011).

### 3.3.4 Data Reduction

To select pixels where the previous assumption (see Sec.3.3.3) are valid and measurement is easy we removed pixels at low signal and those showing all kind of low amplitude systematic variations (Terzo et al., 2011):

- pixels with spikes due to cosmic rays
- pixels with micro-flares or other transient brightening
- pixels with slow variations, due for instance to local loop drift or loop motions.

## 3.4 Results

A first example of temperature map obtained in this way is shown in Fig.3.6. The pixels with no temperature value were screened out previously from the analysis (Sec. 3.3.4). Most pixels are found at temperature around $\log T = 6.2$, as shown by the temperature histogram of Fig.3.7. These pixels are localized in the center of the active region. Cooler pixels are localized mostly at the outer boundary of the region, approximately corresponding to the loop footpoints.

The bulk of temperatures found ($\log T \sim 6.2$) are quite lower than expected for an active region ($\log T \sim 6.3 - 6.5$). This is not surprising because we are using the softer filter of the hard/soft filter ratio. The soft filter is more sensitive to cooler plasma, so we are sampling the cool component of the Emission Measure distribution of the active region plasma (Peres et al., 2000; Reale et al., 2009; Testa et al., 2010).

We measured the fluctuations amplitudes, and the standard deviation on their distributions. We derived a temperature map by a single filter observation (Ti_poly) by inverting the formula above (eq.3.9). In the active region is clearly visible that there is a temperature distribution, with brighter regions in the count-rate image (Fig.3.3) that show higher temperature.

Part of the fluctuations might be due to other effects, such as systematic brightness variations. So, if any, the temperature might be even underestimated. This single filter method is however robust, because little dependent on XRT filters calibration (Narukage et al., 2011).

The Applicability of this method is liable to high cadence observations ($dt \leq$

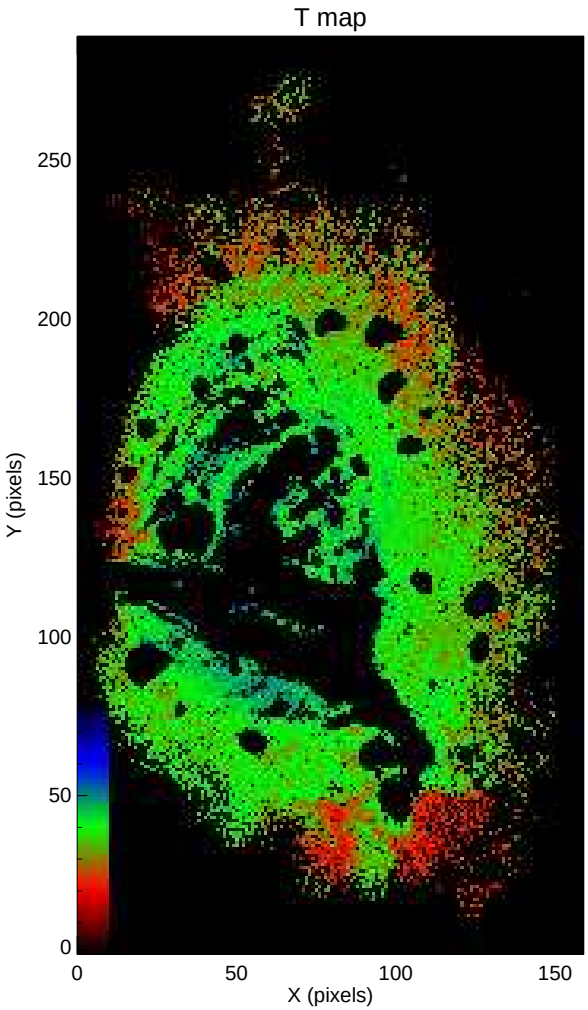


Figure 3.6 In the figure we show the resulting temperature map of the valid pixels (inside the frame of the image). The temperature values are in the range 6.0 $\leq$(red pixels) log T $\leq$ 6.5 (blue pixels). The peak is at log T $\sim$ 6.2 (green pixels).

plasma times). In a multi-thermal line of sight we are sampling the EM where the filter is more sensitive (soft filter in this case). The method is easy to apply to constant or linear light curves. The method should be robust because we expect a little depending on the filter calibration. In our opinion this method could be more efficient and resilient to instrument degradation, with respect to the classic method of filters-ratio.

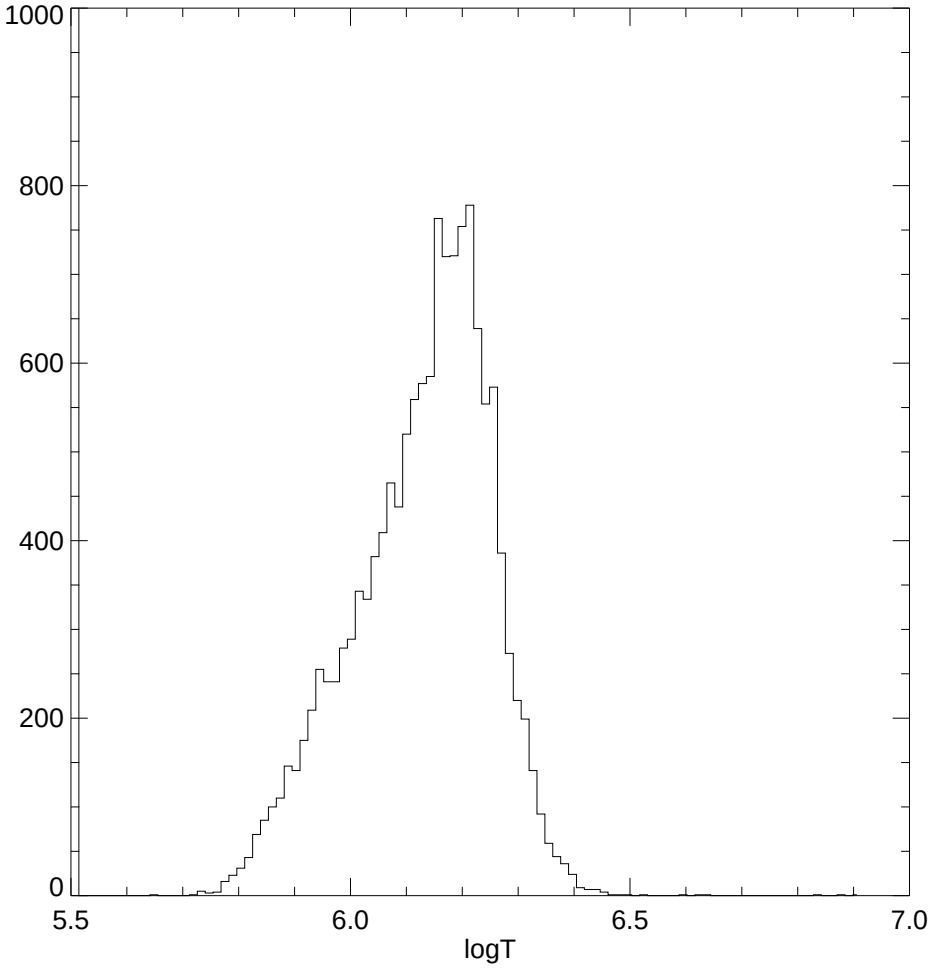


Figure 3.7 The histogram shows that the temperature is in the range $6.0 \leq \log T \leq 6.5$. The peak is at log T $\sim 6.2$.

# Chapter 4

# Conclusions and Future Outlook

The solar corona is highly structured by the solar magnetic field and is hot ($\geq 10^6$ K). It is widely accepted that the origin of the heating of the hot plasma confined in the closed coronal structures (named *loops*) lies in the magnetic field (Vaiana et al., 1973). The determination of the fine thermal structure of the corona is crucial to solve the question of the detailed origin of the coronal heating. The solar *active regions* are good laboratories to investigate this, because they are bright and include a wide variety of structures.

In my PhD work I tried to open new ways to analyze with simple and robust approaches crucial and unsolved problems. For instance, it is currently under debate whether frequent small and rapid heating episodes (*nanoflares*) (Parker, 1988; Cargill, 1994b; Cargill & Klimchuk, 2004), are entirely able to heat the solar corona or partly or only negligibly (Klimchuk, 2006b). Since these phenomena happen under the resolution of present-day satellites, it is compelling to find (Sec. 1.5) new indirect methods of analysis.

In my Phd work, using new methods of analysis (Sec.2.1.1), I obtained evidence that nanoflares are widespread in an active region observed by the X-Ray Telescope on-board the Hinode mission.

I showed that the distributions of intensity fluctuations have small but important asymmetries, either taken from individual pixels, multi-pixel subregions, or the entire active region (Sec.2.3.5). Negative fluctuations (corresponding to reduced intensity) are greater in number but weaker in amplitude, so that the median fluctuation is negative compared to a mean of zero. Using Monte Carlo simulations, I showed that only part of this asymmetry can be explained by Poisson photon statistics. The remainder is explainable with a tendency for exponentially decreasing intensity, such as would be expected from a cooling plasma produced, e.g., from a nanoflare. I strongly suggest that nanoflares are a universal heating process within active regions.

A forward step could be the application of this method to minor emission regions (quiet sun) to address another open question, if maybe the heating mechanisms of the solar corona are the same in its different parts.

The investigation of the thermal structure of solar active region and coronal loops is crucial for their deep physical comprehension and to understand the underlying heating mechanisms. In the solar corona the diagnostic of temperature is not a trivial task, because no direct measurements are available. Most X-ray telescopes works in integrating mode, so them can be used to perform temperature diagnostics through multi-filterbands spectroscopy. A high cadence observation of an active region made with a single-filter Hinode/XRT allowed us to use an alternative approach measuring the time fluctuations of the pixel count rate and their variance as temperature proxy. The method should be robust because I expect a little dependence on the filter calibration.

The problem of the coronal heating, however, is far from be solved. My PhD work was intended, using old and new ways, to give a new and robust contribution to this debate. Results and problems of my present and future work could be applied as technical request to specifications of future space mission instrumentation.

The interaction between the solar magnetic field as source of very energetic impulsive events and the earth's atmosphere is a very compelling problem for astrophysics and space science. Understanding the mechanisms that heats the solar corona to more than 1 million degree is of crucial importance for the insight of our star, and in turn of all stars. Also it will be very important to understand and, maybe in a near future, to predict the happening of this events (*"space weather effects"*) that could affect space missions and, in the end, life on earth.

# Appendix A

# Research Notes

## A.1 *"On the importance of background subtraction in the analysis of coronal loops observed with TRACE".*

Using TRACE coronal observations, we compare the analysis and diagnostics of coronal loop after subtracting the background with two different and independent methods. We analyze sequences of images in the 171 Å and 195 Å filter bands of TRACE. One background subtraction method consists of considering background values obtained by interpolating between concentric strips around the analyzed loop. Another involves a pixel-to-pixel subtraction of the final image after the loop has completely faded out, used by (Reale & Ciaravella, 2006). We compare the emission distributions along the loop obtained with both methods and find that they differ considerably. We also find differences in the related filter ratio and temperature profiles. In particular, the pixel-to-pixel subtraction leads to coherent diagnostics of a cooling loop. After applying the other type of subtraction, the diagnostics are much less clear. The background subtraction should be treated with care when analyzing a loop. The pixel-to-pixel subtraction appears to be more reliable, but its

application is not always possible. Subtraction by means of interpolation between surrounding regions can produce higher systematic errors, because of intersecting structures and the large amount of subtracted emission in TRACE observations.

The problem of background subtraction is serious also for spectral data, because their lower spatial and temporal resolution determines the presence of more structures, and therefore more thermal components, along the line of sight in the same spatial element.

## A.2 Introduction

An important issue in the data analysis of coronal loop observations is background subtraction. Previous work (Del Zanna & Mason, 2003; Testa et al., 2002; Schmelz et al., 2003; Aschwanden & Nightingale, 2005; Reale & Ciaravella, 2006; Aschwanden et al., 2008) have established the importance of separating the true loop plasma from the diffuse foreground and background emission, produced by unresolved coronal structures and instrumental effects. Background subtraction is required because of the many overlapping bright structures and diffuse emission, nearby or along the line of sight, in addition to stray light (DeForest et al., 2009). The accurate extraction of emission along the loop is necessary before applying standard diagnostic methods (such as the filter ratio) to derive physical quantities, e.g., temperature, or applying more detailed loop models. When the background is significant relative to the loop intensity, it will seriously affect the extracted intensity along the loop. There is no standard and generally accepted method of background subtraction; the procedure is then "operator-sensitive" and so in turn are the results.

The problem is particularly important when analyzing observations where the background is a significant fraction of the signal. This happens, for instance, in observations performed with *TRACE* (e.g., Schmelz et al., 2003, Aschwanden &

Nightingale, 2005, Reale & Ciaravella, 2006). Here we explore the dependence and sensitivity of the results on the background subtraction method, by comparing two methods applied to the same loop observed with *TRACE* in more than one filter band. We take advantage of the unique opportunity to apply two different and independent methods of background subtraction to the same dataset. One of the methods (Reale & Ciaravella, 2006 - hereafter RC06) has the advantage that we use as background an image of the loop region when the loop is absent, and that background variations are estimated to be small throughout the observation.

In section 2, we describe the data analysis and background subtraction. Section 3 shows and compares the results obtained by the two background subtraction methods, including implications for temperature diagnostics with filter ratios. In section 4, we discuss the results.

### A.2.1 TRACE Mission

The *Transition Region and Coronal Explorer* (TRACE) satellite (Fig.A.1), was launched on 2 April 1998, was a NASA Small Explorer (SMEX) that images the solar photosphere, transition region and corona, located in a sun-synchronous polar orbit (Handy et al., 1999). The instrument featured a 30-cm Cassegrain telescope with a field of view of $8.5 \times 8.5$ arcmin and a spatial resolution of 1 arcsec (0.5 arcsec pixels), (see Fig.2.1, right panel). TRACE contained multilayer optics and a CCD detector to record three EUV wavelengths and several UV wavelengths. It observed plasmas at selected temperatures from 6000 K to 10 MK with a typical temporal resolution of less than 1 min.

Figure A.1 The *Transition Region and Coronal Explorer* spacecraft (Credits TRACE/NASA).

### Optics

The optical path of TRACE was composed of a set of *entrance filters*, a matched set of thin-film multilayer coatings on two normal-incidence mirrors, two filter wheels behind the primary mirror and a lumogen-coated CCD detector. The instrument was divided into quadrants, each quadrant lodging an optics optimized for a specific wavelength: 171, 195, and 284 Å for the three EUV quadrants, and a range of $1200 - 7000$ Å for the UV quadrant (Handy et al., 1999).

## A.3 Data analysis

We analyze a *TRACE* observation of 13 May 1998, with a 3.5 h time sequence of $1024 \times 1024$ pixel full resolution image in two of TRACE filters (171 Å , 195 Å). This is the same data set selected and analyzed by RC06. The same $512 \times 512$ pixel region of the whole field of view was extracted for the analysis. From these data, four images were selected, in each filter, at the times: 06:36:57 UT, 06:59:35 UT, 07:39:26 UT, and 08:29:34 UT for 171 Å filter; and 06:37:18 UT, 07:00:06 UT, 07:39:47 UT, and 08:30:06 UT for 195 Å filter. The filters have different sensitivities to the temperature of observed plasma. Observations taken at the same time with different filters provide information about the plasma temperature. In particular, the ratio of the emission in two different filter bands, relative to the ratio of the response functions of the filters, infers the temperature of the emitting plasma. Since the filter ratio may be altered by the diffuse emission, originating both in other structures coaligned along the line of sight and in the stray light, it is very important to estimate and remove this background emission. In TRACE observations, the diffuse emission is typically very high and might represent most of the signal.

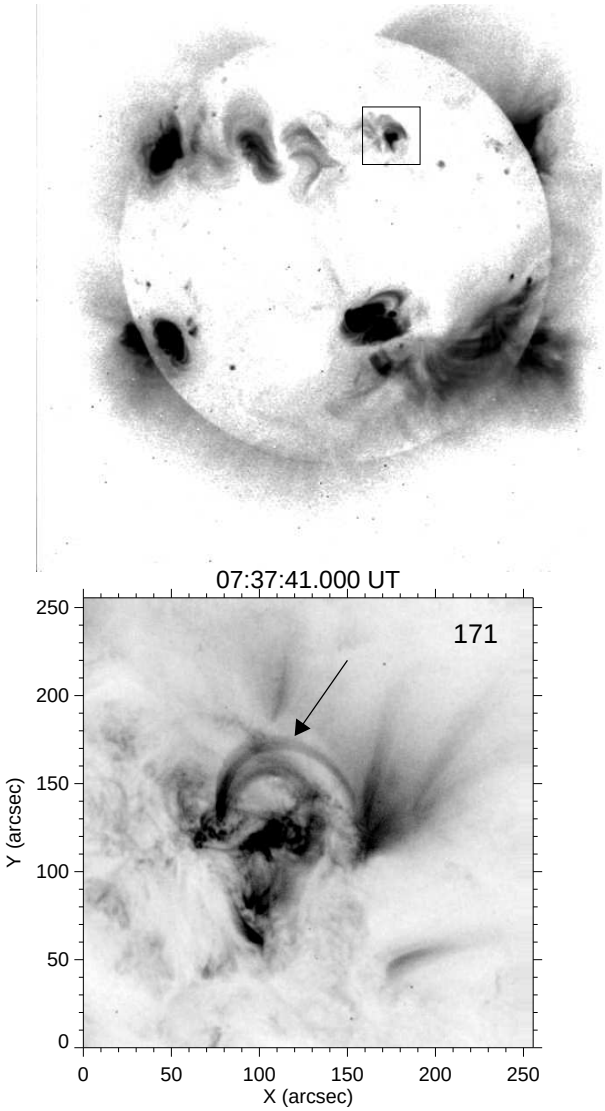


Figure A.2 Loop region as observed with TRACE ($256 \times 256$ *pixels* image) in the 171 Å filter at the labelled time (*bottom panel*). The loop analyzed here is indicated by an arrow. The loop region is located in the inset of the Yohkoh/SXT full disk image (*top panel*). The grey scale is inverted and linear for the TRACE image ($\leq 8$ DN $s^{-1}$ $pix^{-1}$) and inverted and logarithmic for the Yohkoh image (between 10 and 150 DN $s^{-1}$ $pix^{-1}$).

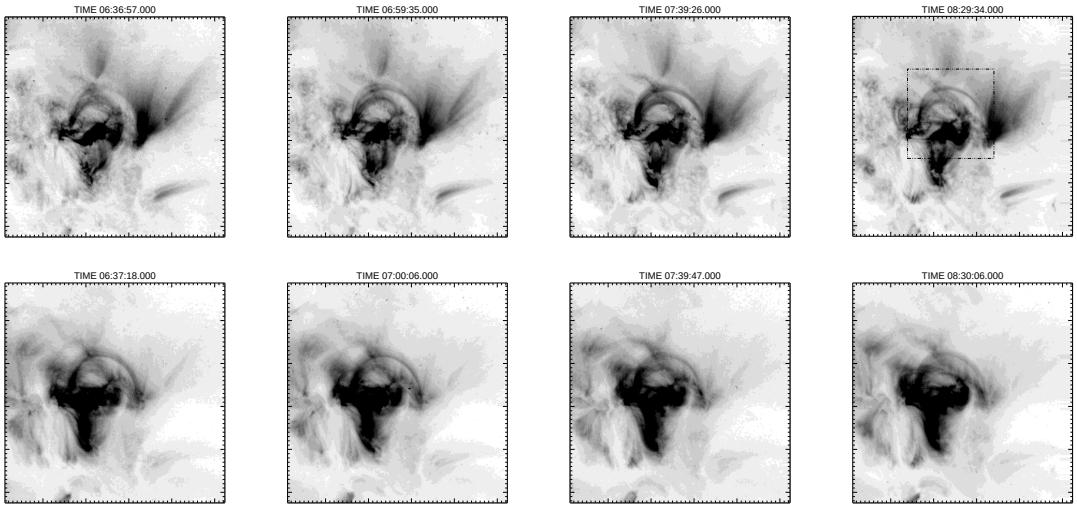


Figure A.3 Loop region (top row: 171 Å ; bottom row: 195 Å ) at subsequent times (from left to right): 06:36:57.000 UT, 06:59:35.000 UT, 07:39:26.000 UT, 08:29:34.000 UT for 171 Å, and 06:37:18.000 UT, 07:00:06.000 UT, 07:39:47.000 UT, 08:30:06.000 UT for 195 Å. The grey scale is inverted and linear between 0.4 and 7 DN $s^{-1}$ $pix^{-1}$ for all images. The frame in the top right image is the part shown in Fig. A.4.

### A.3.1 Loop analysis

We analyze the same loop as in RC06. The loop is selected on the TRACE images (Fig. A.2), and appears as an entire loop in several 171 Å filter images (Fig. A.3). It is clearly visible in the 195 Å filter band (Fig. A.3). The loop is bright, i.e., observed with high quality statistics and a high contrast over the background. It was selected as far as possible to be free from other structures intersecting along the line of sight. The loop evolves in both filter bands. In the 171 Å band, it is faint initially, then brightens reaching a peak of intensity around 07:30 UT, and it fades again, before disappearing at the end of the sequence ($\sim$ 10:00 UT, RC06). In the 195 Å band, the loop is initially brightest and progressively fades out. This loop evolution is even clearer in Fig. A.4, which shows images of the loop region normalized to the final image at 10 UT, where the loop is no longer visible. Here we revisit the data at the four selected times. The data were treated with the standard procedures for *TRACE* data processing contained in the *Solar SoftWare* (*ssw*) and the images were coaligned using a standard cross-correlation technique.

### A.3.2 Background subtraction

We compare the method previously adopted in RC06 with an alternative and independent approach. This method is based on interpolation between emission values in a region close to (but outside) the loop, and is similar to the method adopted in Testa et al. (2002); Aschwanden & Nightingale (2005); Schmelz et al. (2003) and Aschwanden et al. (2008). As a first step, we measure the loop emission. We define a strip enclosing the loop in both of the TRACE filter passbands, and divide the strip into sectors, as shown in Fig. A.5. We analyzed strips of different widths. A width of 10 pixels is a good compromise between too low quality statistics and exceeding too much the loop borders. With this choice, we obtain 27 similar almost square sectors

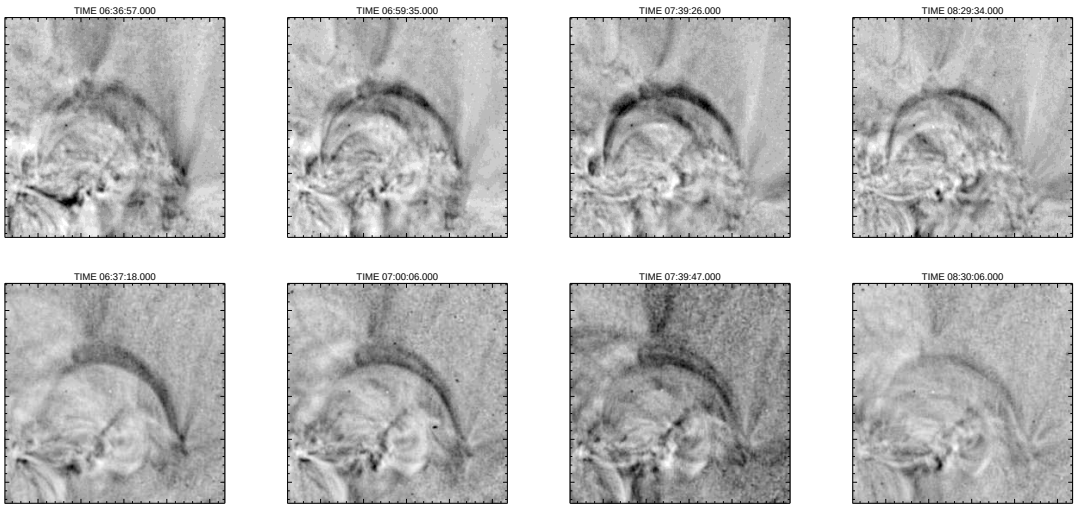


Figure A.4 Zooms of the loop region in Fig. A.3 (frame in the top right image of Fig. A.3). The images (top row: 171 Å ; bottom row: 195 Å ) are normalized to the final image of the sequence (at 10:00 UT), where the loop is no longer visible, to enhance the contrast of the loop evolution. The grey scale is linear between 0.4 and 2.5 (1 means that the emission value is the same as that of the final image).

(RC06). We then mark two other strips, parallel and concentric to the one used to extract the loop emission, one outside and another inside the imaginary circle of which the loop is part. We divide these two additional strips into sectors aligned with those of the central strip (Fig. A.5). These two other strips are used to extract the emission for background subtraction. We place them as close as possible to the loop of interest, avoiding other nearby structures that differ from the analyzed loop. Both strips also have a width of 10 pixels and are divided into 27 sectors to ensure a one-to-one correspondence of these sectors with the sectors patching the loop. In each of the 27 sectors in the two external strips, we compute the mean emission value per pixel. To each sector of the central strip, we assign a background equal to the emission linearly interpolated between the two corresponding sectors of the external strips (Fig. A.5).

To ensure completeness, we also considered a least squares quadratic interpolation. We then considered two additional concentric strips about the analyzed loop, one outer and the other inner. However, the additional outer strips are so far from the central loop they include other bright structures that severely contaminate the procedure and locally alter the otherwise smooth emission distribution. Therefore, the higher order interpolation does not in our case improve our results. Nevertheless, we point out that we linearly interpolate between values obtained by averaging over a sector. This is already and intrinsically more accurate than a linear interpolation performed between single pixels.

We recall that the method of background subtraction of RC06 assumes that the loop disappears at the end of the image sequence. The last image (around 10 UT) is then subtracted pixel-by-pixel from all other images, where the structures surrounding and crossing the loop of interest along the line of sight do not change much during the observation sequence. To estimate the background fluctuations during the observation, RC06 measured an average pixel-by-pixel standard deviation of 13% in both the 171 Å and the 195 Å filter band.

A more accurate subtraction would be achieved if the subtracted image were produced by interpolating between an image before the loop switches on and one after the loop switches off. Unfortunately, this loop has a very long lifetime and to find images acquired before the loop ignition we search more than 25 ks earlier than the start time of our analysis. In our opinion, this time is too long for us to assume that the environment did not change and to measure a reliable background, and we prefer to keep the final image as the only image for subtraction.

We also point out that the image to subtract was taken at 10:00 UT, significantly apart in time from the analyzed images taken between 06:30 and 08:30 UT. The perspective (i.e., viewing angle) of the observed loop varied during that interval possibly impacting the RC06 scheme, which assumes that each line of sight intersects

the same column of plasma throughout the entire sequence. However, we do not expect a significant effect since we estimate a change in the viewing angle of the order of $1-2^{\circ}$ or less, as confirmed by a visual inspection of the images after subtraction.

These are not the only two methods of background subtraction. Schmelz et al. (2007) and Schmelz et al. (2003) used two more approximate methods of background subtraction: (1) constant background subtraction, and (2) pixel pair background subtraction. In the former method, they subtract a constant value extracted from a single background pixel chosen above the loop apex; in the latter, they selected a background pixel for each loop pixel.

## A.4 Results

### A.4.1 Loop emission

Figures A.6 and A.7 show examples of applying our interpolation method of background subtraction. The lines join the data points, which are the mean values of the pixel emission in a sector. The error in each mean value is the standard deviation of the mean in that sector. The error was conservatively rounded to 0.05. The lower panels of Figs. A.6 and A.7 show the results subtracting values obtained by interpolating between the dotted and the dashed curves, from the solid curve.

The loop emission is diminished significantly by the background subtraction, at some points even completely cancelled, because of the overlap with other bright structures close to but independent of our loop. To directly comparison the interpolation and the RC06 background subtraction methods, we plot the emission along the loop obtained with the two methods in the same figure. Figure A.8 shows the results for both the 171 Å filter and the 195 Å filter. We can see that the emission significantly differs between the two methods: the profiles mostly differ in the central part, which is predicted to be very faint at any time after background subtraction

using the interpolation method. In contrast, with the latter method the footpoints are found to be mostly brighter than with the pixel-to-pixel subtraction, although we observe agreement at times (e.g., at the right extreme at 06:36 UT and 07:00 UT in both filters). The footpoint result is debatable, since the footpoint regions cannot be clearly resolved in the original data (Fig. A.3). There is no doubt, however, that the bulk of the loop is clearly visible at many times (Figs. A.3 and A.4), and therefore, the emission cannot be so low, in contrast to the interpolation method and in agreement with pixel-to-pixel method. Therefore, when the two methods differ the most, RC06's pixel-to-pixel method surely provides a more reliable result. There is some agreement between the profiles at the latest reported time.

We note in Fig. A.8 that, since the emission remaining after subtraction by the interpolation method is faint except close to the loop footpoints, it does not clearly evolve with time. RC06 found that the background-subtracted central section of the loop evolves in agreement with the evolution observed in the images (Figs. A.3 and A.4). Therefore, the results obtained with the RC06 method appear more reliable than those obtained with the interpolation method.

### A.4.2 Temperature diagnostics

To establish the differences between the background subtraction methods, we analyzed the temperature diagnostics obtained from the filter ratio. It is well-known that for an optically thin plasma, which is isothermal along the line of sight, the ratio of the emission detected in two different filters is a function of the temperature only (e.g., Rosner et al., 1978b). From the ratio value measured in an image pixel we can then derive a temperature value in that pixel and compile a proper thermal map. For the narrow-band 171 Å and 195 Å filters of TRACE, the relationship between temperature and filter ratio 195/171 is monotonic only across a certain temperature range, i.e., $0.7 < T < 1.8$ MK (e.g., Aschwanden et al., 2000), the

range for which the filter responses are the highest. It is reasonable to assume that the detected plasma is all in that temperature range and this allows us to measure the temperature along the loop, after background subtraction. As an example, Fig. A.9 shows the filter ratio 195/171 and the corresponding temperature along the loop at 07:40 UT computed after the background subtraction using the pixel-to-pixel method (also shown in RC06) and the interpolation method. The ratio profile obtained with the latter method appears to be far more irregular, so we are unable to define an overall trend. In contrast, the other method produces a more regular profile, which is coherent with the clear visibility of the loop in the filter ratio map (RC06), despite the dip at the left leg caused by another crossing bright structure. We find similar trends in the corresponding temperature profiles along the loop.

We emphasize that, although both profiles indicate overall a small temperature variation along the loop, the quality of the pixel-to-pixel background determines whether a trend can be identified or not. The globally flat temperature profile is typical of TRACE data (e.g., Lenz et al., 1999) and was attributed in part to an instrumental bias (Weber et al., 2005). However, RC06 showed that the filter ratio diagnostics are anyhow meaningful and sensitive enough to detect the loop progressive cooling. Figure A.10 shows the loop average filter ratio obtained after the two different background-subtraction methods at four different times. From the evolution obtained with the interpolation method, it is far less clear that the loop is cooling, confirming that the sensitivity of the temperature diagnostics is higher with the pixel-to-pixel background subtraction.

## A.5 Discussion

We have demonstrated that the accuracy of the background subtraction can significantly affect the quality of the analysis of TRACE coronal loops because the

background signal is very high and influenced by many bright structures near and perhaps entangled with the analyzed loop, along the line of sight. We have taken advantage of a unique opportunity to compare two different and independent methods of background subtraction: one that subtracts the interpolated emission of two off-loop strips; and the other that subtracts pixel-by-pixel the complete image after the disappearance of the loop (RC06). Extracting the background emission with two strips as close as possible to the loop of interest, we have been able to remove emission from structures that can transversally intersect the loop. This is true as long as the "contaminating" loops run across the target loop, while it is not true when this occurs at an oblique angle.

We have shown that not only do different methods produce different emission profiles, but that the subsequent diagnostics are affected. With the pixel-by-pixel subtraction, we are able to derive coherent filters ratio profiles along the loop and measure a coherent temperature evolution where the loop globally cools as expected from the sequence of appearance/disappearance in the different TRACE filters. These results are far less clear after using the other method of background subtraction.

The RC06 background subtraction therefore looks to be a more reliable method. In principle, it is accurate, if the loop of interest is the most variable structure in the field of observation; it is direct, in contrast to the interpolation method; it is applied pixel-by-pixel, allowing us to derive "background-subtracted images" and therefore to achieve a visual feedback by analyzing all loop pixels, instead of sampling them at selected positions. On the other hand, this method works well as long as the structures surrounding and crossing the loop of interest along the line of sight do not change much during the observation. In other words, the RC06 method cannot take time variations in the background emission into account and we cannot exclude that crossing structures vary during the observation. We also remark that

the pixel-by-pixel subtraction could be applied only because the loop disappears at the end of the image sequence. This condition can be matched only by evolving loops. For loops that remain steady during the entire observation, other methods must be used. The interpolation of out-loop emission has often been used (Testa et al., 2002; Aschwanden & Nightingale, 2005; Schmelz et al., 2003, and Aschwanden et al., 2008), but according to our analysis, it may lead to severe systematic errors when affected by other structures close to but distinct from the loop under analysis.

Figure A.5 illustrates the difficulties encountered by the interpolation method by showing that close to the target loop there is another structure of similar intensity. Although the interpolation method should reliably estimate the background around the two loops, it is unable to take the overlap of the two loops properly into account. A scheme that fits separately the two loops and their respective backgrounds estimated as above may provide a more accurate solution.

Other methods of background subtraction are instead too "operator-sensitive", because they are based on the meticulous selection of single background pixels, intentionally avoiding in this way structures that can cross the loop of interest and significantly alter the loop emission.

In conclusion, this work confirms and qualifies how a reliable background subtraction is a delicate and difficult task when analyzing coronal loops observed with TRACE. The problem can of course be greatly reduced by performing observations with instruments that have far lower instrumental background emission and hence lower systematic errors.

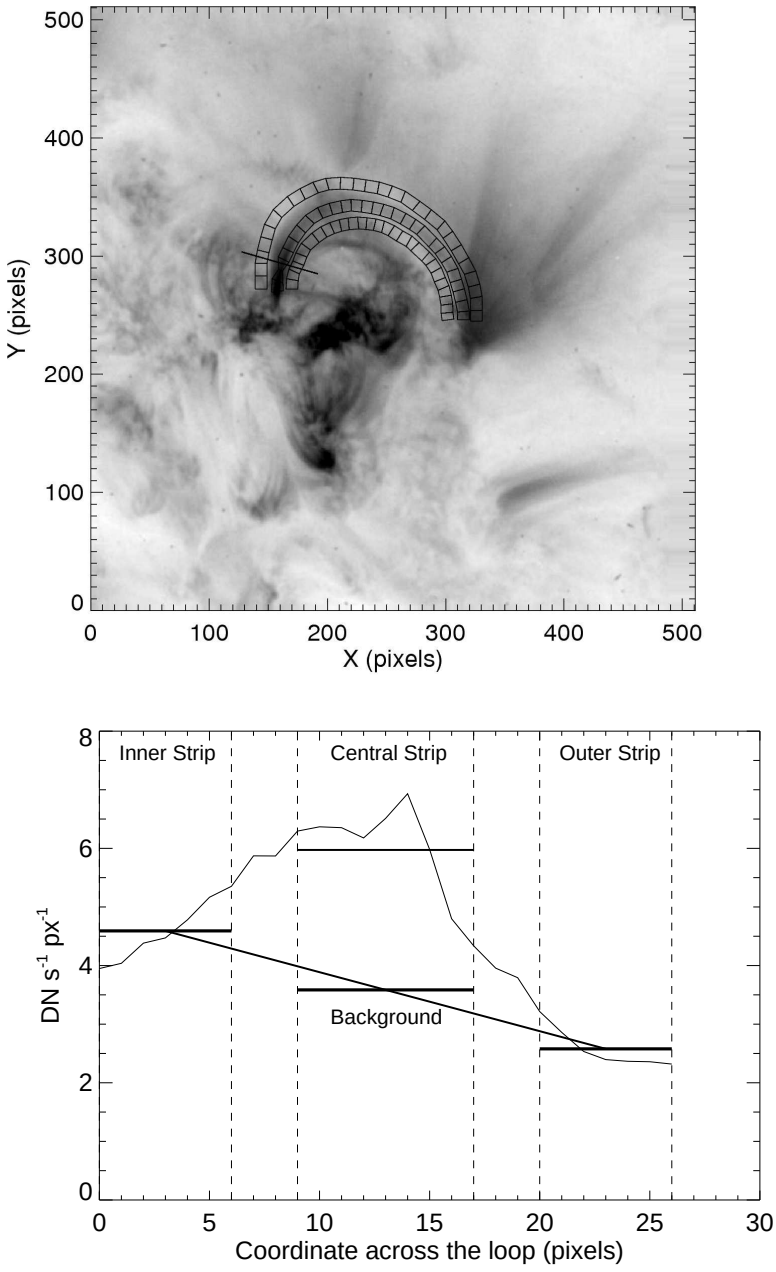


Figure A.5 Background subtraction with interpolation method. *Upper panel:* the strips for the loop analysis (central) and for the background subtraction (outer and inner) are marked in the loop region (07:39:26.000 UT, 171 Å filter). *Lower panel:* Emission profile (*thin solid line*) measured for a cut across the loop (marked in the upper panel). We compute the average emission (thick horizontal lines) in the corresponding sectors intersected by the outer and inner strips (bounded by vertical dashed lines). The background value (central horizontal line) is computed by linear interpolation of the average emission values of the outer strips. This is then subtracted from the total emission measured in the central strip (upper solid line).

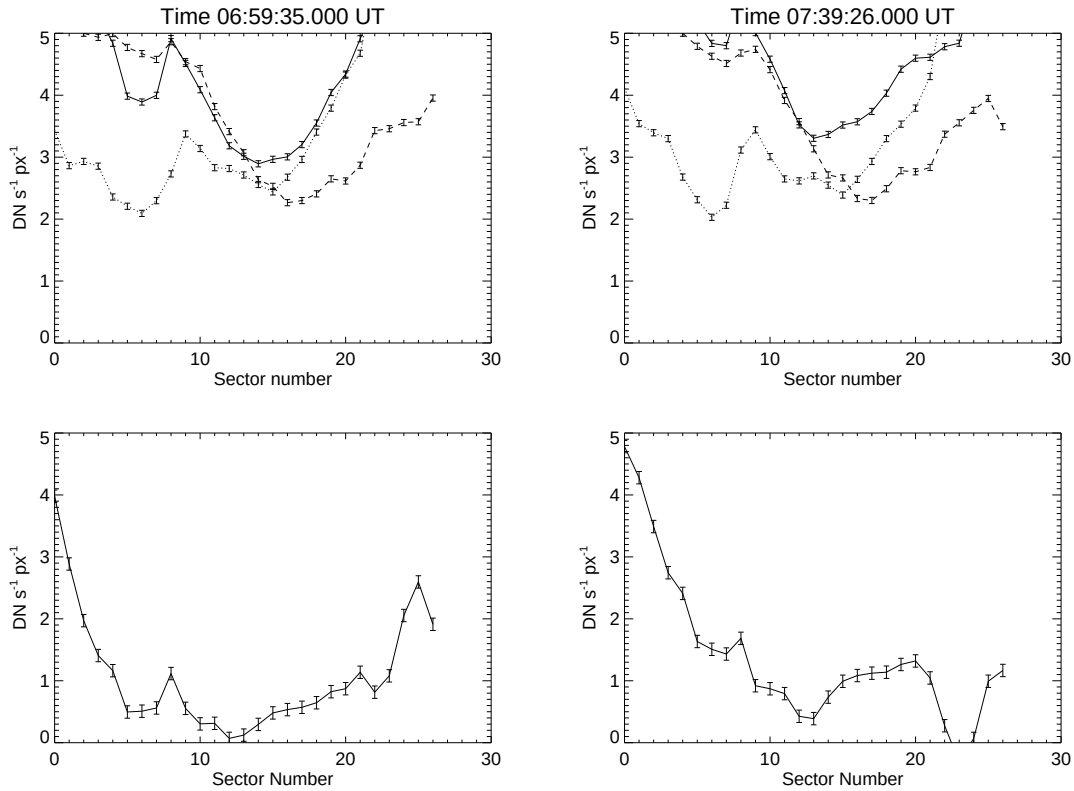


Figure A.6 Emission along the loop in the 171 Å filter, at 06:59:35.000 UT (left column), and 07:39:26.000 UT (right column). Upper panels: emission along the loop strip (solid line), outer strip (dotted line), and inner strip (dashed line). Lower panels: emission after background subtraction with the interpolation method.

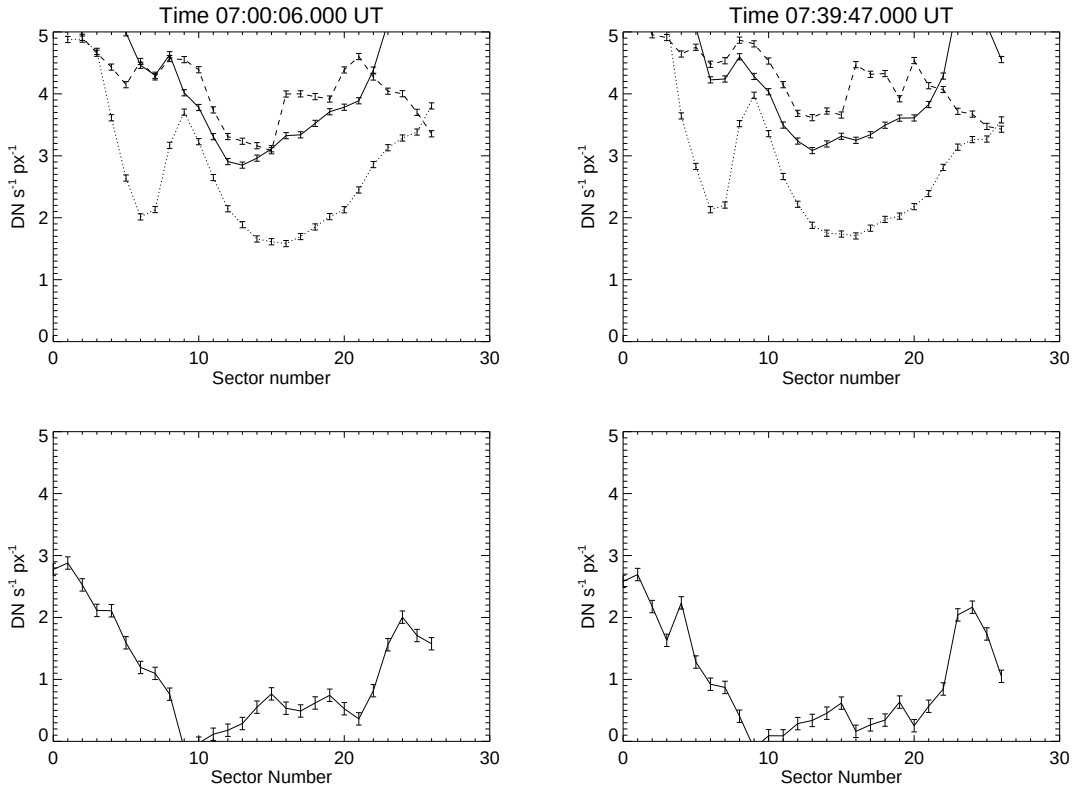


Figure A.7 As Fig. A.6 for the 195 Å filter, at 07:00:06.000 UT (left column), and 07:39:47.000 UT (right column).

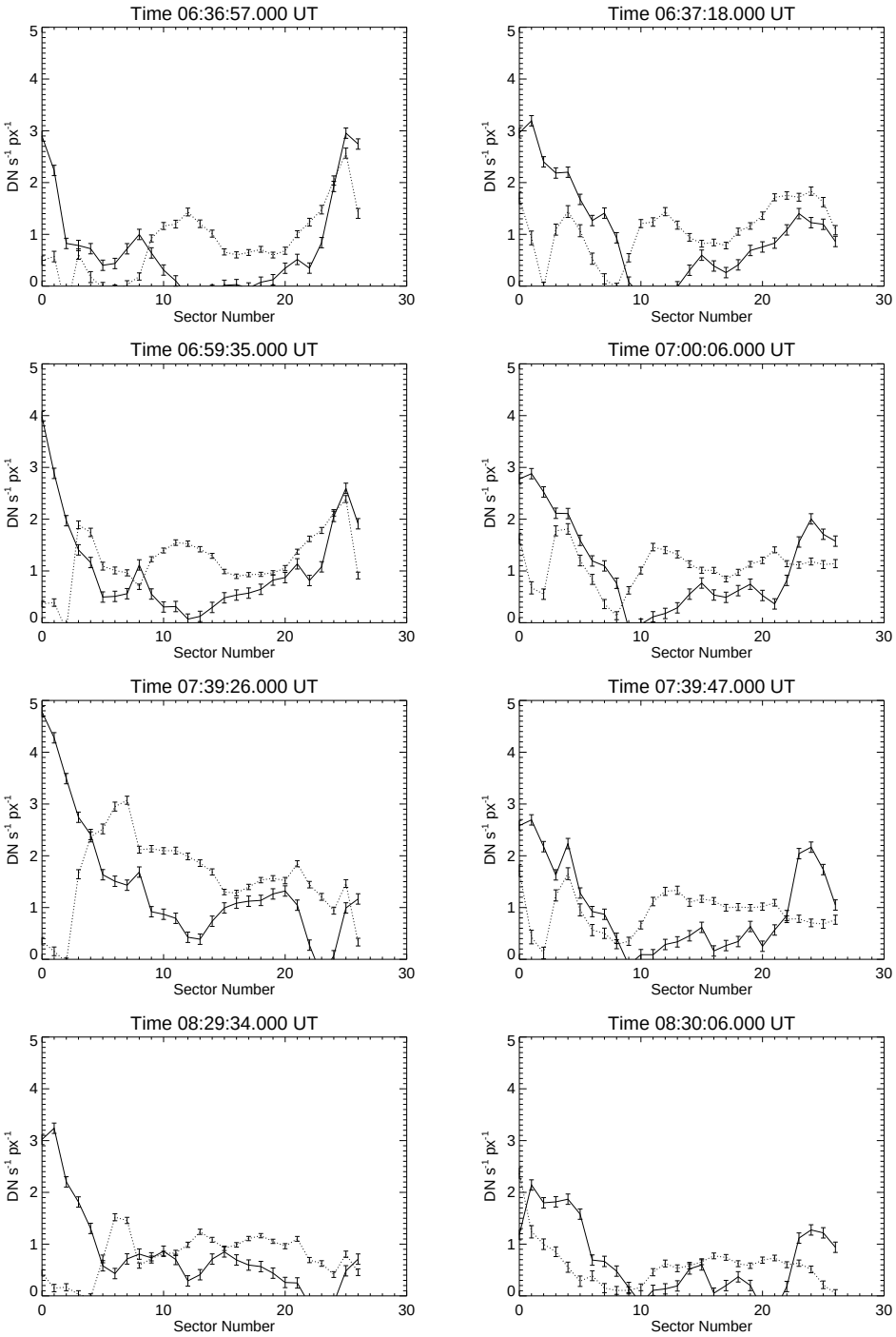


Figure A.8 Emission along the loop at the labelled times in the 171 Å filter (left column) and the 195 Å filter (right column). All panels show the emission along the loop, after background subtraction with two different methods: pixel-by-pixel method (RC06, dashed line), and interpolation method (solid line).

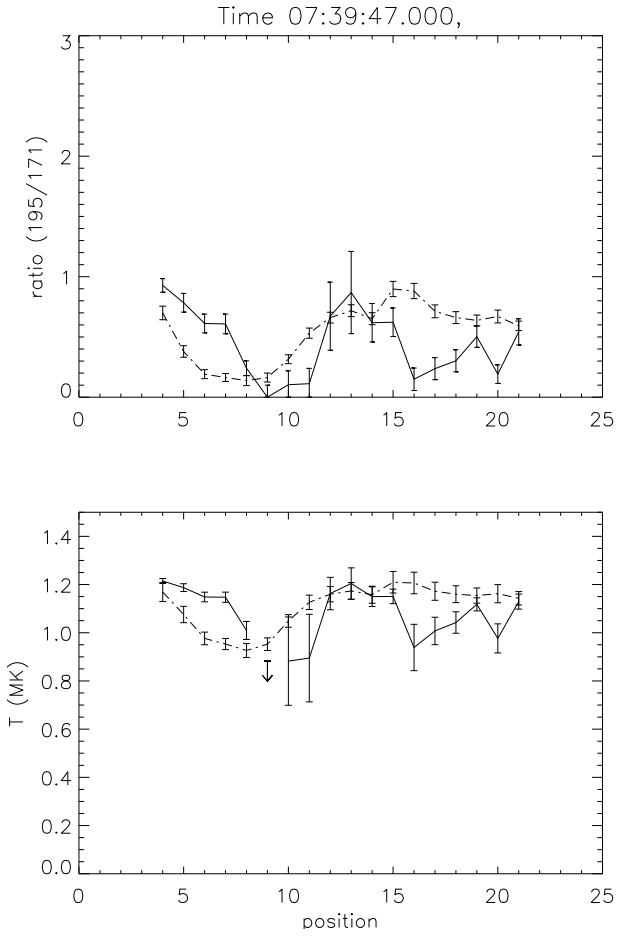


Figure A.9 Filter ratio 195/171 (*top*) and corresponding temperature (*bottom*) along the loop at 07:40 UT computed after background subtractions with either the pixel-to-pixel (*dashed*) or interpolation (*solid*) methods. The arrow is an upper limit to the interpolation data.

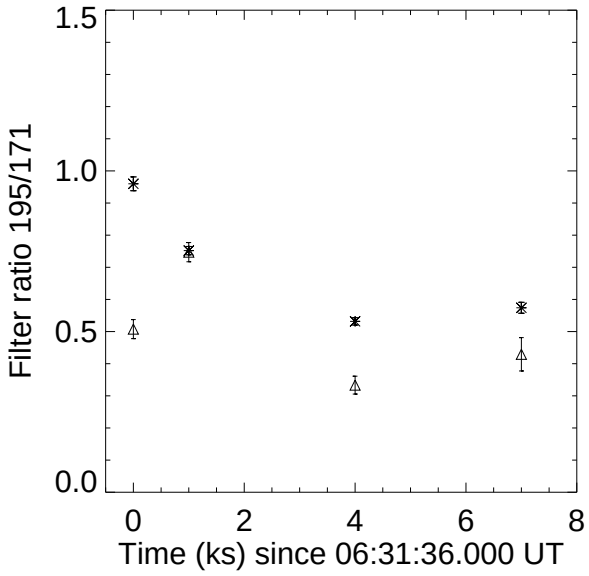


Figure A.10 Evolution of the loop average 195/171 filter ratio, sampled at the four times analyzed in this work and obtained by applying background subtractions, with either the pixel-to-pixel (*stars*) or interpolation (*triangles*) methods.

# Bibliography

Aschwanden, M. J., & Nightingale, R. W. 2005, ApJ, 633, 499

Aschwanden, M. J., Nitta, N. V., Wuelser, J.-P., & Lemen, J. R. 2008, ApJ, 680, 1477

Aschwanden, M. J., Tarbell, T. D., Nightingale, R. W., Schrijver, C. J., Title, A., Kankelborg, C. C., Martens, P., & Warren, H. P. 2000, ApJ, 535, 1047

Betta, R., Peres, G., Reale, F., & Serio, S. 1997, A&A, 122, 585

Brooks, D. H., Ugarte-Urra, I., & Warren, H. P. 2008, ApJ, 689, L77

Brooks, D. H., & Warren, H. P. 2009, ApJ, 703, L10

Cargill, P. J. 1994a, ApJ, 422, 381

—. 1994b, ApJ, 422, 381

Cargill, P. J., & Klimchuk, J. A. 2004, ApJ, 605, 911

Collura, A., Barbera, M., Inzerillo, G., Mirabello, F., Sciortino, S., & Serio, S. 1994, in Society of Photo-Optical Instrumentation Engineers (SPIE) Conference Series, Vol. 2280, Society of Photo-Optical Instrumentation Engineers (SPIE) Conference Series, ed. O. H. Siegmund & J. V. Vallerga, 206–213

Cosmo, M. L. et al. 2005, in Society of Photo-Optical Instrumentation Engineers (SPIE) Conference Series, Vol. 5900, Society of Photo-Optical Instrumentation Engineers (SPIE) Conference Series, ed. O. Citterio & S. L. O'Dell, 99–105

De Pontieu, B. et al. 2011, Science, 331, 55

DeForest, C. E., Martens, P. C. H., & Wills-Davey, M. J. 2009, ApJ, 690, 1264

Del Zanna, G., & Mason, H. E. 2003, A&A, 406, 1089

Drake, J. F. 1971, Sol. Phys., 16, 152

Golub, L. et al. 2007, Sol. Phys., 243, 63

Gomez, D. O., Martens, P. C. H., & Golub, L. 1993, ApJ, 405, 767

Guarrasi, M., Reale, F., & Peres, G. 2010, ApJ, 719, 576

Handy, B. N. et al. 1999, Sol. Phys., 187, 229

Hong, J., Schlegel, E. M., & Grindlay, J. E. 2004, ApJ, 614, 508

Hudson, H. S. 1991, Sol. Phys., 133, 357

Kahler, S. 1976, Sol. Phys., 48, 255

Kano, R. et al. 2004, in Astronomical Society of the Pacific Conference Series, Vol. 325, The Solar-B Mission and the Forefront of Solar Physics, ed. T. Sakurai & T. Sekii, 15–+

Kano, R. et al. 2008, Sol. Phys., 249, 263

Kano, R., Shimizu, T., & Tarbell, T. D. 2010, ApJ, 720, 1136

Kano, R., & Tsuneta, S. 1995, ApJ, 454, 934

Katsukawa, Y. 2003, PASJ, 55, 1025

Katsukawa, Y., & Tsuneta, S. 2001, ApJ, 557, 343

Klimchuk, J. A. 2006a, Sol. Phys., 234, 41

—. 2006b, Sol. Phys., 234, 41

Kosugi, T. et al. 2007, Sol. Phys., 243, 3

Labonte, B. J., & Reardon, K. P. 2007, Sol. Phys., 240, 387

Lemen, J. R., Title, A. M., J., A. D., & Boerner, P. F. 2011, Sol. Phys.

Lenz, D. D., Deluca, E. E., Golub, L., Rosner, R., Bookbinder, J. A., Litwin, C., Reale, F., & Peres, G. 1999, Sol. Phys., 190, 131

Lin, R. P., Schwartz, R. A., Kane, S. R., Pelling, R. M., & Hurley, K. C. 1984, ApJ, 283, 421

Liu, S.-Y. 1974, ApJ, 189, 359

López Fuentes, M. C., Klimchuk, J. A., & Mandrini, C. H. 2007, ApJ, 657, 1127

Maritz, J., & Jarrett, R. 1978, Jounal of the American Statistical Association, 73

Moretti, P. F., Cacciani, A., Hanslmeier, A., Messerotti, M., Oliviero, M., Otruba, W., Severino, G., & Warmuth, A. 2001, A&A, 372, 1038

Narukage, N. et al. 2011, Sol. Phys., 269, 169

Parenti, S., Reale, F., & Reeves, K. K. 2010, A&A, 517, A41+

Parker, E. N. 1983, ApJ, 264, 635

—. 1988, ApJ, 330, 474

—. 1991, ApJ, 372, 719

Patsourakos, S., & Klimchuk, J. A. 2005, ApJ, 628, 1023

—. 2007, ApJ, 667, 591

—. 2008, ArXiv e-prints, 808

Peres, G., Orlando, S., Reale, F., Rosner, R., & Hudson, H. 2000, ApJ, 528, 537

Peres, G., Serio, S., Vaiana, G. S., & Rosner, R. 1982, ApJ, 252, 791

Priest, E. R. 1982, Solar magneto-hydrodynamics (Dordrecht, Holland ; Boston : D. Reidel Pub. Co. ; Hingham,), 74P–+

Raymond, J. C., & Smith, B. W. 1977, ApJS, 35, 419

Reale. 2007, A&A, 471, 271

Reale, F. 2002a, ApJ, 580, 566

Reale, F. 2002b, in Astronomical Society of the Pacific Conference Series, Vol. 277, Stellar Coronae in the Chandra and XMM-NEWTON Era, ed. F. Favata & J. J. Drake, 103

Reale, F. 2005, in ESA Special Publication, Vol. 600, The Dynamic Sun: Challenges for Theory and Observations

—. 2010, Living Reviews in Solar Physics, 7, 5

Reale, F., & Ciaravella, A. 2006, A&A, 449, 1177

Reale, F., Nigro, G., Malara, F., Peres, G., & Veltri, P. 2005, ApJ, 633, 489

Reale, F., & Orlando, S. 2008, ApJ, 684, 715

Reale, F. et al. 2007, Science, 318, 1582

Reale, F., Testa, P., Klimchuk, J. A., & Parenti, S. 2009, ApJ, 698, 756

Rosner, R., Golub, L., Coppi, B., & Vaiana, G. S. 1978a, ApJ, 222, 317

Rosner, R., Tucker, W. H., & Vaiana, G. S. 1978b, ApJ, 220, 643

Sakamoto, Y., Tsuneta, S., & Vekstein, G. 2008, ApJ, 689, 1421

—. 2009, ApJ, 703, 2118

Schmelz, J. T., Beene, J. E., Nasraoui, K., Blevins, H. T., Martens, P. C. H., & Cirtain, J. W. 2003, ApJ, 599, 604

Schmelz, J. T., Roames, J. K., & Nasraoui, K. 2007, Advances in Space Research, 39, 1497

Seaton, D. B., Winebarger, A. R., DeLuca, E. E., Golub, L., Reeves, K. K., & Gallagher, P. T. 2001, ApJ, 563, L173

Serio, S., Peres, G., Vaiana, G. S., Golub, L., & Rosner, R. 1981, ApJ, 243, 288

Serio, S., Reale, F., Jakimiec, J., Sylwester, B., & Sylwester, J. 1991, A&A, 241, 197

Shimizu, T. 1995, PASJ, 47, 251

—. 2002, Advances in Space Research, 29, 2009

Shimizu, T., & Tsuneta, S. 1997, ApJ, 486, 1045

Strong, K. T., Harvey, K., Hirayama, T., Nitta, N., Shimizu, T., & Tsuneta, S. 1992, PASJ, 44, L161

Terzo, S., & Reale, F. 2010, A&A, 515, A7

Terzo, S., Reale, F., Miceli, M., Klimchuk, J. A., Kano, R., & Tsuneta, S. 2011, ApJ, 736, 111

Testa, P., Landi, E., & Drake, J. 2010, in Bulletin of the American Astronomical Society, Vol. 41, American Astronomical Society Meeting Abstracts 216, 402.03

Testa, P., Peres, G., & Reale, F. 2005, ApJ, 622, 695

Testa, P., Peres, G., Reale, F., & Orlando, S. 2002, ApJ, 580, 1159

Tucker, W. H. 1973, ApJ, 186, 285

Vaiana, G. S., Krieger, A. S., & Timothy, A. F. 1973, Sol. Phys., 32, 81

Vekstein, G. 2009, A&A, 499, L5

Vekstein, G., & Katsukawa, Y. 2000, ApJ, 541, 1096

Warren, H. P., Winebarger, A. R., & Hamilton, P. S. 2002, ApJ, 579, L41

Warren, H. P., Winebarger, A. R., & Mariska, J. T. 2003, ApJ, 593, 1174

Weber, M. A., Schmelz, J. T., DeLuca, E. E., & Roames, J. K. 2005, ApJ, 635, L101